2008

NUMERICAL MIXING PLANE STUDIES WITH VALIDATION FOR AERO-ENGINE CENTRIFUGAL COMPRESSOR DESIGN

Jason A. Bourgeois
Western University

Recommended Citation

Bourgeois, Jason A., "NUMERICAL MIXING PLANE STUDIES WITH VALIDATION FOR AERO-ENGINE CENTRIFUGAL COMPRESSOR DESIGN" (2008). *Digitized Theses*. 4857.
https://ir.lib.uwo.ca/digitizedtheses/4857

NUMERICAL MIXING PLANE STUDIES WITH VALIDATION FOR AERO-ENGINE CENTRIFUGAL COMPRESSOR DESIGN

(Spine title: Numerical Mixing Plane Studies for Centr. Compressor Design)
(Thesis format: Monograph)

by

Jason A. Bourgeois

Graduate Program in Engineering Science
Department of Mechanical and Materials Engineering

A thesis submitted in partial fulfillment
of the requirements for the degree of
Master of Engineering Science

Faculty of Graduate Studies
The University of Western Ontario
London, Ontario, Canada

ABSTRACT

The unsteady high-speed flow in centrifugal compressor stages tests current limitations of modeling techniques due to high degrees of curvature, adverse pressure gradients, and three-dimensional turbulent boundary layers. The current study presents experimental and numerical validation studies of predictions for a centrifugal compressor stage with a tandem impeller and fish-tail discrete passage diffuser using the mixing plane approach presently used for the design of these stages. Assessments are made of predictions with a more accurate geometry representation than has been modeled previously and with a number of turbulence closure models including the $k-\epsilon$, SST, SST-RM, and RSM-SSG models. Comparison with measured performance parameters seems to indicate better predictions by the RSM-SSG and SST models. For further validation of the numerical modeling, the latest results of a laser Doppler velocimetry study are presented and compared to numerical predictions, yielding good agreement at stage inlet and exit.

KEYWORDS: Turbomachinery, computational fluid dynamics, mixing plane, centrifugal compressor, gas turbine, impeller, tandem impeller, diffuser, fish-tail diffuser, fluid machinery, laser Doppler velocimetry

ACKNOWLEDGMENTS

I would like to thank Pratt & Whitney Canada for their financial support for this project and the great opportunities offered through their collaboration with the University of Western Ontario and the University of Calgary. This project would not have been possible without the time, effort, and guidance given by their senior compressor aerodynamics engineers Douglas Roberts, Feng Shi, and Peter Townsend. I would also like to thank the P&WC test group, headed by Elizabeth Gioia, for their wonderful help and support during the LDV test campaign. Many thanks are extended to the project supervisors, Dr. Eric Savory, Dr. Robert Martinuzzi, and Dr. Chao Zhang for their support, contributions, and many discussions over the course of the project. As well, I must thank my colleagues Rita Patel at the University of Western Ontario and Dr. Rofiqul Islam at the University of Calgary for their help over the course of this project and for their contributions. Finally, thanks are also extended to the Natural Sciences and Engineering Research Council of Canada for their additional financial support through the Canada Graduate Scholarship program.

Contents

List of Tables

List of Figures

LIST OF ABBREVIATIONS, SYMBOLS, AND NOMENCLATURE

Latin Symbols

a	speed of sound
a_{ij}	anisotropy tensor
A	area
A_{eff}	effective flow area
A_{geom}	geometric area
B	blockage factor
$\vec{C}$	stationary frame of reference fluid velocity
C_{ijk}	third-order diffusion correlation
$\overline{d_p}$	area averaged deviation from the mean pressure
e	internal energy
E	total energy
F_1	first blending function from the SST model
F_2	second blending function from the SST model
h	static enthalpy
k	turbulent kinetic energy
$\dot{m}$	mass flow rate

$\dot{m}_c$	corrected mass flow rate
$\dot{m}_{c,net}$	net corrected mass flow rate
M	Mach number
n_i	component of the surface normal vector in the direction of the i-th base vector
N	total number of samples
p	pressure
P_k	production of turbulent kinetic energy
$P_{reattach}$	additional production of turbulent kinetic energy in SST-RM model
Pr_T	turbulent Prandtl number
q_i	component of the heat flux vector in the direction of the i-th base vector
r	radius
R	gas constant
Re	Reynolds number
s	denotation of an arbitrary variable
s_{ij}	instantaneous strain rate tensor
S_{ij}	mean strain rate tensor

S	material surface
SD	sample standard deviation
S_i^m	source of momentum in the direction of the i-th base vector
$S_i^{m,Rot}$	rotational reference frame source of momentum in the direction of the i-th base vector
$S_i^{m,Cor}$	Coriolis source of momentum in the direction of the i-th base vector
$S_i^{m,Cfg}$	centrifugal source of momentum in the direction of the i-th base vector
t	time
t_{ij}	viscous stress tensor
T	temperature
TR	temperature ratio
u_i	Cartesian component of velocity in the direction of the i-th base vector
u	Cartesian x-wise component of velocity
$\vec{U}$	local blade velocity
v	Cartesian y-wise component of velocity

V	material volume; velocity magnitude
w	Cartesian z-wise component of velocity
$\vec{W}$	relative frame of reference fluid velocity
x_i	Cartesian coordinate component along the i-th base vector

Greek Symbols

α	flow angle between the meridional direction and the absolute velocity vector
β	flow angle between the meridional direction and the relative velocity vector
γ	ratio of specific heats
δ_{ij}	Kronecker delta (equals 1 when $i = j$ and 0 otherwise)
ϵ	rate of dissipation of turbulent kinetic energy
ϵ_{ij}	dissipation rate correlation
ϵ_P	precision uncertainty due to random fluctuations about the mean
ζ	spanwise coordinate
η	efficiency

κ	thermal conductivity; bulk viscosity
ξ	streamwise coordinate
λ	second viscosity coefficient
λ_p	impeller passage pitch fraction
μ	molecular viscosity coefficient
μ_T	eddy viscosity (or turbulent viscosity) from the Boussinesq approximation
ν	molecular kinematic viscosity
ν_T	kinematic eddy viscosity
Π	pressure ratio
Π_{ij}	pressure-strain correlation
θ	circumferential coordinate
ρ	density
σ	slip factor
σ_{ij}	total stress tensor
σ_k	closure coefficient from the $k-\epsilon$ model
σ_p	root mean square deviation from the mean pressure
σ_ϵ	closure coefficient from the $k-\epsilon$ model
τ_{ij}	Reynolds stress tensor

ϕ	denotation of an arbitrary scalar field variable; meridional flow direction
ψ	denotation of an arbitrary scalar field variable
ω	rate of rotation of the impeller; turbulence frequency
Ω	mean vorticity magnitude
Ω_{ij}	mean vorticity tensor

Accents, subscripts, and superscripts

(given in terms of arbitrary variable ϕ)

$\bar{\phi}$	time average according to the Reynolds decomposition
ϕ'	fluctuation of ϕ about the Reynolds average
$\tilde{\phi}$	mass-weighted time average according to the Favre decomposition
ϕ''	fluctuation of ϕ about the Favre average
ϕ_0	total (stagnation) quantity of ϕ
ϕ_1	ϕ at impeller inlet
ϕ_2	ϕ at impeller exit (trailing edge)
ϕ_{2Shr}	ϕ at the impeller trailing edge on the shroud surface
ϕ_3	ϕ at diffuser throat

ϕ_4	ϕ at diffuser exit
ϕ_x	axial component of a vector quantity, ϕ
ϕ_r	radial component of a vector quantity, ϕ
ϕ_{rel}	quantity, ϕ, in the relative frame of reference
ϕ_{ref}	reference value of quantity ϕ
ϕ_θ	circumferential component of a vector quantity, ϕ
ϕ_m	meridional component of a vector quantity, ϕ
ϕ_{Coarse}	quantity, ϕ, for the coarse grid
ϕ_{Med}	quantity, ϕ, for the medium (standard) grid
ϕ_{Fine}	quantity, ϕ, for the fine grid
ϕ_f	quantity, ϕ, for a grid with the approximated fillet geometry
ϕ_{nf}	quantity, ϕ, for a grid with no approximated fillet geometry (upper blade surface extrapolated to hub surface)
ϕ^*	quantity, ϕ, at the aerodynamic throat when choking occurs

Abbreviations

CFD	Computational Fluid Dynamics

DNS	Direct Numerical Simulation
L2F	Laser-2-Focus Velocimetry
LES	Large Eddy Simulation
LDV	Laser Doppler Velocimetry
LE	Leading Edge
P&WC	Pratt & Whitney Canada
PIV	Particle Image Velocimetry
RANS	Reynolds Averaged Navier Stokes
RSM-SSG	Speziale, Sarkar, and Gatski Reynolds Stress Model
SST	Menter's Shear Stress Transport turbulence model
SST-RM	Menter's Shear Stress Transport with Reattachment Modification
TE	Trailing Edge

Chapter 1

Introduction

Larger gas turbine engines for use on aircraft implement several compressor stages, all of which are typically of the axial stage type where the hub and shroud walls constrain the flow to move along the machine axis. Smaller aero-engines, however, may employ a centrifugal compressor stage at the rear of the compressor. It is this type of stage that is studied herein. Depending on the flow rate needed for a specific application, the highest efficiency achievable depends on the style of the turbomachine. For higher flow rates, the advantage lies with in axial compressors, while for lower flow rates, the advantage shifts to centrifugal compressors (Dixon, 2005). The specific work input to the fluid for a given size of component can be much higher with the centrifugal compressor since it takes advantage of centrifugal effects. A centrifugal compressor stage consists of a rotating impeller and a stationary diffuser which follow one after the other along the gas path. Unlike axial compressor stages, the gas path in a centrifugal compressor is turned from axial at the inlet of the impeller to radial at the exit of the impeller. A centrifugal stage of this type would be located downstream of a number of axial stages and just upstream of the combustion chamber.

Until recently, industrial design of these compressor stages has generally utilized computational fluid dynamics (CFD) techniques where the two main components of the compressor stage are considered in isolation (Roberts and Steed, 2004; Roberts and Kacker, 2002). First the rotor is simulated in the rotational frame of reference assuming a constant static pressure at the exit of the computational domain. Diffuser simulations would not include the vaneless space region where the exit flow from the impeller enters the diffuser. Simulations of fish-tail pipe diffusers, instead, would start further downstream at the diffuser throat with a power-law boundary layer profile applied as an inlet boundary condition. The interaction effects that occur between the components are thereby ignored. It was only once a design was complete and the parts were manufactured and tested experimentally that the true coupled flow field was found. In a number of cases, the interaction effects that occur when coupling the impeller and diffuser would negatively affect the performance of the diffuser and one or both of the components would therefore need to be redesigned to improve the stage performance. However, the flow coupling between the newly designed components would still be unknown until they are again manufactured and tested.

Within the last few years, mixing plane techniques have become part of the state of the art design process for centrifugal stages. Mixing plane techniques yield steady state solutions to the governing equations in turbomachinery computations where the mixing process at the interface between a rotating impeller and stationary diffuser is modeled while retaining certain important coupled aspects of the pressure and velocity flow fields of the two components necessary for more accurate performance calculations than were possible using the previous isolated analysis methodology.

The general CFD methodology that is fundamentally the same in either of these design processes has been developed to numerically solve the set of governing equations of fluid flow, the Navier Stokes equations, through or around any given geometry. These numerical methods have been developed because the solution of the Navier Stokes equations analytically has only been possible for a handful of simple flows. As any numerical simulation is limited by the computing power available at any given time, the techniques have evolved alongside the development of computing technology since the 1960's as the simulations usually require a large amount of computing power. CFD, if properly validated, can reduce the design costs by minimizing the experimental testing needed. The unsteady high-speed flow in centrifugal compressors is quite complex in terms of the fluid dynamics involved, and the physical processes are not fully understood, especially in terms of rotor-stator interaction. CFD model developments that allow steady state solutions in coupled rotating and stationary components require studies that combine both experimental and numerical CFD aspects for validation of the modeling before the limitations and strengths of the methodology can be assessed, including particularly an understanding of when the model is physically valid, and under what conditions it may become invalid.

The present work is part of a collaborative project that combines both numerical and experimental studies and has been undertaken by Pratt & Whitney Canada, the University of Western Ontario, and the University of Calgary with the general goal of understanding the flow physics of this particular style of centrifugal compressor stage, and to assess the capabilities and deficiencies of the pseudo-steady-state mixing plane analysis now used in centrifugal compressor design. The study presented herein looks at a centrifugal compressor stage with a tandem impeller and fish-tail pipe diffuser and focuses predominantly on the numerical investigations of previously unstudied aspects of the state of the art methodology while providing experimental velocity flow field data to supplement previously available performance data for validation.

In terms of the velocity flow field measurements undertaken, laser Doppler velocimetry (LDV) is employed to obtain point measurements of velocities in a compressor test rig fitted with the compressor stage studied. These investigations are still ongoing at the submission of this thesis. LDV measurements had also been taken in a stationary cascade rig in an earlier stage of the project. The stationary cascade rig was used as a preliminary study to allow familiarization with the difficult task of taking velocity flow field measurements in such a restricted and complex environment as in a centrifugal stage. The rig was designed to have a similar outlet flow velocity and direction as the rotating compressor stage does at its design condition and the investigations have been documented in Patel (2007). Measurements of the actual compressor stage flow are taken in the industrial testing centre operated by Pratt & Whitney Canada in Longueuil, Quebec. Data available for validation for the present work were flow field data at the inlet and outlet to the compressor stage as well as some of the first measurements in the vaneless space region downstream of the impeller trailing edge and upstream of the elliptical leading edges of the pipe diffuser. The non-intrusive LDV measurements supplement the pressure and temperature measurements available previously for performance calculations which, to date, are the only measurements available besides some limited pitot and cobra pressure probe traverses in these compressor stages.

1.1 Organization of the thesis

The mixing plane numerical methodology for simulating the full compressor stage is employed under various configuations of the stage geometry and the results are assessed against the experimental performance and flow field data gathered. Chapter 2 introduces the necessary description of a compressor stage, including terminology and specific details regarding the stage studied here. This is followed in Chapter 3 by a discussion of the general details of the governing equations to be solved for compressible turbulent flow computations and the modeling that is necessary to predict the mean flow field without resorting to very computationally intensive direct numerical simulation (DNS) or large eddy simulation (LES) which is impractical and sometimes infeasible for turbomachinery design. In Chapter 4 a description is given of the aspects of the computations that are specific to the compressor stage simulations. This includes a discussion of the solver, the mixing plane approach, the boundary conditions, the grid and the near-wall treatment employed. Chapter 5 then describes a grid independence study done for the compressor studied, and this is followed by Chapter 6 which is devoted to a discussion of the modeling of the geometry and turbulence quantitities that is taken as a baseline case against which subsequent modeling is compared. An assessment is then given in Chapter 7 of the effects of more accurate representation of the impeller fillets as well as the effect of the location of the outlet boundary condition. Following this there is a discussion in Chapter 8 of using different turbulence models. Finally the most current results available from LDV measurements in the compressor rig are presented in Chapter 9.

Chapter 2

Background

2.1 Description of geometry, conventions, and notation

Typical conventions used in terms of geometry and frames of reference will be presented here. There is a description both of conventional turbomachinery notation for the reader unfamiliar with this usage as well as certain conventions for notation that are particular to the compressor stage geometry studied.

A centrifugal compressor stage consists of two primary components: a rotating impeller and a stationary diffuser. The impeller increases the energy of the working fluid (air in an aero-engine) by drawing it in through the eye (the inlet) of the impeller from a predominantly axial direction, and whirling it outwards in the radial direction, increasing the momentum of the fluid (Dixon, 2005). The static pressure and the velocity of the fluid are increased by the impeller, and the kinetic energy is converted in the diffuser to pressure energy. The present work investigates the flow field within an aero gas-turbine centrifugal compressor stage. Numerical analyses have been carried out for a stage consisting of a tandem bladed impeller and a fish-tail pipe diffuser as shown in Fig. 2.1.

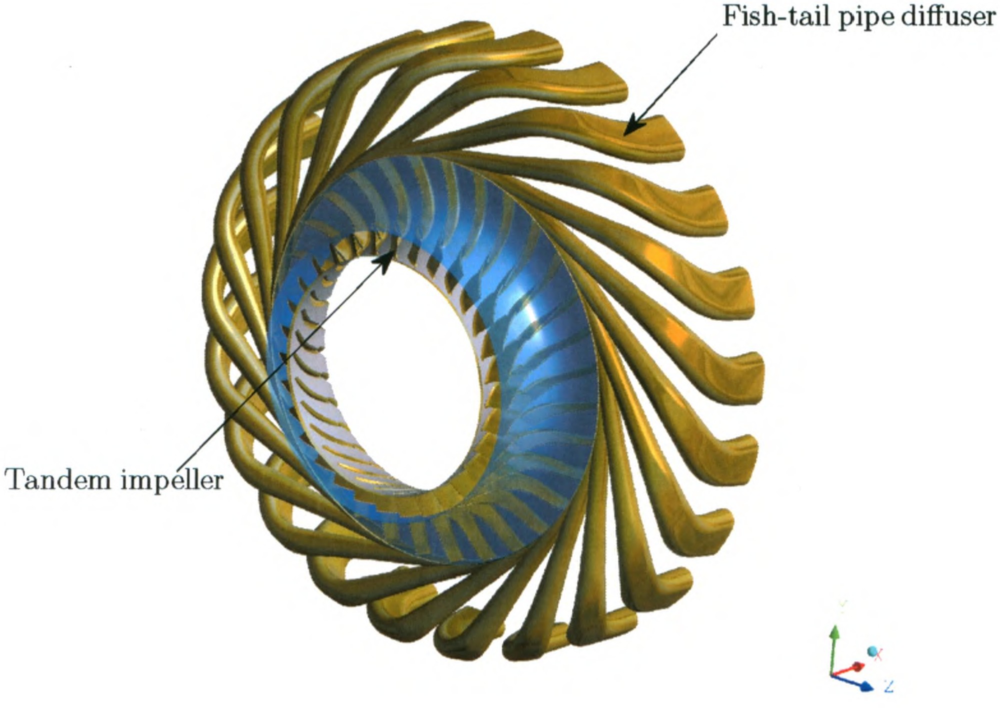

Figure 2.1: Centrifugal compressor stage studied.

By convention, the fluid velocity in a turbomachine is presented in either a stationary frame of reference where the velocity is denoted by $\vec{C}$, or in the frame of reference rotating with the impeller (the rotor) where the velocity is denoted by $\vec{W}$. The velocities in the two reference frames are related by

$$\vec{C} = \vec{W} + \vec{U} \tag{2.1}$$

where $\vec{U}$ is the local blade speed at radius $\vec{r}$ for rotational rate $\vec{\omega}$ giving $\vec{U} = \vec{\omega} \times \vec{r}$.

The most relevant description of velocity components in a turbomachine can be given with respect to one of two types of reference frame. The first description uses general cylindrical coordinates where components are given about the machine axis in terms of the local axial, circumferential, and radial directions (denoted with subscripts x, θ, r, respectively). Within the field of turbomachinery, a more descriptive set of components may sometimes be the local meridional, circumferential, and spanwise directions. This description is especially useful in centrifugal components where the gas path changes from axial to radial. The meridional direction references the local normal of the mean gas path direction in the meridional plane (a radial cut of the component). Such a meridional cut is shown in Fig. 2.2 for the impeller which also shows the normalized coordinate variable definitions in the impeller and diffuser.

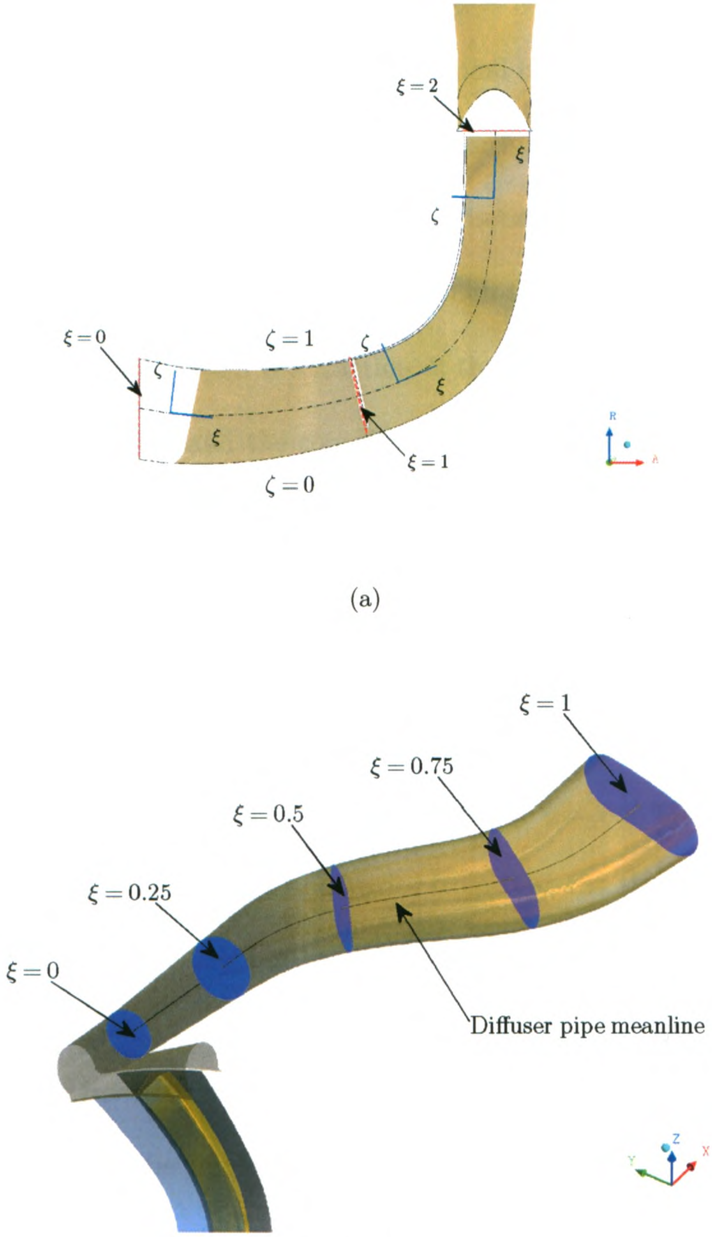

(a)

(b)

Figure 2.2: Streamwise coordinate definitions for (a) impeller and (b) diffuser components.

Herein, normalized coordinate variables are used where ξ denotes the local normalized streamwise coordinate (along the meridional direction in the impeller) and ζ which denotes the local normalized spanwise coordinate. In the impeller, ξ varies linearly from 0 at the inlet to 1 at the location between the inducer and exducer blades, and subsequently varies from 1 to 2 through the exducer section. Note that as defined, the coordinate system is a fraction of the meridional (streamwise) length through each blade section, and the coordinate is linear only within its own section since the inducer has a shorter meridional length than the exducer. The coordinate system as defined makes the location of the split between the two blades clear. The normalized span ζ is by definition zero at the hub surface and 1 at the shroud surface. Within the diffuser, the notion of a spanwise coordinate in the diffuser is ambiguous, and thus only a normalized streamwise coordinate, ξ, is given which is everywhere normal to the local pipe centreline and varies from 0 at the throat to 1 at the exit plane of the pipe.

The work input by the compressor on the fluid is related to the change in mean flow direction between the inlet and outlet of the rotor, and thus it is typical to describe the flow at inlet and outlet in terms of velocity triangles that describe the mean flow directions. The velocity triangles at impeller inlet and exit are shown in Fig. 2.3 where the relationship between the pitchwise velocity components and flow angles is clearly shown. Within the impeller, the mean flow is redirected by the impeller from a direction at the inlet that has primarily axial and circumferential components, $\vec{C}_1 \approx \langle C_{x1}, C_{\theta 1}, 0.0\rangle$ (i.e. the meridional direction at inlet is approximately axial), to a direction that has primarily radial and circumferential components, $\vec{C}_2 \approx \langle 0.0, C_{\theta 2}, C_{r2}\rangle$ (i.e. the meridional direction at exit is approximately radial). The conventional turbomachinery angles in the pitchwise direction of the stationary and relative frame velocities are denoted by α and β, respectively, where

$$\alpha = tan^{-1}\left(\frac{C_\theta}{C_m}\right) \tag{2.2}$$

$$\beta = tan^{-1}\left(\frac{W_\theta}{C_m}\right) \tag{2.3}$$

The flow angle in the meridional plane is denoted by ϕ where

$$\phi = tan^{-1}\left(\frac{C_r}{C_x}\right) \tag{2.4}$$

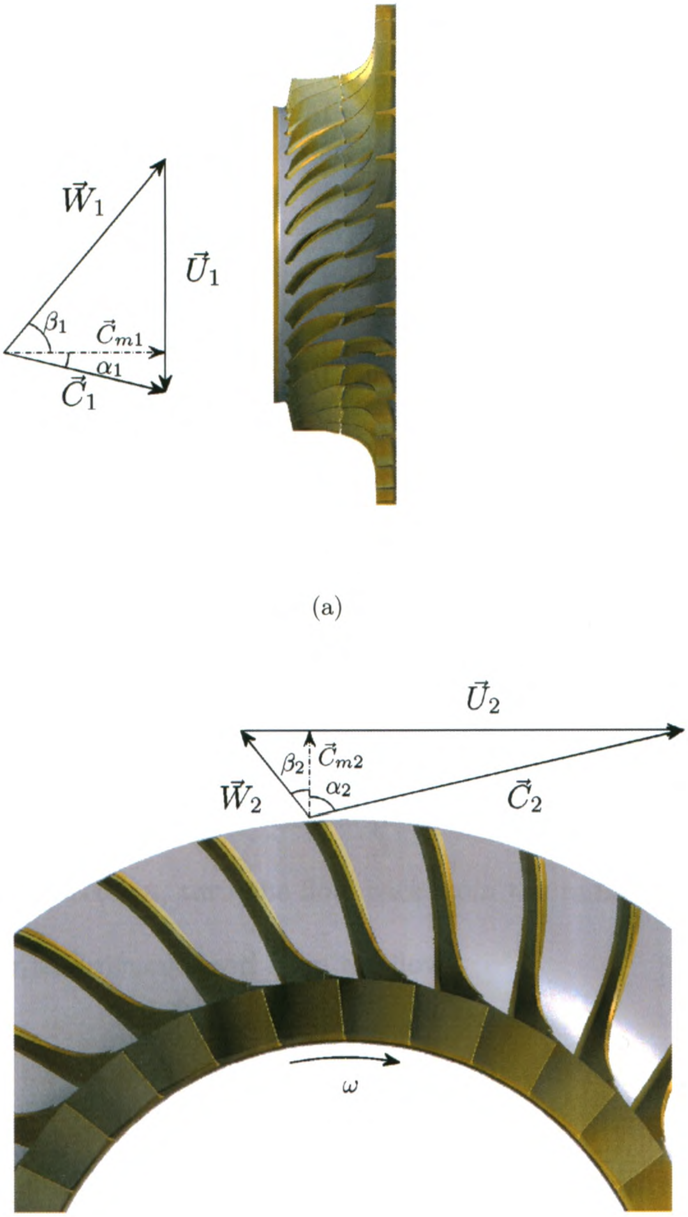

(a)

(b)

Figure 2.3: Impeller velocity triangle at (a) inlet and (b) exit.

Fig. 2.4 depicts an annotated view of a single impeller and single diffuser passage. Four locations are numbered which are, respectively, (1) the impeller inlet, (2) the impeller trailing edge, (3) the diffuser throat, and (4) the diffuser exit. These numbers will appear in variable subscripts throughout this work. The figure shows how the tandem impeller differs from a conventional impeller in that it has two distinct airfoils along the gas path of the component called the inducer blade and the exducer blade which are offset from one another circumferentially by a clocking-angle as described in Roberts and Kacker (2002). The fluid from the impeller exits into a fish-tail pipe diffuser, which is a type of discrete passage diffuser consisting of an arrangement of pipes at the radial exit of the impeller where the leading edges of the diffuser are formed by the intersections of adjacent pipes. The high-kinetic-energy flow exiting from the impeller is diffused by the fish-tail pipes which increase in cross-sectional area along the flow direction, turn the flow back from the radial direction towards the axial direction, and remove swirl from the flow.

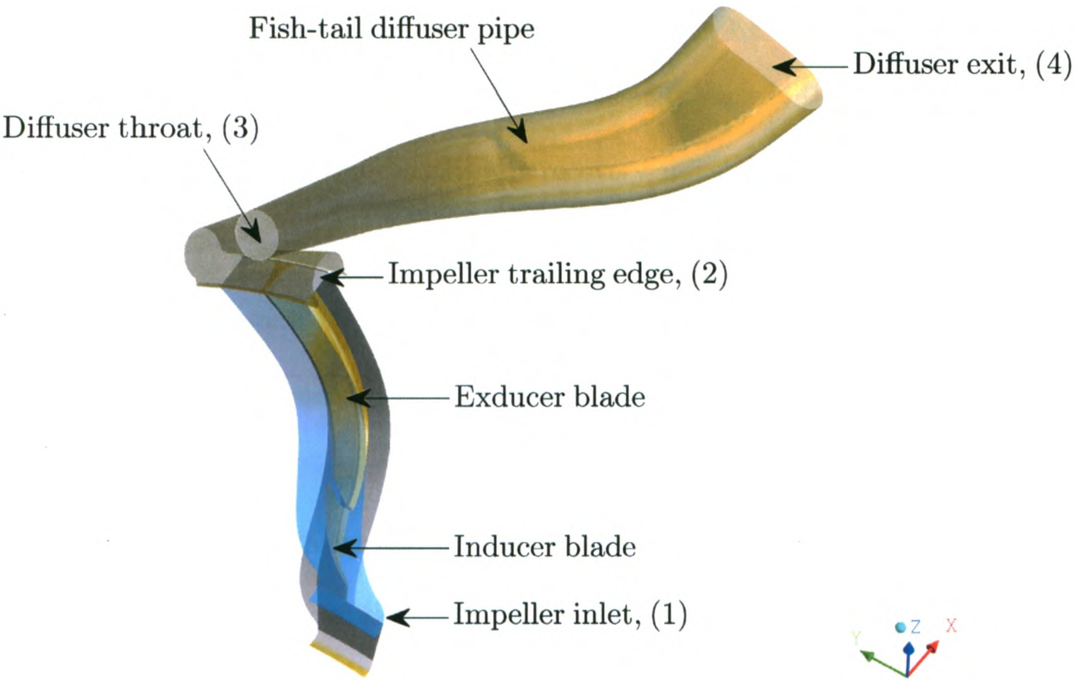

Figure 2.4: Single impeller and diffuser passage.

2.2 Description of the compressor stage

The impeller studied is unshrouded and tandem bladed. The stage studied has a medium pressure ratio, $\Pi_{4,01} \approx 2-3$, with subsonic leading edge relative and diffuser inlet Mach numbers. Both the impeller and diffuser components which are the subject of this study are fairly unconventional, and so some comments will be made concerning them.

Centrifugal stages with tandem impellers have been seen to have potential for improving the uniformity of the impeller exit velocity distribution, which could have benefits in improving the diffuser pressure recovery and stall margin as well as offering structural benefits over conventional designs (Roberts and Kacker, 2002). The price for these benefits were shown by Roberts and Kacker (2002) to be a penalty in efficiency. They compared a conventional single blade impeller against a tandem arrangement with 6 different clocking-angles (circumferential angle describing the relative positions of inducer and exducer blades). All arrangements were shown to have a lower efficiency than the conventional impeller, having total to total efficiency penalties between 0.5% for an in-line tandem arrangement and up to 3.8% for a clocking of 75% of the blade pitch angle.

Fish-tail pipe diffusers were developed for use in high performance centrifugal compressors as an improvement over more conventional cambered vane and flat plate diffusers, where an improvement in adiabatic efficiency of 6.8 to 8.8% was seen for the fish-tail type when used in 5:1 and 6:1 pressure ratio centrifugal compressor stages (Kenny, 1968). These improvements were attributed to the spanwise variation of the diffuser leading edge metal angle of the pipe diffuser metal angle (constant in the other diffusers studied) being more compatible with the flow field, as well as the swept leading edge being better suited to handle supersonic flow.

2.3 Review of centrifugal compressor studies

The highly complex flow occurring within turbomachinery stages is a particularly challenging problem computationally and numerous contradictory statements have been made as to what aspects of the flow are important for computations, some claiming that unsteady analysis ought to be used during the design process. This may be due in part to the unsatisfactory understanding of interaction mechanisms between the rotor and stator which is due in part to the difficulty of investigating the phenomenon both experimentally and numerically. Ziegler *et al.* (2003a,b) conducted an experimental investigation into impeller-diffuser interaction on a compressor they call the "Radiver" compressor. They described the impeller-diffuser interaction in a centrifugal compressor as the group of mechanisms which cause differences in performance and flow phenomena in the components when the components are being operated in isolation or when they are operated together. The main influences of the impeller on the diffuser are

(a) Unsteadiness originating from the distorted flow field in the exit of the impeller seen at the inlet of the diffuser. These in particular play a large role in mixing processes.

(b) The spanwise distribution of Mach number and flow angle at the inlet of the diffuser, fundamental to how the diffuser will function.

There are also possibly significant effects of the diffuser on the impeller which include

(a) The unsteady pressure disturbance caused by the diffuser vanes (or in the case of the fishtail diffuser, the leading edges of the pipes) on the upstream impeller flow.

(b) The shape of the inlet of a vaneless diffuser, or the presence of a vaneless diffuser influences the flow in the impeller.

The authors of these studies concluded that only transient simulations may be capable of predicting important flow phenomena for proper design of centrifugal compressor stages (in particular, they mention the design of the radial gap between the impeller and diffuser). However, their results were made available as an open CFD case, and the recent computational studies of Smirnov *et al.* (2007) for the "Radiver" compressor indicate that transient simulations may have no definite advantage over steady-state simulations using the mixing plane approach. This may not be true over the whole speedline, however. When predicting cases near stall or surge, unsteady simulations may in fact be necessary. Merz *et al.* (2004) discuss an axial compressor stage for which they have undertaken numerical studies with two turbulence models, the standard $k-\omega$ model, and an advanced $k-\epsilon$ model. The cases examined by these authors were for a high tip-clearance impeller and were near the stall point and they found that unsteady simulations were more accurate than steady-state isolated rotor simulations. In their studies, the advanced $k-\epsilon$ model showed better agreement with experimentally obtained performance parameters (efficiencies, pressure ratios, and temperature ratios). The accurate prediction of the compressor flow field close to stall may require unsteady calculations due to unsteady phenomena such as vortex shedding from the blade tip and trailing edge as well as flow separation on the blade.

Unsteady analysis, however, incurs computational costs that are out of the scope of feasibility for iterative aerodynamic design (Roberts and Steed, 2004). Steady-state analysis is thus necessary to meet the requirements for rapid turn-arounds of design iterations. For confidence that steady-state models are predicting physically realistic phenomena, they must be assessed with respect to the best available knowledge base for such turbomachinery components. This knowledge base includes other more complicated numerical analyses or perhaps best of all, experimental results. This is the primary motivation behind the current investigation into mixing plane calculations of the studied centrifugal compressor stage.

The reason why steady-state mixing plane simulations may be capable of predicting the flow field sufficiently for designers over most of the speedline goes back to one of the earliest 3-D Navier Stokes simulations of a centrifugal compressor by Dawes (1995). The simulations of Dawes (1995) studied the Krain impeller (Krain, 1988) with a vaned diffuser using the $k - \epsilon$ turbulence model. It was shown that despite the presence of flow unsteadiness in the region between the exit of the impeller and the entry zone of the diffuser, the effect of the unsteadiness on the overall flow field was of little importance when compared to a steady-state simulation of the diffuser with the time-averaged flow incidence in the spanwise direction applied uniformly across the inlet of the diffuser. It was concluded that mixing models should only mix out the circumferential component of the velocity, and not the spanwise variation that is found at the impeller exit, a condition which is satisfied by the mixing planes used herein. The study also provided a comparison of the time-averaged entropy generation rate, and little loss was directly attributable to unsteady effects.

Shum *et al.* (2000) used Dawes' code and the $k - \epsilon$ turbulence model, and compared unsteady stage simulations to steady-state isolated diffuser calculations where boundary conditions were taken as time averages from the unsteady simulations. For the compressor studied, the blade to vane ratio was changed to 1:1 to avoid modeling the full annulus. The study focused on what factors make the most significant contributions to performance parameters. They conclude that the steady state flow angle alignment with the diffuser vane is the single most important factor that determines diffuser performance.

It may be noted that a number of different turbulence models have been used in these studies. It has been made apparent that the choice of turbulence modeling in both centrifugal and axial compressor stages significantly affects the quality of predictions in a numerical investigation. Studies investigating turbulence modeling effects on simulations include, for example, the axial compressor study of Shabbir *et al.* (1996) and the study of the centrifugal stage in Roberts and Steed (2004).

2.4 Motivation for the current study

Certain deficiencies were seen in the previous isolated component CFD methodology for compressor design. Unsteady simulations on the other hand are excessively expensive computationally to meet the needs of a high turn-around for aerodynamic design iterations. Roberts and Steed (2004) showed that the mixing plane methodology can be used to obtain much better performance data for the design of centrifugal stages. The methodology, however, has not been sufficiently validated. The studies herein present a number of numerical experiments into the usage of more detailed geometry by including blade fillets in computations, by extending the computational domain downstream of the diffuser exit to include a plenum to examine the effect of the boundary location, and varying the turbulence models used to examine the effects on the flow field and performance parameters. Experimental studies are also undertaken which can be used as a comparison to the predicted flow field to assess whether the mixing plane approach accurately predicts the true physical mean flow field in the compressor.

2.5 Summary

The necessary description of compressor stage geometry, notation, and turbomachinery conventions has been outlined in this chapter, and a review of previous studies and the motivation for the current study has been outlined. Before describing the details of the numerics particular to the simulations conducted herein, the following chapter describes the general CFD methodology used for calculating the mean flow field for a compressible turbulent flow. The averaging of the governing equations is described and the turbulence models employed herein are briefly presented. These turbulence models are necessary for the closure of the mean flow conservation equations.

Chapter 3

Numerical simulations of compressible turbulent flows

The flow field within the centrifugal compressor stage is predicted using three eddy-viscosity turbulence models (two-equation models) and one second order closure model and the predictions are assessed in Chapter 8. The eddy-viscosity turbulence models analyzed are the standard $k-\epsilon$ model, the hybrid $k-\epsilon/k-\omega$ model referred to as the SST model, and a modified version of the SST model denoted SST-RM. The second order closure model used is the Speziale, Sarkar, and Gatski Reynolds Stress Model (RSM-SSG). Herein, a general discussion of turbulence modeling in CFD is provided that is indebted primarily to reviews in Schlichting and Gersten

(2000) and Wilcox (2006), as well as to the documentation in ANSYS (2006). Following this, some brief comments about each model are made along with the closure relationships for each. The interested reader is directed to the literature for a more detailed discussion.

3.1 Turbulence closure modeling

Turbulence is an unsteady, three-dimensional, complex flow process consisting of a wide spectrum of scales. The equations governing a turbulent compressible flow as is found in a compressor stage are the equations for the conservation of mass, momentum, and energy. The momentum equations solved include the viscous terms and apply the Stokes assumption about a zero bluk viscosity and therefore are the well known Navier-Stokes equations for Newtonian fluids. A brief derivation of the conservation equations in their differential conservative form is given in Appendix A. The direct numerical simulation (DNS) of the Navier-Stokes equations, especially for complex flows such as those encountered in turbomachinery, requires much more computing power than is practically feasible. For practical flow calculations, different turbulence modeling approaches have been developed that can be used with a much lower computational cost.

Typically only the mean flow field is of particular interest, so the time dependent governing equations for statistically steady turbulent flows are either averaged as by Reynolds (1895), or in a way that is suitable particularly for compressible flows, as by Favre (1965a,b). A problem arises, however, when setting up the equations for the mean flow: the averaging of the nonlinear convective terms in the Navier-Stokes equations lead to additional unknown terms in the mean flow equations (the Reynolds stresses) that are a function of the turbulent fluctuating variables. The mean flow equations are called the Reynolds Averaged Navier Stokes (RANS) equations after their originator. In order to close the system of equations, model equations for the unknown Reynolds stress terms must be supplemented. Usually the turbulence model equations are constructed by deriving the exact form of the governing equations for the terms involving turbulence properties, and approximations of the unknown correlation terms that appear in these exact averaged equations are made in terms of known flow properties based on empirical data.

3.1.1 Reynolds Averaged Navier-Stokes Equations

The instantaneous values of field variables in statistically stationary turbulent flows (i.e. turbulent flows which have statistics that are constant in time, particularly the mean and standard deviation of the field variables) can be decomposed as by Reynolds (1895) as a sum of the mean quantity and a fluctuation about the mean

$$\phi(t) = \overline{\phi} + \phi'(t) \tag{3.1}$$

where ϕ denotes an arbitrary field variable which could be u, v, w, p, T, ρ, etc., and where the overbar denotes a time average and a prime denotes a fluctuation.

The Reynolds time average is given by

$$\overline{\phi} = \lim_{t\to\infty} \frac{1}{t} \int_0^t \phi(t)dt \tag{3.2}$$

where the averaging time, t, is large enough that the average is independent of time. Note that this relation implies that the time average of the fluctuations is identically zero,

$$\overline{\phi'} = 0 \tag{3.3}$$

Typically, the following rules for time averaging are also stated (Schlichting and Gersten, 2000), easily derivable from the definition of the Reynolds average above,

$$\overline{\overline{\phi}} = \overline{\phi} \tag{3.4}$$

$$\overline{\phi + \psi} = \overline{\phi} + \overline{\psi} \tag{3.5}$$

$$\overline{\overline{\phi}\psi} = \overline{\phi}\,\overline{\psi} \tag{3.6}$$

$$\overline{\frac{\partial \phi}{\partial s}} = \frac{\partial \overline{\phi}}{\partial s} \tag{3.7}$$

$$\overline{\int \phi ds} = \int \overline{\phi} ds \tag{3.8}$$

Reynolds averaging is suitable for the derivation of the incompressible RANS equations. However, when dealing with a compressible flow, Favre averages (Favre, 1965a,b) reduce the complexity of the mean flow equations for flows where compressibility effects are important. It is noted, though, that the more simple mathematical form of the equations does not reduce the complexity of the actual physics of these flows, but changes the definition of the mean and fluctuating components that are being dealt with. The Favre average is a mass weighted average given by

$$\tilde{\phi} = \frac{1}{\overline{\rho}} \lim_{t \to \infty} \frac{1}{t} \int_0^t \rho \phi dt = \frac{\overline{\rho \phi}}{\overline{\rho}} \tag{3.9}$$

where the time dependent variable is split as

$$\phi(t) = \tilde{\phi} + \phi''(t) \tag{3.10}$$

Note, with these definitions

$$\overline{\rho} \tilde{\phi} = \overline{\rho \phi} \tag{3.11}$$

$$\overline{\rho \phi''} = 0 \tag{3.12}$$

$$\overline{\phi''} \neq 0 \tag{3.13}$$

Time averages of the equations of mass, momentum, and energy conservation are required, and the averaged equations are used to find the mean flow field for fully turbulent flows. The continuity equation for compressible flow (see Eq. (A.3)) is given by

$$0 = \frac{\partial \rho}{\partial t} + \frac{\partial}{\partial x_i}\left(\rho u_i\right) \tag{3.14}$$

To find the mean continuity equation, this equation is time averaged assuming the flow is statistically stationary. If the equation is averaged using the two averaging methods, it can be seen that Favre averaging simplifies the mathematics for the averaged compressible flow equations. Simple Reynolds averaging gives

$$\begin{aligned}
0 =& \overline{\frac{\partial \rho}{\partial t} + \frac{\partial\left(\rho u_i\right)}{\partial x_i}} \\
=& \frac{\partial \bar{\rho}}{\partial t} + \frac{\partial\left(\overline{\rho u_i}\right)}{\partial x_i} \\
=& \frac{\partial \bar{\rho}}{\partial t} + \frac{\partial\left[\overline{\left(\bar{\rho}+\rho'\right)\left(\overline{u_i}+u_i'\right)}\right]}{\partial x_i} \\
=& \frac{\partial \bar{\rho}}{\partial t} + \frac{\partial\left(\bar{\rho}\,\overline{u_i}\right)}{\partial x_i} + \frac{\partial\left(\overline{\bar{\rho} u_i'}\right)}{\partial x_i} + \frac{\partial\left(\overline{\rho' \overline{u_i}}\right)}{\partial x_i} + \frac{\partial\left(\overline{\rho' u_i'}\right)}{\partial x_i}
\end{aligned}$$

and finally noting that averages of fluctuating quantities are zero, Eq. 3.3,

$$0 = \frac{\partial \bar{\rho}}{\partial t} + \frac{\partial \left(\bar{\rho}\bar{u}_i\right)}{\partial x_i} + \frac{\partial \left(\overline{\rho' u_i'}\right)}{\partial x_i} \tag{3.15}$$

However, if Favre averaging is used for the velocity components,

$$\begin{aligned} 0 =& \overline{\frac{\partial \rho}{\partial t} + \frac{\partial \left(\rho u_i\right)}{\partial x_i}} \\ =& \frac{\partial \bar{\rho}}{\partial t} + \frac{\partial \left(\overline{\rho u_i}\right)}{\partial x_i} \end{aligned}$$

Eq. (3.11) is then applied and the Favre averaged continuity equation is found,

$$0 = \frac{\partial \bar{\rho}}{\partial t} + \frac{\partial \left(\bar{\rho}\tilde{u}_i\right)}{\partial x_i} \tag{3.16}$$

where Eq. (3.16) is of the same mathematical form as the unaveraged continuity equation and simpler than the Reynolds averaged equivalent, Eq. (3.15).

In addition to the equation for the conservation of mass, we also need an equation for the conservation of momentum. The momentum equation for a Newtonian fluid is used (see Eq. (A.7)),

$$\frac{\partial \left(\rho u_i\right)}{\partial t} + \frac{\partial \left(\rho u_i u_j\right)}{\partial x_j} = -\frac{\partial p}{\partial x_j} + \frac{\partial t_{ji}}{\partial x_j} \tag{3.17}$$

Averaging the momentum equation gives

$$\overline{\frac{\partial\left(\rho u_i\right)}{\partial t}+\frac{\partial\left(\rho u_i u_j\right)}{\partial x_j}}=\overline{-\frac{\partial p}{\partial x_j}+\frac{\partial t_{ji}}{\partial x_j}}$$

$$\frac{\partial\left(\overline{\rho u_i}\right)}{\partial t}+\frac{\partial\left(\overline{\rho u_i u_j}\right)}{\partial x_j}=-\frac{\partial\overline{p}}{\partial x_j}+\frac{\partial\overline{t_{ji}}}{\partial x_j}$$

$$\frac{\partial\left(\overline{\rho}\tilde{u}_i\right)}{\partial t}+\frac{\partial\left(\overline{\rho(\tilde{u}_i+u_i'')(\tilde{u}_j+u_j'')}\right)}{\partial x_j}=-\frac{\partial\overline{p}}{\partial x_j}+\frac{\partial\overline{t_{ji}}}{\partial x_j}$$

and thus

$$\frac{\partial\left(\overline{\rho}\tilde{u}_i\right)}{\partial t}+\frac{\partial\left(\overline{\rho}\tilde{u}_i\tilde{u}_j\right)}{\partial x_j}=-\frac{\partial\overline{p}}{\partial x_j}+\frac{\partial\left(\overline{t_{ji}}-\overline{\rho u_i''u_j''}\right)}{\partial x_j} \tag{3.18}$$

From this equation, it may be seen that the averaged momentum equation has the same form as the unaveraged equation with one difference: there is an extra second order tensor term with dimensions of stress. This tensor which is referred to as the Reynolds stress tensor which has the effect on the mean flow of apparently increasing the viscosity of the fluid (since $-\overline{\rho u_i''u_j''}$ is typically positive). The tensor is defined in terms of a stress per unit density,

$$\overline{\rho}\tau_{ij}=-\overline{\rho u_i''u_j''} \tag{3.19}$$

Eq. (3.18) is then written as

$$\frac{\partial\left(\overline{\rho}\tilde{u}_i\right)}{\partial t}+\frac{\partial\left(\overline{\rho}\tilde{u}_i\tilde{u}_j\right)}{\partial x_j}=-\frac{\partial\overline{p}}{\partial x_j}+\frac{\partial\left(\overline{t_{ji}}+\overline{\rho}\tau_{ji}\right)}{\partial x_j} \tag{3.20}$$

In a similar way the Favre averaged total energy equation can be obtained and is given by

$$\begin{aligned} \frac{\partial\left(\overline{\rho}\tilde{h}_o\right)}{\partial t}+\frac{\partial\left(\overline{\rho}\tilde{h}_o\tilde{u}_j\right)}{\partial x_j}&=\frac{\partial\overline{p}}{\partial t} \\ &+\frac{\partial}{\partial x_j}\left[-\overline{q}_j-\overline{\rho h''u_j''}+\overline{t_{ji}u_i''}-1/2\overline{\rho u_i''u_i''u_j''}+(t_{ij}+\overline{\rho}\tau_{ij})\tilde{u}_i\right] \end{aligned} \tag{3.21}$$

To establish model equations for the unknown terms involving correlations of fluctuating quantities, a detailed understanding of the physical processes of the turbulent fluctuations is needed. As Schlichting and Gersten (2000) point out, this includes the understanding that the apparent stresses are mainly produced by the large-scale eddies in the flow. Instability then causes flow in the smaller scales to follow, and then high velocity gradients, $\partial u''/\partial x$, etc. will occur in the smallest eddies such that energy is transformed into internal energy. This means energy is transferred from the main flow to the large eddies through the apparent stresses (which are notably independent of the viscosity) and subsequently transferred to smaller and smaller-scale eddies until energy is dissipated in the smallest scales. This mechanism accounts for the fact that in turbulent flows the friction drag and the average velocity distribution have only slight Reynolds number dependence even though all energy losses are due to the viscosity.

3.1.2 The Reynolds stress and turbulent kinetic energy transport equations

An exact (i.e. un-modeled) transport equation for the Reynolds stresses can be obtained by performing operations on the Navier Stokes equations and averaging. This will be important not only for the Reynolds stress models, but it also yields upon contraction what is commonly referred to as the k-equation, a transport equation for the turbulence kinetic energy common to most one- and two-equation turbulence models.

The differential equation for the Reynolds stress tensor can be found by taking the momentum equation for velocity component u_i and multiplying it by the velocity fluctuation in the j direction, u_j'', then adding it to the momentum equation for velocity component u_j multiplied by the velocity fluctuation in the i direction, u_i'' and time averaging in the same way as with the RANS equations. After some algebraic manipulation, the averaged Reynolds stress equation, which can be found for example in Wilcox (2006), reads

$$\begin{aligned}\frac{\partial}{\partial t}(\overline{\rho}\tau_{ij}) + \frac{\partial}{\partial x_k}(\overline{\rho}\tilde{u}_k\tau_{ij}) &= -\overline{\rho}\tau_{ik}\frac{\partial \tilde{u}_j}{\partial x_k} - \overline{\rho}\tau_{jk}\frac{\partial \tilde{u}_i}{\partial x_k} + \overline{\rho}\epsilon_{ij} + \overline{\rho}\Pi_{ij} \\ &+ \frac{\partial}{\partial x_k}\left[-\overline{(t_{kj}u_i'' + t_{ki}u_j'')} + \overline{\rho}C_{ijk}\right] + \overline{u_i''}\frac{\partial \bar{p}}{\partial x_j} + \overline{u_j''}\frac{\partial \bar{p}}{\partial x_i}\end{aligned} \tag{3.22}$$

with the pressure-strain correlation, the dissipation rate correlation, and the third-order diffusion correlation given by

$$\overline{\rho}\Pi_{ij} = \overline{p'\left(\frac{\partial u_i''}{\partial x_j} + \frac{\partial u_j''}{\partial x_i}\right)} \tag{3.23}$$

$$\overline{\rho}\epsilon_{ij} = \overline{t_{kj}\frac{\partial u_i''}{\partial x_k} + t_{ki}\frac{\partial u_j''}{\partial x_k}} \tag{3.24}$$

$$\overline{\rho}C_{ijk} = \overline{\rho u_i'' u_j'' u_k''} + \overline{p' u_i''}\delta_{jk} + \overline{p' u_j''}\delta_{ik} \tag{3.25}$$

Contracting the Reynolds stress equation yields the k-equation, which is

$$\begin{aligned}\frac{\partial}{\partial t}(\overline{\rho}k) + \frac{\partial}{\partial x_j}(\overline{\rho}\tilde{u}_j k) = &- \overline{\rho}\tau_{ij}\frac{\partial \tilde{u}_i}{\partial x_j} - \overline{\rho}\epsilon + \frac{\partial}{\partial x_j}\left(\overline{t_{ji}u_i''} - 1/2\overline{\rho u_i'' u_i'' u_j''} - \overline{p' u_j''}\right)\\ &- \overline{u_i''}\frac{\partial \bar{p}}{\partial x_i} - \overline{p'\frac{\partial u_i''}{\partial x_i}}\end{aligned} \tag{3.26}$$

3.2 Closure of the RANS equations

3.2.1 The Boussinesq approximation

Many of the common turbulence models which require the need to solve only one or two extra equations for the Reynolds stresses (where there are 6 independent components of the tensor) use the Boussinesq eddy-viscosity assumption, (Boussinesq, 1877), in order to compute the Reynolds stresses. The Reynolds stress tensor is computed as the product of some eddy-viscosity and the mean strain-rate tensor. In analogy to the Newtonian friction law where the viscous stress is taken to be of the form given by Eq. (A.8), the Boussinesq approximation takes the turbulent stresses to be of the form

$$\overline{\rho}\tau_{ij} = \mu_T S_{ij} - \frac{2}{3}\delta_{ij}\left(\overline{\rho}k + \mu_T\frac{\partial u_k}{\partial x_k}\right) \tag{3.27}$$

where μ_T is the eddy (or turbulent) viscosity which, unlike the molecular viscosity, is not a property of the fluid, but rather is a property of the flowfield and, in general, varies with position.

3.2.2 Modeled governing equations

The momentum and total energy equations have terms which are unknowns in terms of correlations with fluctuating quantities. These equations need to be modeled to close the system of equations.

Using the Boussinesq approximation for the Reynolds stress tensor and substituting the Newtonian viscous stress tensor, the momentum equation becomes

$$\begin{aligned}\frac{\partial\left(\overline{\rho}\tilde{u}_i\right)}{\partial t} + \frac{\partial\left(\overline{\rho}\tilde{u}_i\tilde{u}_j\right)}{\partial x_j} &= -\frac{\partial\overline{p}}{\partial x_j} \\ &+ \frac{\partial}{\partial x_j}\left[\left(\mu+\mu_T\right)\left(\frac{\partial u_i}{\partial x_j} + \frac{\partial u_j}{\partial x_i} - \frac{2}{3}\delta_{ij}\frac{\partial u_k}{\partial x_k}\right)\right] - \frac{2}{3}\overline{\rho}k\end{aligned} \tag{3.28}$$

This is the form of the momentum equation solved numerically for eddy-viscosity turbulence models. For Reynolds stress turbulence models, model equations for each component of the Reynolds stress tensor are solved. As the tensor is symmetric, it has 6 independent components, so 6 equations are solved, as well as another equation for the dissipation rate. In the above form, the eddy-viscosity, μ_T, is yet to be defined, and is dependent on the particular turbulence model used.

The total energy equation, Eq. (3.21), also contains terms which are unknowns, and it is modeled as

$$\frac{\partial\left(\overline{\rho}\tilde{h}_o\right)}{\partial t}+\frac{\partial\left(\overline{\rho}\tilde{h}_o\tilde{u}_j\right)}{\partial x_j}=\frac{\partial\overline{p}}{\partial t}+\frac{\partial}{\partial x_j}\left(\kappa\frac{\partial\tilde{T}}{\partial x_j}-\frac{\mu_T}{Pr_T}\frac{\partial\tilde{h}}{\partial x_j}+(\bar{t}_{ij}+\overline{\rho}\tau_{ij})\tilde{u}_i\right) \tag{3.29}$$

3.2.3 Closure of the eddy viscosity

The model equations to close the eddy-viscosity terms for the $k-\epsilon$ and SST models are presented herein.

3.2.3.1 The k-ϵ model

The standard $k-\epsilon$ model is the model usually credited to Jones and Launder (1973), but with the re-tuned constants of Launder and Sharma (1974). It models equations for the turbulence kinetic energy and turbulence eddy dissipation and uses the Boussinesq approximation to relate these parameters to the unknown Reynolds stresses.

The k-ϵ model closes the eddy viscosity term by relating it to the turbulent kinetic energy, k, and dissipation, ϵ as follows

$$\mu_T = C_\mu \overline{\rho} \frac{k^2}{\epsilon} \tag{3.30}$$

Obviously, now two new unknowns, k and ϵ, are introduced into the system of equations, and they are found by solving modeled transport equations for each. These equations are given as follows

$$\frac{\partial}{\partial t}(\overline{\rho} k) + \frac{\partial}{\partial x_j}(\overline{\rho} \tilde{u}_j k) = \frac{\partial}{\partial x_j}\left[\left(\mu + \frac{\mu_T}{\sigma_k}\right)\frac{\partial k}{\partial x_j}\right] + P_k - \overline{\rho}\epsilon \tag{3.31}$$

and

$$\frac{\partial}{\partial t}(\overline{\rho} \epsilon) + \frac{\partial}{\partial x_j}(\overline{\rho} \tilde{u}_j \epsilon) = \frac{\partial}{\partial x_j}\left[\left(\mu + \frac{\mu_T}{\sigma_\epsilon}\right)\frac{\partial \epsilon}{\partial x_j}\right] + \frac{\epsilon}{k}\left(C_{\epsilon 1} P_k - C_{\epsilon 2}\overline{\rho}\epsilon\right) \tag{3.32}$$

with the production of turbulence kinetic energy given by

$$P_k = \mu_T \frac{\partial \tilde{u}_i}{\partial x_j}\left(\frac{\partial \tilde{u}_i}{\partial x_j} + \frac{\partial \tilde{u}_j}{\partial x_i}\right) - \frac{2}{3}\frac{\partial \tilde{u}_j}{\partial x_j}\left(3\mu_T \frac{\partial \tilde{u}_k}{\partial x_k} + \bar{\rho} k\right) \tag{3.33}$$

The closure coefficients take the following values for the k-ϵ model

$C_{\epsilon 1} = 1.44$ $\quad C_{\epsilon 2} = 1.92$ $\quad C_\mu = 0.09$

$\sigma_k = 1.0$ $\quad \sigma_\epsilon = 1.3$

3.2.3.2 The SST k-ω model

The Shear Stress Transport (SST) model of Menter (1994) is essentially a zonal turbulence model with smart functions that change between two sub-models according to the local flow regime that is being computed (requiring no user specification of different regimes). It was developed in the spirit of trying to improve upon the status of two-equation turbulence closure models in predicting adverse pressure gradient flows, especially the onset of separation, and was seen to be advantageous relative to the sub-models that it was based upon in terms of prediction of the location of separation and the displacement effect associated with it. The model consists of a blending of the equations such that the SST model would retain the robustness and accuracy associated with the Wilcox $k - \omega$ model (Wilcox, 1998) near the wall in the viscous sublayer and the logarithmic part of the boundary layer, while retaining the freestream independence and the more accurate prediction of free-shear layers obtained by the Jones-Launder $k - \epsilon$ model (Jones and Launder, 1973). The SST model switches to the $k - \epsilon$ model away from surfaces where blending happens in the wake region of the boundary layer.

In addition, the model uses a modified definition of the eddy-viscosity in regions of adverse pressure-gradient in order to account for the transport of the principal turbulent shear stress. The modified definition of the eddy-viscosity comes from an enforcement of the assumption (Bradshaw *et al.*, 1967) that the principal turbulent shear stress in a boundary layer is proportional to the turbulence kinetic energy, a fact which does not hold with the standard definition in two-equation turbulence models when the ratio of production to dissipation is significantly higher than one. This assumption does not hold for free-shear flows and, thus, another blending function is used to recover the original eddy-viscosity formulation. The SST model was shown to agree more closely with many test cases than either the Wilcox $k-\omega$ model or the Jones and Launder $k-\epsilon$ model (Menter, 1994).

The formation of the SST equations is as follows. First, the Wilcox k-ω transport equations are written as

$$\frac{\partial}{\partial t}(\overline{\rho}k)+\frac{\partial}{\partial x_j}(\overline{\rho}\tilde{u}_jk)=\frac{\partial}{\partial x_j}\left[\left(\mu+\frac{\mu_T}{\sigma_{k1}}\right)\frac{\partial k}{\partial x_j}\right]+P_k-\beta'\overline{\rho}k\omega \tag{3.34}$$

and

$$\frac{\partial}{\partial t}(\overline{\rho}\omega)+\frac{\partial}{\partial x_j}(\overline{\rho}\tilde{u}_j\omega)=\frac{\partial}{\partial x_j}\left[\left(\mu+\frac{\mu_T}{\sigma_{\omega1}}\right)\frac{\partial \omega}{\partial x_j}\right]+\alpha_1\frac{\omega}{k}P_k-\beta_1\overline{\rho}\omega^2 \tag{3.35}$$

Likewise, the k-ϵ equations transformed into k-ω transport equations are

$$\frac{\partial}{\partial t}(\overline{\rho}k)+\frac{\partial}{\partial x_j}(\overline{\rho}\tilde{u}_jk)=\frac{\partial}{\partial x_j}\left[\left(\mu+\frac{\mu_T}{\sigma_{k2}}\right)\frac{\partial k}{\partial x_j}\right]+P_k-\beta'\overline{\rho}k\omega \tag{3.36}$$

and

$$\begin{aligned}\frac{\partial}{\partial t}(\overline{\rho}\omega)+\frac{\partial}{\partial x_j}(\overline{\rho}\tilde{u}_j\omega)=&\frac{\partial}{\partial x_j}\left[\left(\mu+\frac{\mu_T}{\sigma_{\omega 2}}\right)\frac{\partial\omega}{\partial x_j}\right]+2\bar{\rho}\frac{1}{\sigma_{\omega 2}\omega}\frac{\partial k}{\partial x_j}\frac{\partial\omega}{\partial x_j}\\&+\alpha_2\frac{\omega}{k}P_k-\beta_2\overline{\rho}\omega^2\end{aligned}\tag{3.37}$$

The Wilcox equations, Eqs. (3.34) and (3.35), are then multiplied by the blending function, F_1, and the Jones-Launder equations, Eqs. (3.36) and (3.37), are multiplied by $(1-F_1)$ and added together. The SST transport equations then read

$$\frac{\partial}{\partial t}(\overline{\rho}k)+\frac{\partial}{\partial x_j}(\overline{\rho}\tilde{u}_jk)=\frac{\partial}{\partial x_j}\left[\left(\mu+\frac{\mu_T}{\sigma_{k3}}\right)\frac{\partial k}{\partial x_j}\right]+P_k-\beta'\overline{\rho}k\omega\tag{3.38}$$

and

$$\begin{aligned}\frac{\partial}{\partial t}(\overline{\rho}\omega)+\frac{\partial}{\partial x_j}(\overline{\rho}\tilde{u}_j\omega)=&\frac{\partial}{\partial x_j}\left[\left(\mu+\frac{\mu_T}{\sigma_{\omega 3}}\right)\frac{\partial\omega}{\partial x_j}\right]+(1-F_1)2\bar{\rho}\frac{1}{\sigma_{\omega 2}\omega}\frac{\partial k}{\partial x_j}\frac{\partial\omega}{\partial x_j}\\&+\alpha_3\frac{\omega}{k}P_k-\beta_3\overline{\rho}\omega^2\end{aligned}\tag{3.39}$$

All coefficients with subscript 3, namely $\sigma_{k3},\sigma_{\omega 3},\alpha_3,\beta_3$, are functions of the blending function F_1, given by

$$\Phi_3=F_1\Phi_1+(1-F_1)\Phi_2\tag{3.40}$$

The constant closure coefficients are given by

$\beta'=0.09$ $\alpha_1=5/9$ $\beta_1=0.075$ $\sigma_{k1}=2.0$

$\sigma_{\omega 1}=2.0$ $\alpha_2=0.44$ $\beta_2=0.0828$ $\sigma_{k2}=1.0$

$\sigma_{\omega 2}=1.0/0.856$

To better predict the onset and amount of separation, the proposed modification of the eddy viscosity with a limiter is given as follows

$$\nu_T = \frac{\mu_T}{\bar{\rho}} = \frac{a_1 k}{max(a_1\omega, SF_2)} \tag{3.41}$$

with

$$a_1 = 0.3 \tag{3.42}$$

The blending functions are defined as

$$F_1 = tanh(arg_1^4) \tag{3.43}$$

$$F_2 = tanh(arg_2^2) \tag{3.44}$$

where the arguments are functions of the distance of a point from the closest no-slip boundary, y,

$$arg_1 = min\left[max\left(\frac{\sqrt{k}}{\beta'\omega y}, \frac{500\nu}{y^2\omega}\right), \frac{4\rho k}{CD_{k\omega}\sigma_{\omega 2}y^2}\right] \tag{3.45}$$

$$arg_2 = max\left(\frac{2\sqrt{k}}{\beta'\omega y}, \frac{500\nu}{y^2\omega}\right) \tag{3.46}$$

and

$$CD_{k\omega} = max\left(2\rho\frac{1}{\sigma_{\omega 2}\omega}\frac{\partial k}{\partial x_j}\frac{\partial \omega}{\partial x_j}, 10^{-10}\right) \tag{3.47}$$

3.2.3.3 The SST-RM k-ω model

Menter recently tried to improve the predictions of the SST model for reattaching flows (personal communication, 2008). The SST model was optimized for the prediction of separation, but studies with the model predicted a premature onset of axial compressor stall. Contrarily, for models that tended to predict a delayed onset of separation, such as the $k-\epsilon$ and $k-\omega$ models, a more realistic stall point was predicted, although it was thought that this effect may only be due to a cancellation of errors due to the delayed prediction of separation. The idea behind the modification was that the underlying problem with the SST model was not a premature prediction of separation, but a general deficiency of RANS turbulence models with modeling separated regions. The modification of the SST model was seen to improve predictions for the compressor stall point and stall total pressure ratio for the NASA Rotor 35 and Rotor 37 axial compressor cases. Herein, this model was investigated and compared to the results for other models. Later investigations with the model by Menter showed that it could not consistently improve results across a larger number of cases and therefore it was decided to not recommend it for industrial use.

The modification is achieved through an additional production term in the k-equation,

$$P_{reattach} = \tilde{P}_k min\left[4.0max\left(0, \frac{min(S^2, \Omega^2)}{0.09\omega^2} - 1.5\right), 1.5\right] \quad (3.48)$$

The modification only becomes engaged in regions where there is high shear relative to ω and, thus, affects regions strongly out of equilibrium. Not much consideration has been given to these regions in turbulence model calibration. Although the model has not ultimately been recommended for industrial use, the goals behind its creation are still topics for RANS modeling that need to be addressed.

3.2.4 Direct closure of the Reynolds stresses

Reynolds stress models do not use the Boussinesq assumption to relate the stresses to an eddy-viscosity. Instead transport equations for each stress component is modeled. The Reynolds stress model used in the present study is discussed below.

3.2.4.1 The RSM-SSG model

The last model investigated is the RSM-SSG model of Speziale *et al.* (1991) wherein the Reynolds stresses themselves are modeled directly without the use of an eddy viscosity. Transport equations for all six Reynolds stresses and one transport equation for the dissipation are used and the terms in each modeled. The RSM-SSG model differs from other Reynolds stress models in its use of a quadratic relation for the important pressure-strain correlation term that appears in the Reynolds averaged equation for the Reynolds stresses. An advantage of Reynolds stress models over two-equation models is that they are able to simulate the anisotropy of the Reynolds stresses due to Coriolis forces in rotating frames of reference such as are found in the impeller. The extra source terms to account for the Coriolis force are included in the CFX solver, ANSYS (2006).

Reynolds stress models are a closure for the Reynolds stress term itself. A modeled transport equation is solved for each component of the Reynolds stress tensor and an additional equation, usually the transport equation for turbulent dissipation, is written to close terms in the Reynolds stress equation. The modeled Reynolds stress equation is given by

$$\begin{aligned}\frac{\partial}{\partial t}(\overline{\rho}\tau_{ij}) + \frac{\partial}{\partial x_k}(\overline{\rho}\tilde{u}_k\tau_{ij}) = &-\overline{\rho}P_{ij} - \overline{\rho}\Pi_{ij} \\ &+ \frac{\partial}{\partial x_k}\left[\left(\mu + \frac{2}{3}c_s\overline{\rho}\frac{k^2}{\epsilon}\right)\frac{\partial \tau_{ij}}{\partial x_k}\right] + \frac{2}{3}\overline{\rho}\delta_{ij}\epsilon\end{aligned} \tag{3.49}$$

with the production term

$$P_{ij} = \tau_{ik}\frac{\partial \tilde{u}_j}{\partial x_k} + \tau_{jk}\frac{\partial \tilde{u}_i}{\partial x_k} \tag{3.50}$$

Since the dissipation is needed to close the Reynolds stress transport equations, a transport equation for the dissipation is also included.

$$\frac{\partial}{\partial t}(\bar{\rho}\epsilon) + \frac{\partial}{\partial x_k}(\bar{\rho}\tilde{u}_k\epsilon) = \frac{\epsilon}{k}(c_{\epsilon 1}P - c_{\epsilon 2}\bar{\rho}\epsilon) + \frac{\partial}{\partial x_k}\left[\left(\mu + \frac{\mu_T}{\sigma_\epsilon}\right)\frac{\partial \epsilon}{\partial x_k}\right] \tag{3.51}$$

The pressure-strain correlations are expressed as

$$\Pi_{ij} = \Pi_{ij1} + \Pi_{ij2} \tag{3.52}$$

where

$$\Pi_{ij1} = -\epsilon\left[C_{s1}a_{ij} + C_{s2}\left(a_{ik}a_{kj} - \frac{1}{3}a_{mn}a_{mn}\delta_{ij}\right)\right] \tag{3.53}$$

$$\begin{aligned} \Pi_{ij2} = & - C_{r1}Pa_{ij} + C_{r2}\bar{\rho}kS_{ij} - C_{r3}\bar{\rho}kS_{ij}\sqrt{a_{ij}a_{ij}} \\ & + C_{r4}\bar{\rho}k\left(a_{ik}S_{jk} + a_{jk}S_{ik} - \frac{2}{3}a_{mn}S_{mn}\delta_{ij}\right) \\ & + C_{r5}\bar{\rho}k\left(a_{ik}\Omega_{jk} + a_{jk}\Omega_{ik}\right) \end{aligned} \tag{3.54}$$

The anisotropy tensor, the mean strain rate tensor, and the mean vorticity tensor are defined as

$$a_{ij} = \frac{\tau_{ij}}{k} - \frac{2}{3}\delta_{ij} \tag{3.55}$$

$$S_{ij} = \frac{1}{2}\left(\frac{\partial \tilde{u}_i}{\partial x_j} + \frac{\partial \tilde{u}_j}{\partial x_i}\right) \tag{3.56}$$

$$\Omega_{ij} = \frac{1}{2}\left(\frac{\partial \tilde{u}_i}{\partial x_j} - \frac{\partial \tilde{u}_j}{\partial x_i}\right) \tag{3.57}$$

The closure coefficients for the Speziale *et al.* (1991) model are

$$\begin{array}{llll} C_\mu = 0.1 & \sigma_\epsilon = 1.36 & c_s = 0.22 & c_{\epsilon 1} = 1.45 \\ c_{\epsilon 2} = 1.83 & C_{s1} = 1.7 & C_{s2} = -1.05 & C_{r1} = 0.9 \\ C_{r2} = 0.8 & C_{r3} = 0.65 & C_{r4} = 0.625 & C_{r5} = 0.2 \end{array}$$

3.3 Summary

The time averaged governing equations for a turbulent compressible flow have been outlined above, and the turbulence models for the current study have been presented. The discussion in the following chapter will describe particulars of the numerics that are specific to the study undertaken herein.

Chapter 4

Discussion of numerics for the study

4.1 Solver

The commercial CFD code, ANSYS CFX-11.0 was used to carry out the simulations. The finite-volume method is used for the spatial discretization of the governing equations with volumes centered on vertices. The solver allows the use of hexahedral, tetrahedral, and prismatic elements, and grids are treated in an unstructured manner. The scheme used within the solver is conservative, implicit and second order in its spatial and temporal discretization. It uses the pressure-based coupled algebraic multi-grid method of Raw (1996), with the discrete equations evaluated using a second order advection scheme similar to that presented in Barth and Jesperson (1989), and evaluates mass flow using the pressure-velocity coupling algorithm of Rhie and Chow (1983).

4.2 The mixing plane approach

The main interest in the present study is the time averaged flow field. Mixing plane analysis is used where any true dependence of the flow field on the relative position of the blades and diffuser pipes is mixed out circumferentially, while the spanwise variations found at the impeller exit are retained, as Dawes (1995) stressed was much more significant in obtaining the proper physics in the compressor stage. The interaction effects between the rotor and stator are thus the time averaged interaction rather than the unsteady interaction. The flow field is computed for a single impeller passage and single diffuser passage (Fig. 2.4) with periodic boundary conditions that bound the domain from hub to shroud and the mixing plane is implemented at the interface of the impeller and diffuser domains to couple the rotating impeller flow field with the stationary diffuser flow field.

The use of a mixing plane means that a steady state solution is sought where the field variables are computed in a rotating reference frame in the impeller section and a stationary frame in the diffuser section. This is implemented by applying circumferential averages to fluxes through bands on the mixing plane. The spanwise profiles thus obtained from the exit plane of the rotating impeller domain are used on the inlet of the stationary diffuser domain. Over the course of the iteration process, the profile that constitutes the appropriate steady state interaction between the two components is sought. The interface fluxes across the mixing plane are implemented within the solver such that they are fully implicit and strict conservation is maintained across the interface for mass, momentum, and energy after changes in pitch are accounted for (ANSYS, 2006).

The pressure profile at the mixing plane is determined by extrapolation of the profile on each side of the plane. Since this can sometimes be unstable, a small amount of stiffness is added by decaying the profile towards a constant value by 5%.

4.3 Boundary conditions

To solve the governing equations, boundary conditions must be specified. Different points along the compressor stage speedline (characteristic curve) require different exit boundary conditions to be specified. A given static pressure is imposed for points along the speedline with relatively high inlet corrected mass flow rates for the stage. The boundary condition is changed to a specified mass flow rate for lower inlet corrected mass flow rates. For either case, a constant diffuser exit static pressure profile is enforced. The reason for switching between pressure and mass flow boundary conditions is that at a certain maximum mass flow rate, the flow will be choked at the diffuser throat. When this happens, the mass flow rate is essentially constant and the only stable boundary condition would be one where the back pressure is imposed. However, for lower mass flow rates as the compressor approaches stall, the compressor may run at mass flow rates below peak static pressure rise. Thus, for a stable solution, a mass flow must be specified, as the imposed exit pressure cannot exceed the maximum achievable pressure rise of the machine.

At the impeller inlet, axi-symmetric spanwise profiles of total pressure, total temperature, and flow direction are specified across the plane where all profiles were obtained from pitot and cobra pressure probe traverses carried out previously in the Pratt & Whitney Canada compressor rig in Longueuil, Quebec. The profiles of the total temperature and total pressure normalized by their respective mass flow averaged values are shown in Fig. 4.1, plotted against the normalized span height, ζ, where the coordinate is defined such that $\zeta = 0$ at the hub wall and $\zeta = 1$ at the shroud wall as described in Chapter 2. The profiles of the absolute reference frame flow angle in the circumferential direction relative to the machine axis, α, and the meridional plane (radial-axial plane) flow angle, ϕ, are shown in Fig. 4.2. The profile for the meridional flow angle, ϕ, is simply a linear interpolation from the hub and shroud meridional plane angles. All wall boundary conditions are modeled as no-slip and adiabatic. A small bleed mass flow is extracted downstream of the impeller trailing edge to extract a similar amount of mass flow as would be the case in the actual engine.

The impeller Reynolds number based on tip speed and impeller exit passage height for the 100% speed characteristic curve analyzed is approximately 331,600 where the Reynolds number is defined as

$$Re = \frac{U_2 b_2}{\nu} \tag{4.1}$$

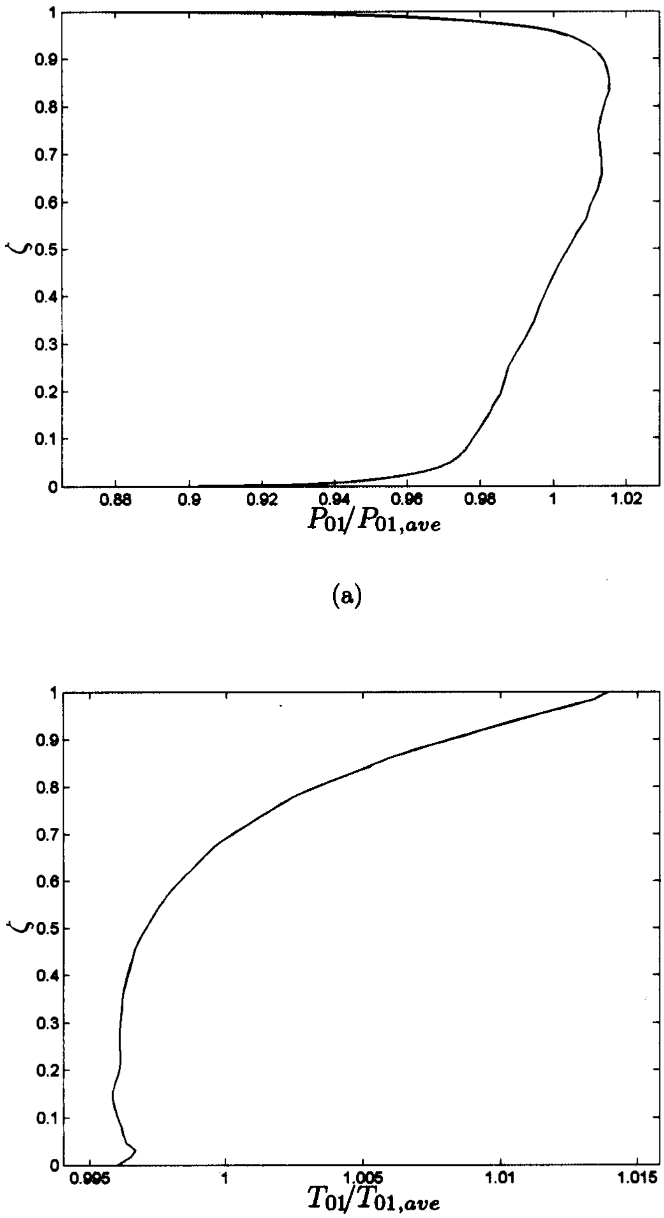

(a)

(b)

Figure 4.1: Inlet boundary condition profiles normalized by mass flow averaged values for (a) total pressure and (b) total temperature.

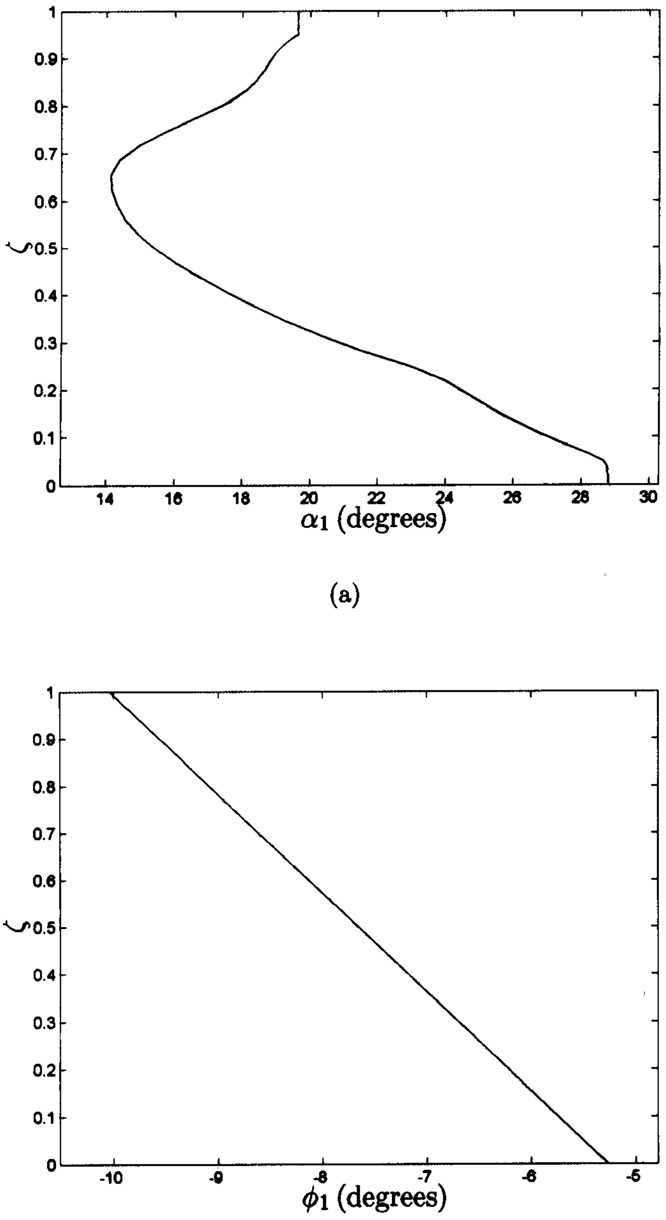

(a)

(b)

Figure 4.2: Inlet boundary condition profiles for flow direction for (a) α and (b) ϕ.

4.4 Computational grid

The inducer, the exducer, and the diffuser are all gridded separately using ANSYS ICEM CFD and are joined with domain interfaces within the solver which allow non-matching grids. A hybrid grid consisting of tetrahedral and prism layers along the wall is used for the diffuser section and hexahedral grids are used for the two impeller sections (inducer and exducer). The grid used herein has approximately 2.7 million nodes (2.7M) in total. In particular, there are approximately 780k nodes in the inducer section, 1.1M in the exducer section, and 820k in the diffuser section. The impeller grids used 25 nodes in the tip region for resolution of the tip clearance flow. The grids herein are somewhat more dense than many other numerical studies of centrifugal stages where approximately 1M nodes are used in total. The increased grid density stems from the use of a turbulence model that integrates through the sublayer as well as the resolution of the tip clearance flow. A global view of the grid is shown in Fig. 4.3. Some more detailed views of different portions of the grid are shown in Figs. 4.4 and 4.5.

The standard computational grid used in nearly all simulations herein approximates the fillet surfaces that join the blade and hub surfaces. The approximation involves a modeled fillet surface that has a sharp discontinuous interface between the blade and the hub, but accounts for the majority of the geometrical blockage associated with the fillet while degenerate mesh angles (mesh angles that approach zero degrees), which would occur with the true fillet representation in the complicated tandem blade geometry of the studied impeller, are avoided. The angle between the surfaces used is 45 degrees. More discussion concerning this fillet representation is given in the beginning of Chapter 7.

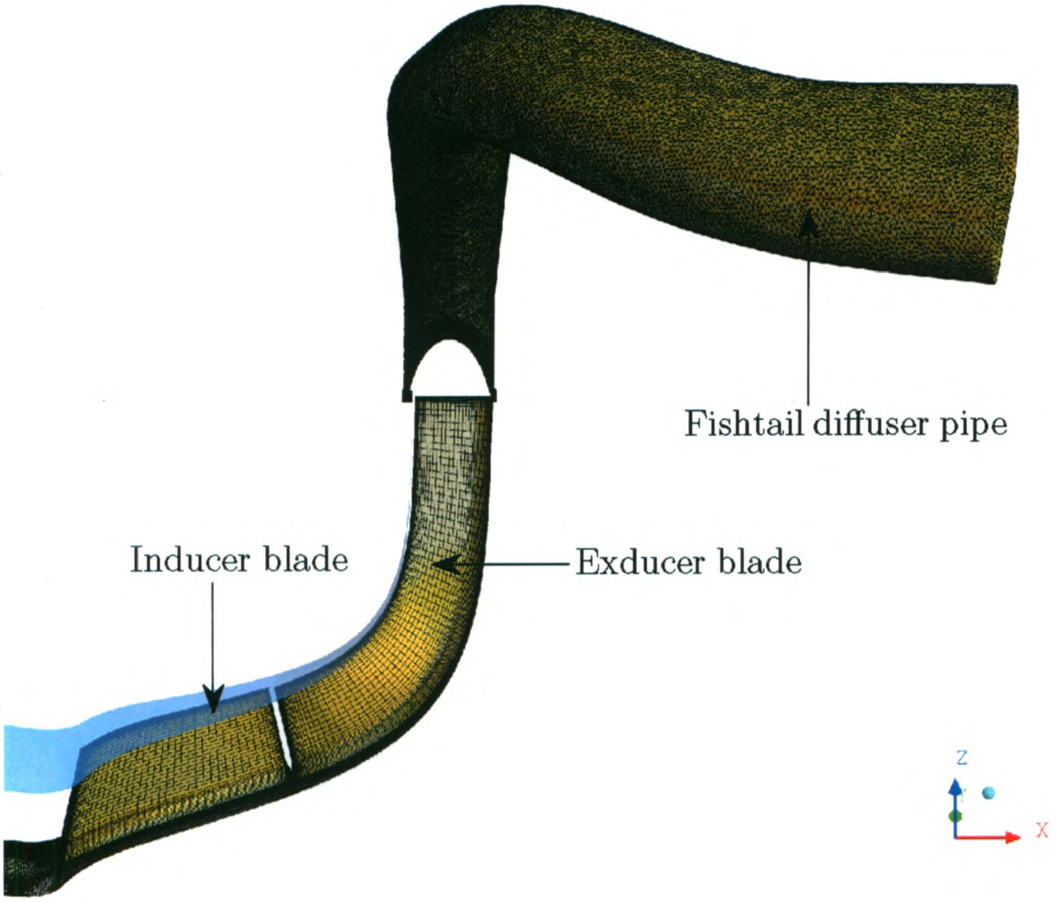

Figure 4.3: Computational grid for the blade, hub, and diffuser wall surfaces.

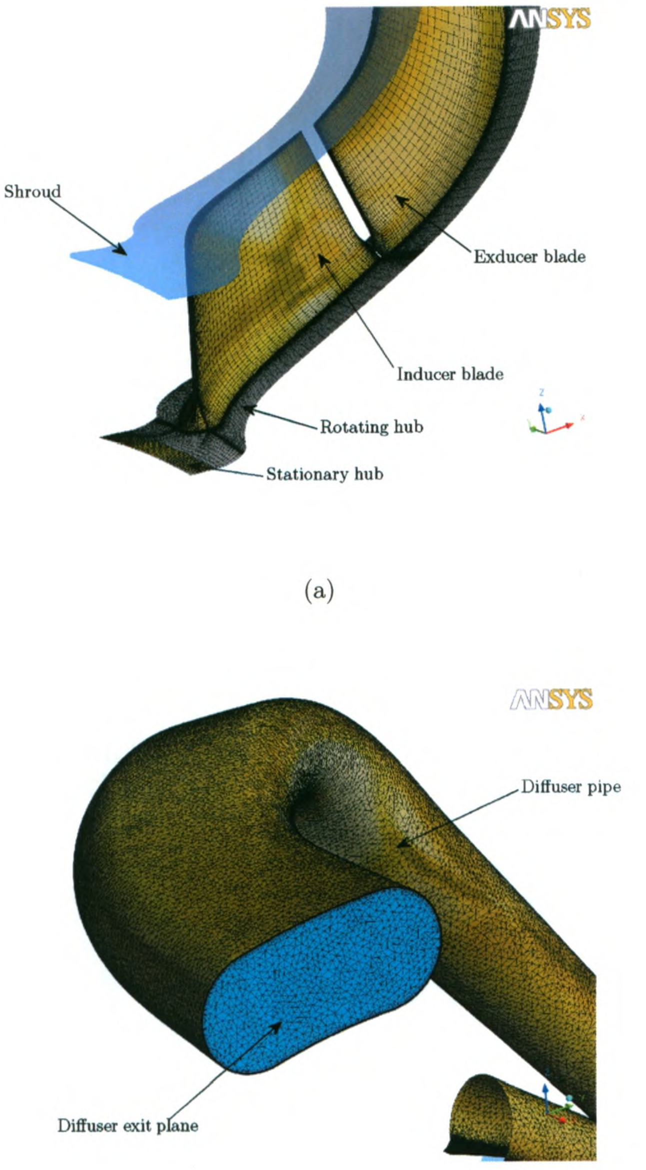

(a)

(b)

Figure 4.4: Grid details of (a) impeller blades and (b) diffuser pipe.

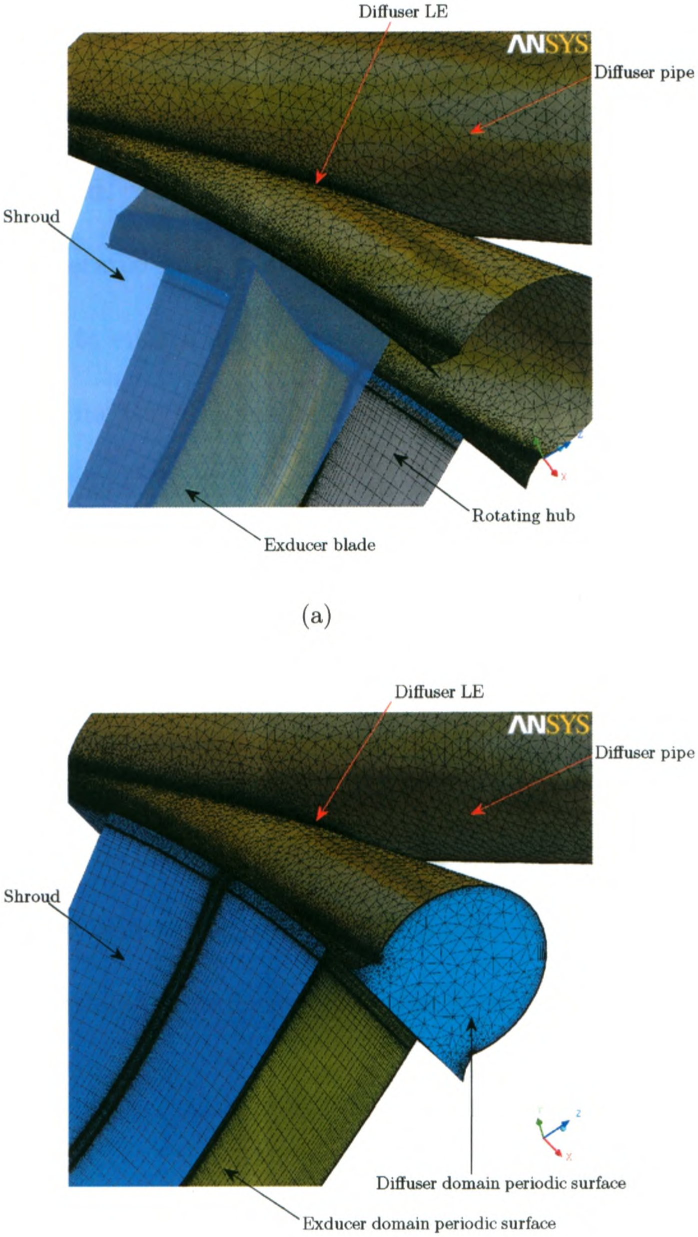

(a)

(b)

Figure 4.5: Grid details of (a) the impeller-diffuser interface and (b) the periodic and shroud surfaces.

4.5 Near-wall treatment

It should be emphasized that the near-wall treatment is different depending on which turbulence model is used. The same grid is used for all turbulence models where the grid has been generated such that average y^+ values at the walls are in the range of about 0.5-1.5 to ensure good resolution into the viscous sublayer. This is particularly important for the SST model since the near wall modeling is based on the ω-formulation of Wilcox (1998) which provides good results through the viscous sublayer. The CFX automatic near-wall treatment is used for the SST model which will automatically switch over to a wall-function approach if the closest grid point off the wall is outside of the viscous sublayer. The CFX scalable wall functions allow the use of the same grid for the other two models which are based on an ϵ-formulation. This formulation cannot be used through the viscous sublayer (Wilcox, 2006) so wall functions are necessary, and the scalable wall functions in CFX limit the distance scale used in the logarithmic formulation such that it will always reside outside the viscous sublayer (ANSYS, 2006).

4.6 Summary

The specific details of the numerics for the present study have been presented in this chapter. The discussion described the solver, the mixing plane approach used for coupling rotating and stationary components, the boundary conditions, the computational grid, and the near-wall treatment for the turbulence models. The discussion will now turn to the numerical results, starting first with a discussion in the following chapter of a grid independence study performed.

Chapter 5

Grid independence study

This chapter begins the presentation of numerical results. Throughout the discussion, some data have been normalized, or otherwise modified by certain reference values, to protect the proprietary information of Pratt & Whitney Canada.

5.1 Assessment of grid convergence

The first task is to analyze the level of grid convergence of the simulations presented. Three sets of grids were generated for each component (inducer, exducer, and diffuser), and the node counts are shown in Table 5.1.

The hexahedral impeller grids were refined by approximately doubling the node count for each refinement level. This means in each of the three dimensions, on

Table 5.1: Grid node comparison

Domain	Coarse Grid	Medium Grid	Fine Grid
Inducer	401,858	776,371	1,405,598
Exducer	638,850	1,101,974	2,084,525
Diffuser	947,978	823,053	2,016,145

average, cell edge lengths are reduced by a factor of $2^{1/3}$. The diffuser grids were generated in the same way, by reducing the edge seed length sizes by the same amount. The medium refinement level was generated with the ANSYS ICEM CFD 10.0 multi-purpose grid generation software, while the other two levels were generated with the newer version ICEM CFD 11.0. Due apparently to differences in the grid generation algorithm, despite the fact that the seed length sizes were scaled appropriately, the coarse grid has more nodes than the medium grid. Inspection of the grids seems to indicate that more dense regions of the grid, in particular the leading edge region (which accounts for a large portion of the node count), seem to be most at fault for this fact, and it is only these very localized regions with small edge lengths that cause this inconsistency in node counts. In the new generator, more elements are placed locally in these areas. It was decided that rather than regenerating the medium level grid, the apparently more efficiently generated grid (in the sense that a smaller number of nodes was obtained with the same desired seed lengths throughout the different regions when using the older version of the grid generator) would be used. The dense grid regions at the diffuser leading edges account for so little of the physical domain that between the coarse and medium grids the intention of the grid independence study still holds: the size of the control volumes are being reduced in the different regions of the grid upon each refinement level. The discretisation of the governing equations approaches, in the limit, the case of infinitesimal volumes which reproduce the conservation equations exactly. As the sizes of the discrete volumes are reduced, errors due to the finite size of the control volumes should also approach zero. At each subsequent refinement level, generally the local sizes of volumes are reduced, so these tendencies should still hold except in some very small localized regions.

Cases were run on each grid for the SST turbulence model at the design rotational speed and approximately the same design net exit corrected flow rate, $\dot{m}_{c,4}$ (the differences for each grid simulation for this parameter are all below 0.1%). The net exit corrected design flow rate is given by the peak efficiency at the design rotational speed. It is given by

$$\dot{m}_{c,4} = \dot{m}_4 \frac{\sqrt{T_{04}/T_{ref}}}{p_4/p_{ref}} \tag{5.1}$$

The reference values to which the massflow is corrected are to standard temperature, 288.15K, and pressure, 101.325kPa. A comparison of a number of bulk parameters obtained for each grid refinement level is given in Table 5.2.

Table 5.2: Comparison of parameters for the three grid refinement levels.

Variable	$\frac{\phi_{Coarse}-\phi_{Med}}{\phi_{Fine}}(\%)$	$\frac{\phi_{Coarse}-\phi_{Fine}}{\phi_{Fine}}(\%)$	$\frac{\phi_{Med}-\phi_{Fine}}{\phi_{Fine}}(\%)$
$\dot{m}_{c,1}$	0.35	-0.76	-1.11
$\dot{m}_{c,4}$	0.01	-0.07	-0.07
$\Pi_{02,01}$	-0.36	0.09	0.46
$\Pi_{4,01}$	0.24	-0.66	-0.91
$TR_{02,01}$	-0.10	0.03	0.13
$TR_{04,01}$	-0.09	0.03	0.12
$\eta_{01,02}$	-0.05	-0.005	0.04
$\eta_{01,4}$	0.67	-0.99	-1.66

The inlet corrected flow rate, $\dot{m}_{c,1}$, shows a discrepancy of up to about 1.1%. This is the inlet mass flow rate where again a correction is given to standard temperature and pressure, but here using the total pressure value (the reason for the total pressure being used at the inlet and static pressure at exit is analogous for the reason why the stage efficiency is usually defined in terms of the difference of static enthalpy at the exit to the total enthalpy at inlet – the static pressure at exit gives an indication of the amount of pressure rise through the diffuser, and thus indicates the amount of energy converted from kinetic energy at the exit of the impeller to potential energy through the diffuser),

$$\dot{m}_{c,1} = \dot{m}_1 \frac{\sqrt{T_{01}/T_{ref}}}{p_{01}/p_{ref}} \tag{5.2}$$

This is the highest variation seen in any parameter other than the stage total to static efficiency, $\eta_{01,4}$, given by the ratio of the isentropic enthalpy rise and the actual enthalpy rise throughout the compressor stage,

$$\eta_{01,4} = \frac{h_{4,isen} - h_{01}}{h_{04} - h_{01}} \tag{5.3}$$

which was seen to be different by less than 1.7% for all refinement levels.

Other variations presented are the impeller total to total pressure ratio, $\Pi_{02,01}$, temperature ratio, $TR_{02,01}$, and isentropic efficiency, $\eta_{01,02}$, as well as the stage total to static pressure ratio, $\Pi_{4,01}$, and total to total temperature ratio, $TR_{04,01}$, all of which are less than 1%. These are defined as

$$\Pi_{02,01} = \frac{p_{02}}{p_{01}} \tag{5.4}$$

$$TR_{02,01} = \frac{T_{02}}{T_{01}} \tag{5.5}$$

$$\eta_{01,02} = \frac{h_{02,isen} - h_{01}}{h_{02} - h_{01}} \tag{5.6}$$

$$\Pi_{4,01} = \frac{p_4}{p_{01}} \tag{5.7}$$

$$TR_{04,01} = \frac{T_{04}}{T_{01}} \tag{5.8}$$

As an illustrative example of the differences in extracted flow field data at the three grid refinement levels, a number of spanwise profiles, with their geometrical locations shown in Fig. 5.1, are compared in Fig. 5.2. The meridional and circumferential velocity profiles, normalized by the blade tip velocity, for four streamwise locations, ξ, are plotted against their spanwise location, ζ within the impeller. By the definition of the impeller coordinate system, $\xi = [0, 1]$ is within the inducer section and $\xi = [1, 2]$ is within the exducer section (see section 2.1). Likewise, $\zeta = 0$ is by definition the hub surface, $\zeta = 1$ is the shroud surface. The profiles shown are defined by the itersection of a constant streamwise cut and one of the periodic surfaces bounding the computational domain, rotated 2.90 degrees around the machine axis into the computational domain. The locations themselves are not overly important, they are just a sample comparison of results on the different grids. It is seen that some discrepencies between grids grow with streamwise position, but the discrepencies are only of the order of 2% of the tip speed, U_2.

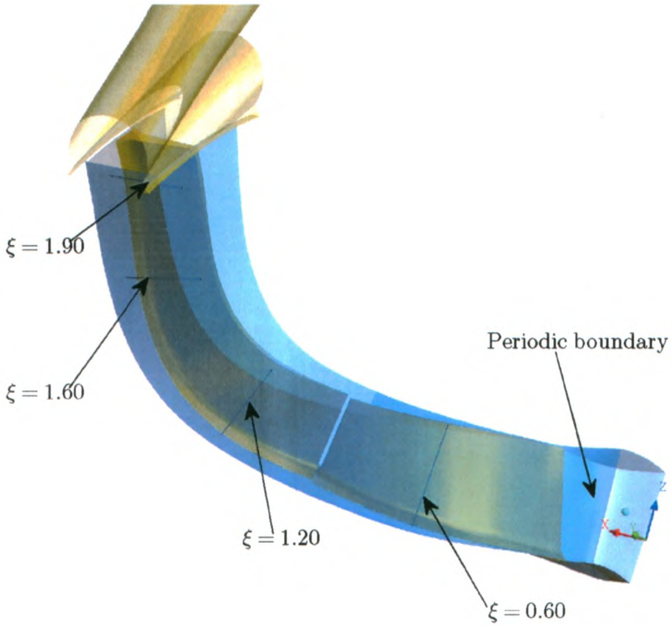

Figure 5.1: Geometrical locations of extracted profile locations in Fig. 5.2 which are taken 2.90 degrees circumferentially off the periodic surface.

The differences in parameters shown in Table 5.2 are considered to be sufficiently low for the purposes of the present study considering they are on the order of the experimental uncertainties involved in the performance parameters being used to verify the results. The order of variability in the parameters are also on the order of the maximum domain imbalances of the conserved quantities (mass, momentum, and energy) deemed acceptable for a converged run, defined as 0.1%, and this is likely the reason that the parameters do not seem to converge with grid refinement level (differences are not necessarily smallest when comparing the medium and fine grids).

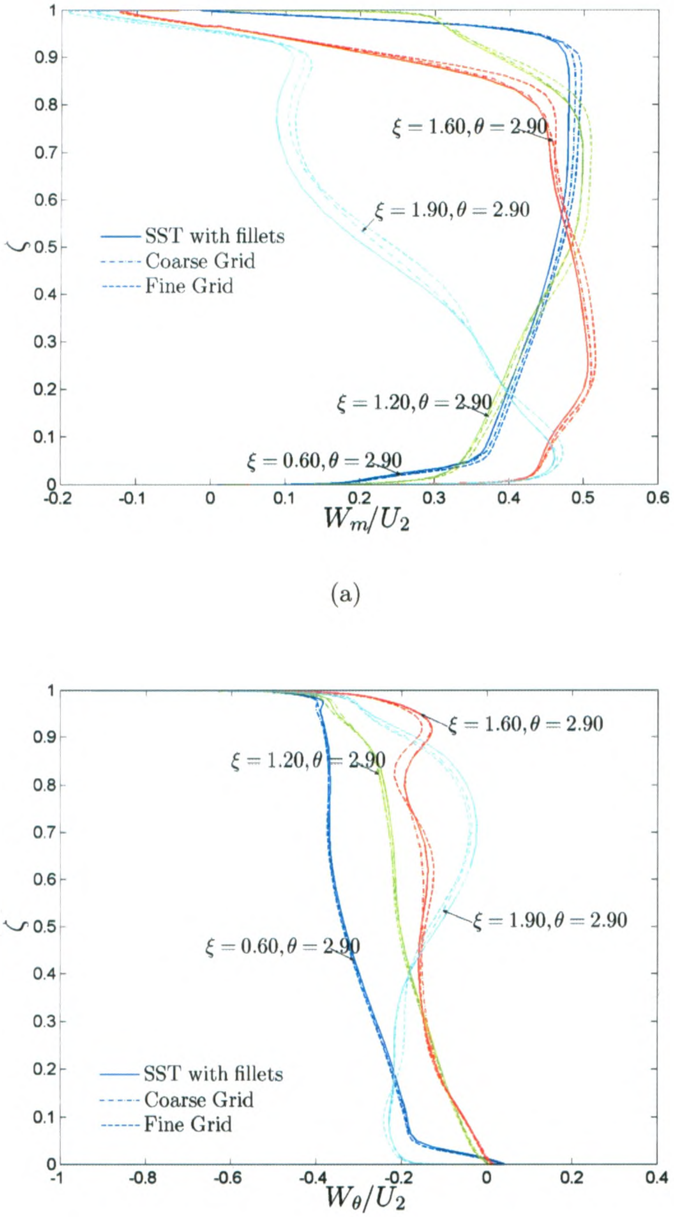

Figure 5.2: Comparison of (a) meridional and (b) circumferential velocity at 4 streamwise locations, ξ, along the impeller. Variables are extracted 2.90 degrees circumferentially off the periodic surface.

5.2 Summary

A presentation of results from a grid independence study were given with a quantification of differences in performance parameters important for the study on the three grid refinement levels. The next chapter discusses the baseline simulations for this work. The baseline simulations use the medium refinement level grid with an approximated fillet geometry. They incorporate the impeller and diffuser components, but no downstream exit plenum, and the SST turbulence model is employed for closure of the mean flow conservation equations.

Chapter 6

Results of baseline simulations

Recent design experience at Pratt & Whitney Canada has shown that quite accurate predictions of measured performance parameters in centrifugal compressor stages are possible using a full stage simulation with a mixing plane and the SST turbulence model (Roberts and Steed, 2004). This is especially true when comparing this coupled type of impeller and diffuser simulation to previous design methodology where components are analyzed in isolation from each other. In this case, the boundary conditions, particularly on the impeller exit, are not well-defined as the interaction between the components is unknown beforehand and the influence of the diffuser on the flow field is not actually being found from the solution procedure. The downstream side of the impeller is being defined by the boundary conditions implemented which cannot properly reflect the influence of the diffuser on the flow field unless it is known beforehand.

The actual coupling of the flow field by use of a mixing plane is a quite simple representation of a highly complex flow field involving rotating blade wakes and pressure fields that change locally with the relative orientations of the rotor and stator. For a designer, it is important that the flow field calculated is giving proper performance predictions because the numerical solutions are predicting physically meaningful representations of the flow field. Ultimately, it is desired to validate velocity profiles at the mixing plane against experiments. At the time of submission of this thesis, only measurements at the inlet and exit of the stage are available as well as a single spanwise traverse at the impeller-diffuser interface. Further data collection is being undertaken at the impeller-diffuser interface to extract spanwise velocity profiles that span a full diffuser pitch and measurements will be taken both phase-locked with the rotation of the shaft and unsynchronized as is modeled with a mixing plane. Performance measurements have been available along the 100% shaft speedline from a previous measurement campaign by P&WC and will be used as validation, and a discussion of the recent LDV measurements will be deferred until Chapter 9.

This chapter presents the flow field and performance predicted for the baseline case for the simulations. Studies in the following chapters will be compared against this baseline. The stage is modeled with impeller and diffuser components, with the exit boundary located at the diffuser exit plane. The impeller fillets are approximated and the SST turbulence model is applied. The success and robustness seen with the SST model and the specific geometric model (with approximated fillets and without an exit plenum) for predicting the performance parameters in the compressor stage have meant that more points along the speedline have been computed for this case compared to the other investigated cases.

6.1 Performance predictions over the compressor speedline

Performance parameters from the computations are compared to those found experimentally for the compressor stage along the speedline which corresponds to the design (100%) shaft speed of the stage. Experimental data have been provided courtesy of Douglas Roberts of Pratt & Whitney Canada. Performance parameters are determined using the instrumentation shown for the compressor test rig presented in Fig. 6.1. Total pressure and temperature measurements are taken at the intake of the rig at eight circumferential locations. Impeller entry total pressure is determined from the intake measurements with a calibration of the intake in a blow-down test rig. An ASME nozzle upstream of the test section is used to measure the mass flow rate and static pressure measurements are taken at the hub and shroud of the impeller trailing edge, the diffuser throat, and above the diffuser exit in the plenum chamber. The average of four measurements is taken at each location. The plenum static pressure measurement location is used as the stage exit pressure since it has been seen in CFD analysis of the rig to differ in pressure from the pressure at the diffuser exit plane by only 0.1%, and has been verified experimentally by P&WC. A calibrated orifice-plate is used to measure the back-face bleed flow rate extracted at the trailing edge hub. Finally, the diffuser exit total temperature is measured using eleven covered thermocouples just inside the exit of the diffuser pipe exits, each at a different location to obtain an average temperature over the exit plane. Elemental uncertainties on single sample temperature measurements have been stated as ±1 deg F and uncertainties for the static pressure measurements have been given as ±0.006 psi at the impeller inlet, ±0.009 psi at the impeller trailing edge, and ±0.02 psi at the plenum downstream of the diffuser exit. Uncertainties have been estimated for pressure and temperature ratios by taking the single sample elemental uncertainties and the precision error estimated from calculating mean temperature and pressure values from 50 single sample measurements and using a root sum of squares to obtain a total uncertainty. Estimated uncertainties found are ±0.5% for temperature ratios and ±1% for pressure ratios. Uncertainties in mass flow rate measurements have been stated as ±1%.

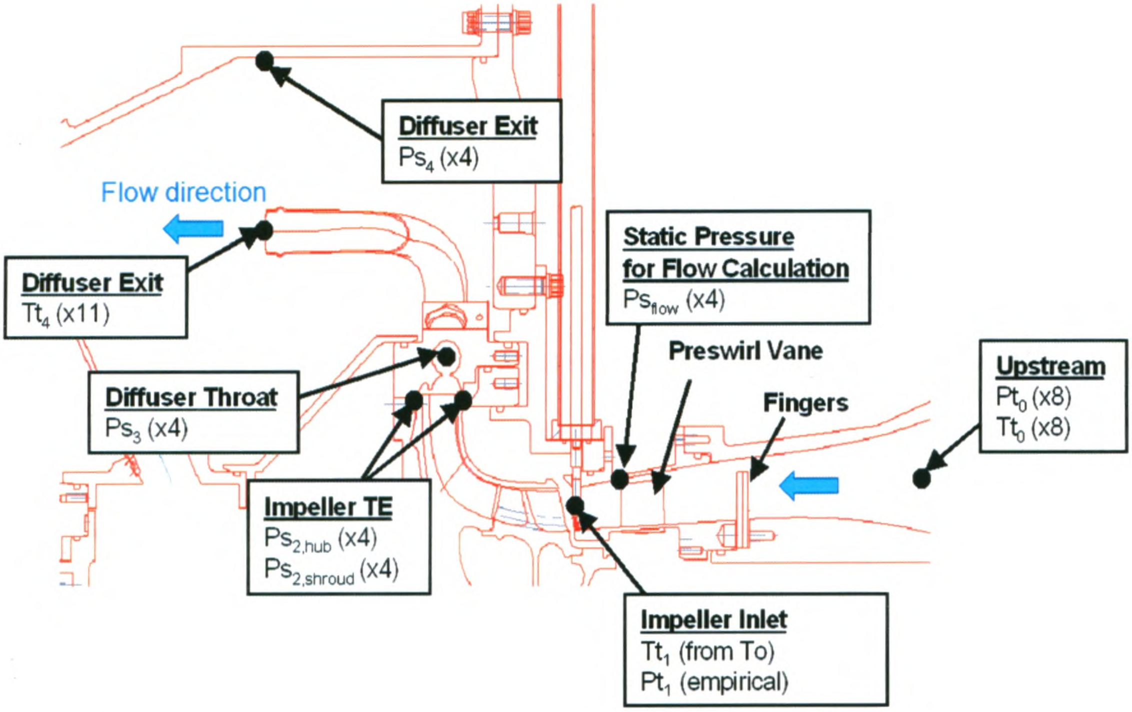

Figure 6.1: Pressure and temperature measurement locations in compressor test rig. Courtesy of Douglas Roberts (Roberts and Steed, 2004)

The stage total to static pressure ratio along the compressor characteristic mapped at 100% shaft speed is shown in Fig. 6.2. The choking of the compressor stage, shown by the vertical portion of the speedline, is governed by the diffuser throat area. The choke mass flow rate is over-predicted in the case of the SST model by about 1%, which is deemed acceptable since the estimated uncertainty of the mass flow measurement itself is about 1%.

A particularly important parameter for performance predictions is the total to total temperature ratio as it is a measure of the work done on the fluid by the compressor. It is clearly seen in Fig. 6.3 that the experimental drop-off of the temperature ratio with inlet corrected mass has a slightly higher rate just before the onset of choke with the SST model. The maximum difference, however, between the experimental and numerical predictions are within half a percent which is within the experimental uncertainty of the totat to total temperature ratio which has been estimated at 0.5%. Once the diffuser is choked, the total temperature rise in the stage is constant because the work done on the fluid is a function of the mass flow rate which is being limited by the diffuser throat. When plotted against inlet corrected flow rate in Fig. 6.3(a), all points lie on top of each other when the compressor is choked, and when plotted against net exit corrected flow in Fig. 6.3(b), all points lie along a line of constant $TR_{04,01}$. The net exit corrected flow is not constant since it is a function of exit pressure which is still reducing along the speedline as the stage is put into deeper and deeper choke. It is not fully understood why the experimental rig data show a drop-off in the total temperature ratio when the stage is choked.

The same trend was seen in the performance data from a similar compressor stage in the same compressor rig in Roberts and Steed (2004). The impeller is designed with a higher choke flow margin than the diffuser, so the impeller itself should not be choked here (and it is not in the numerical simulations). Perhaps certain physics which occur in reality are not being captured by the mixing plane at the choke side of the speedline. Perhaps bow waves extend from the diffuser leading edge which interact with the impeller flow field which may affect the impeller slip, and with it, the total temperature rise through the stage. Such effects could never be seen on the upstream side of a mixing plane.

Fig. 6.4 shows the change in stage total to static efficiency from a reference condition, again plotted against the inlet corrected and net exit corrected flow rates. The baseline model (the SST model) shows good agreement with the experimental data near the design flow rate and shows an under-prediction as the choke flow is approached.

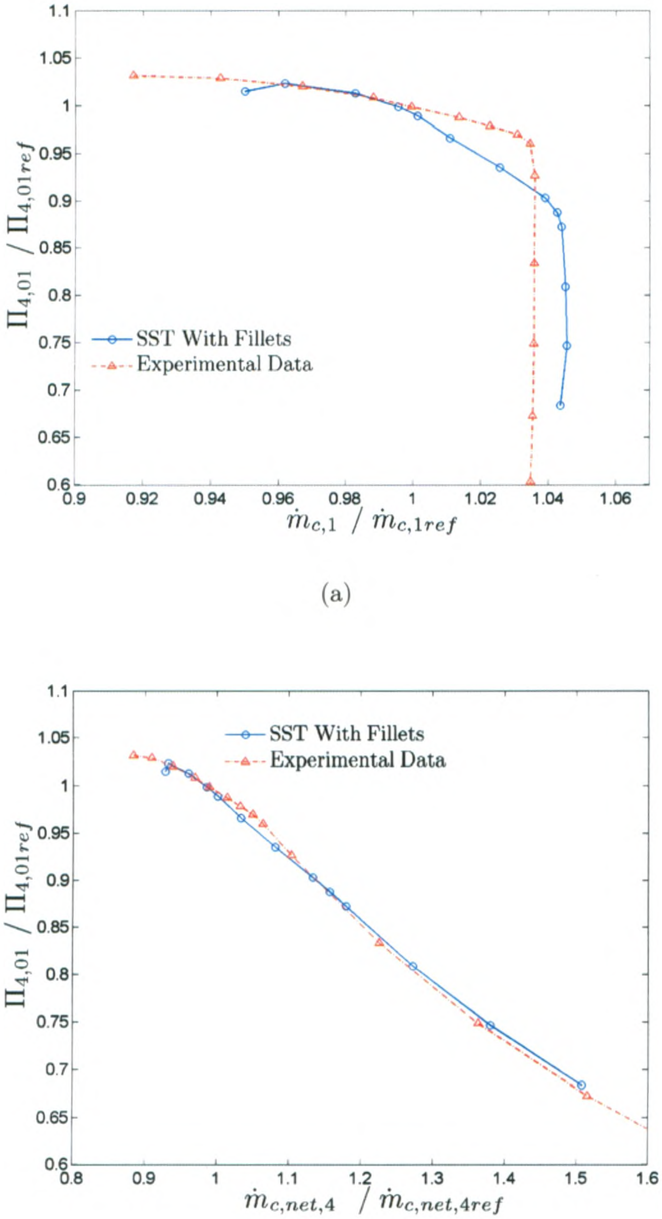

(a)

(b)

Figure 6.2: Normalized pressure ratio versus (a) inlet corrected flow rate and (b) net exit corrected flow rate.

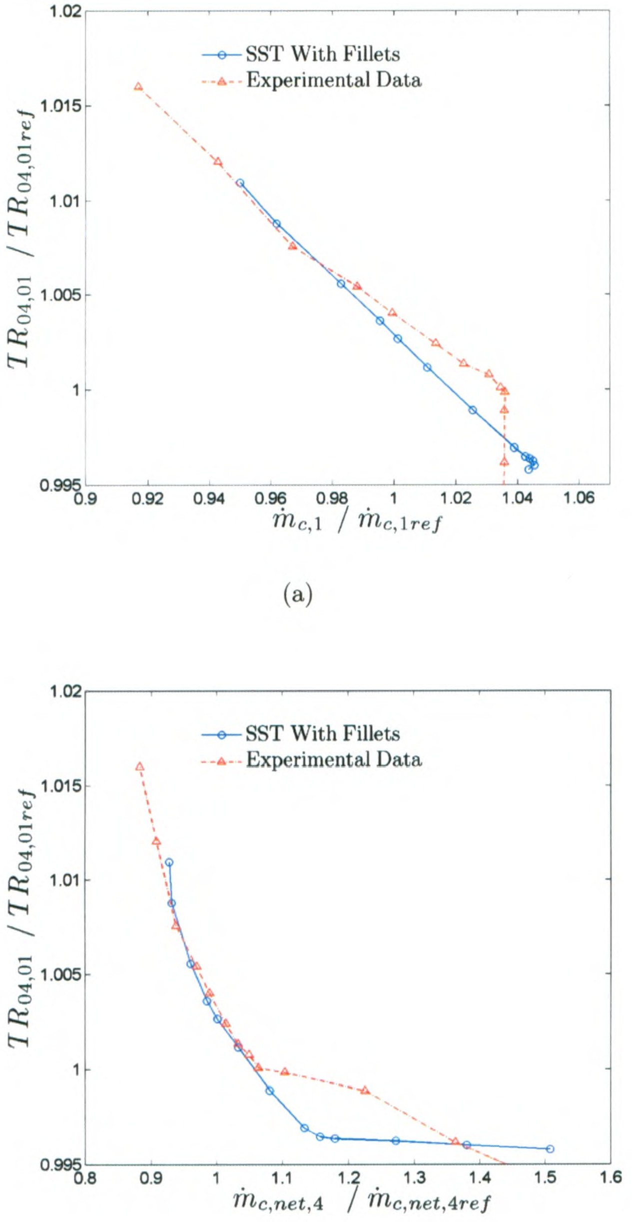

(a)

(b)

Figure 6.3: Normalized total temperature ratio versus (a) inlet corrected flow rate and (b) net exit corrected flow rate.

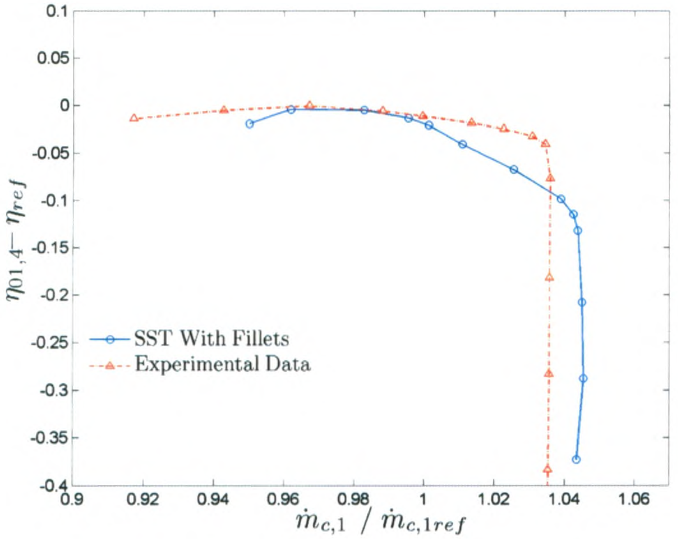

(a)

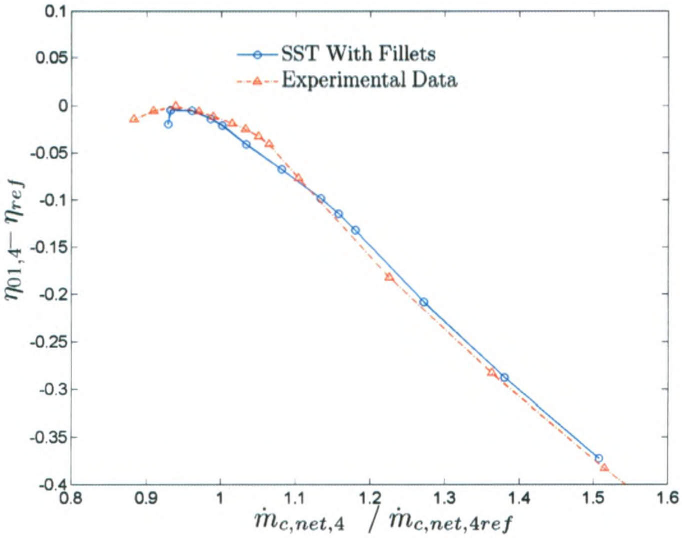

(b)

Figure 6.4: Efficiency change versus (a) inlet corrected flow rate and (b) net exit corrected flow rate.

6.2 Flow field at the design flow rate

In this section the results obtained with the SST model at the design net exit corrected flow rate are discussed. First, spanwise cuts through three blade passages are presented in the blade-to-blade view (i.e. the meridional-circumferential plane) at 50% span, $\zeta = 0.5$, and 95% span, $\zeta = 0.95$ in Figs. 6.6 and 6.7, respectively. To highlight the physical orientation of these surfaces, the Cartesian view of these cuts is shown in Fig. 6.5, showing the surface of constant span throughout the impeller.

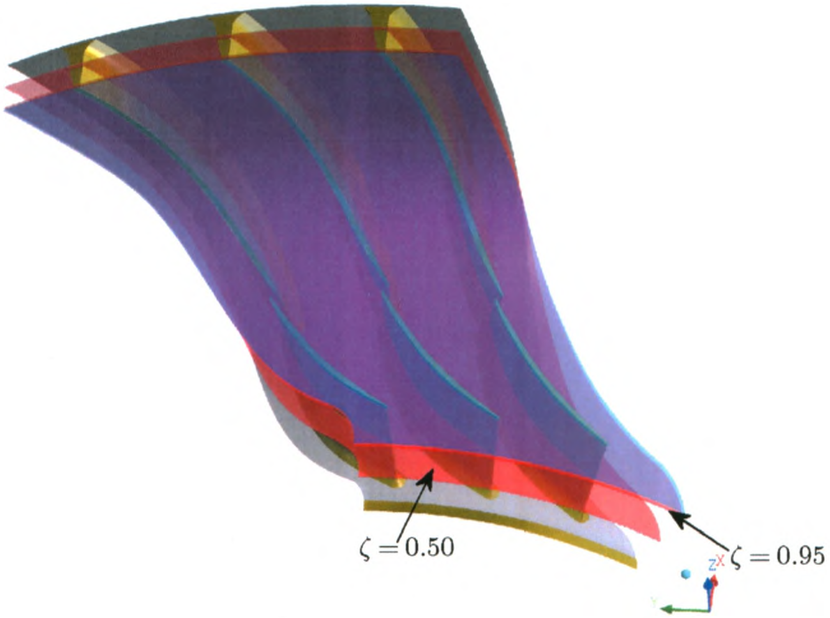

Figure 6.5: Cartesian view of the constant spanwise surfaces shown in Figs. 8.4 and 8.5.

The relative frame Mach number field for the 50% spanwise cut in Fig. 6.6 shows that at the inducer inlet, the flow along the blade suction surface (the trailing surface of the blade as it rotates, seen as the top surface of the blades in the figures) shows an acceleration as the flow gains momentum from the spinning impeller. At the exit, a low momentum flow region is seen. This is the footprint of the highly distorted tip clearance flow which arises due to the shear in the small gap at the tip of the blades between the stationary shroud and the rotating blade. The width of this gap has a very significant effect on the performance parameters of a compressor stage.

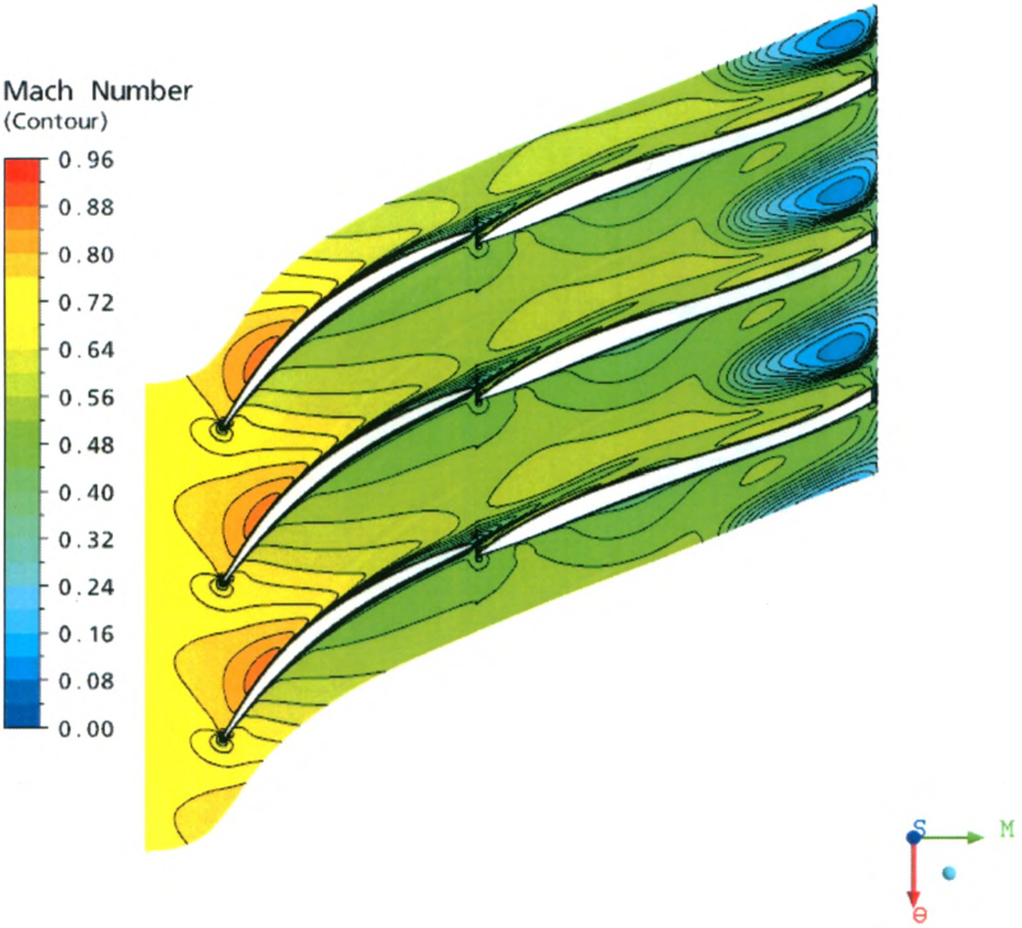

Figure 6.6: Blade-to-blade relative Mach number contours at 50% span.

Fig. 6.7 shows a similar blade-to-blade cut as in Fig. 6.6 but at 95% span where the low momentum and highly distorted zone at the exit of the impeller is even more pronounced. The streaky low momentum zone seen in the inducer passage is also due to the tip clearance flow. The higher acceleration seen at the inducer inlet is due to the higher blade velocity at this greater radial distance.

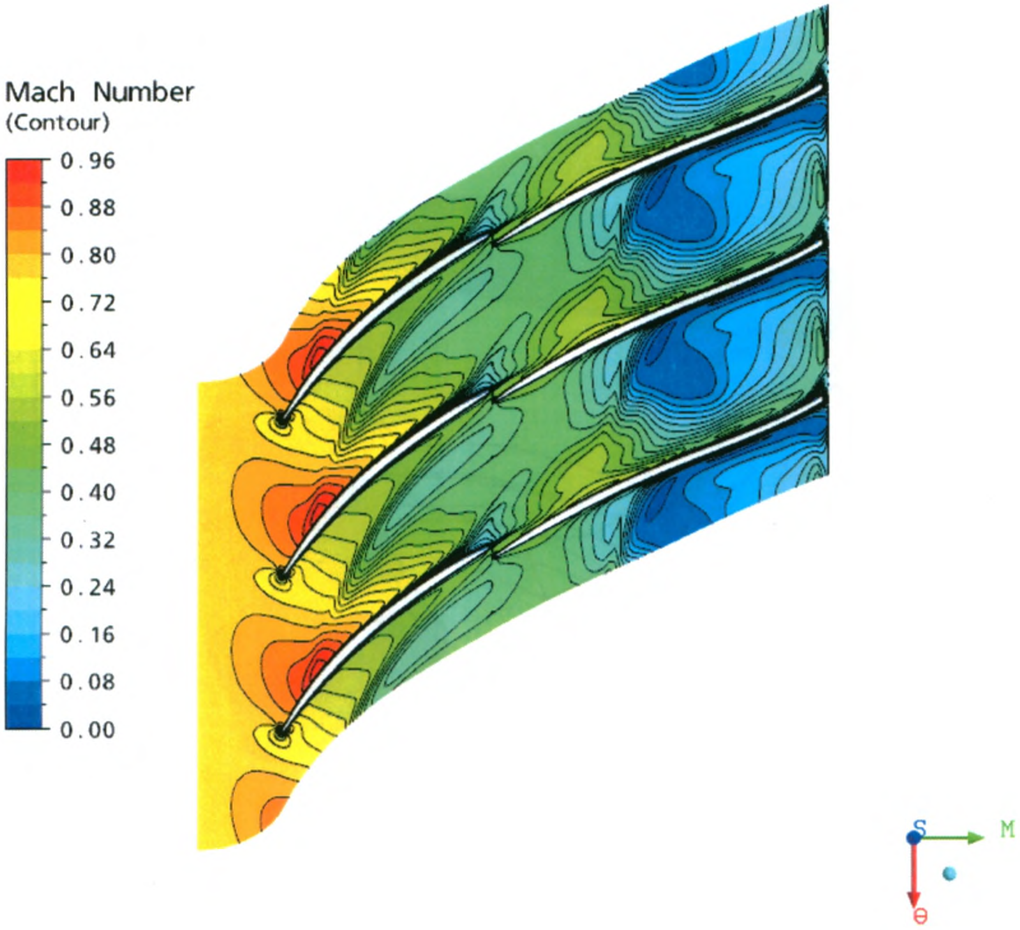

Figure 6.7: Blade-to-blade relative Mach number contours at 95% span.

Fig. 6.8 shows a global view of Mach number contours for streamwise cuts along the diffuser pipe. The deceleration of the flow is shown from the diffuser throat (the first plane in the upper right hand corner of the figure) to the diffuser exit (in the bottom left of the figure). It is seen that the side of the pipe with a larger turning radius shows a higher momentum zone.

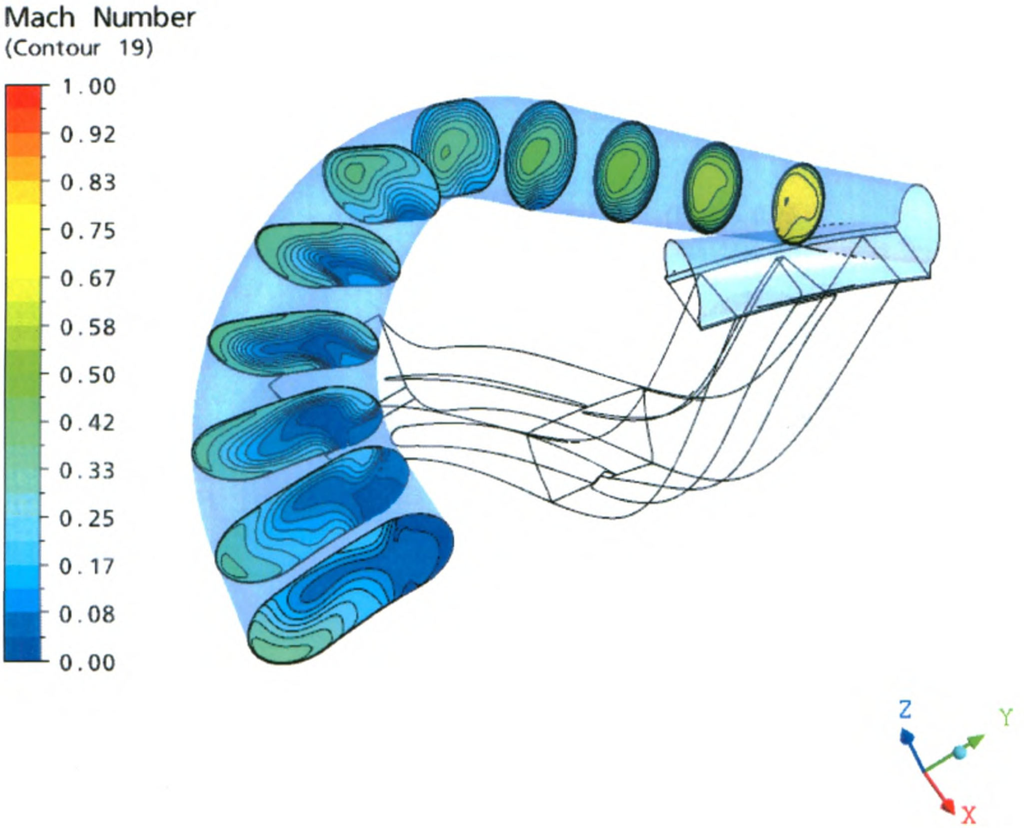

Figure 6.8: Diffuser pipe Mach number contours of cuts normal to the centreline.

For ease of viewing, every second plane in Fig. 6.8 is shown in Fig. 6.9. In Fig. 6.10 the streamlines projected on these planes are shown. As with typical curved duct flows, a counter-rotating vortex pair is found throughout the bend.

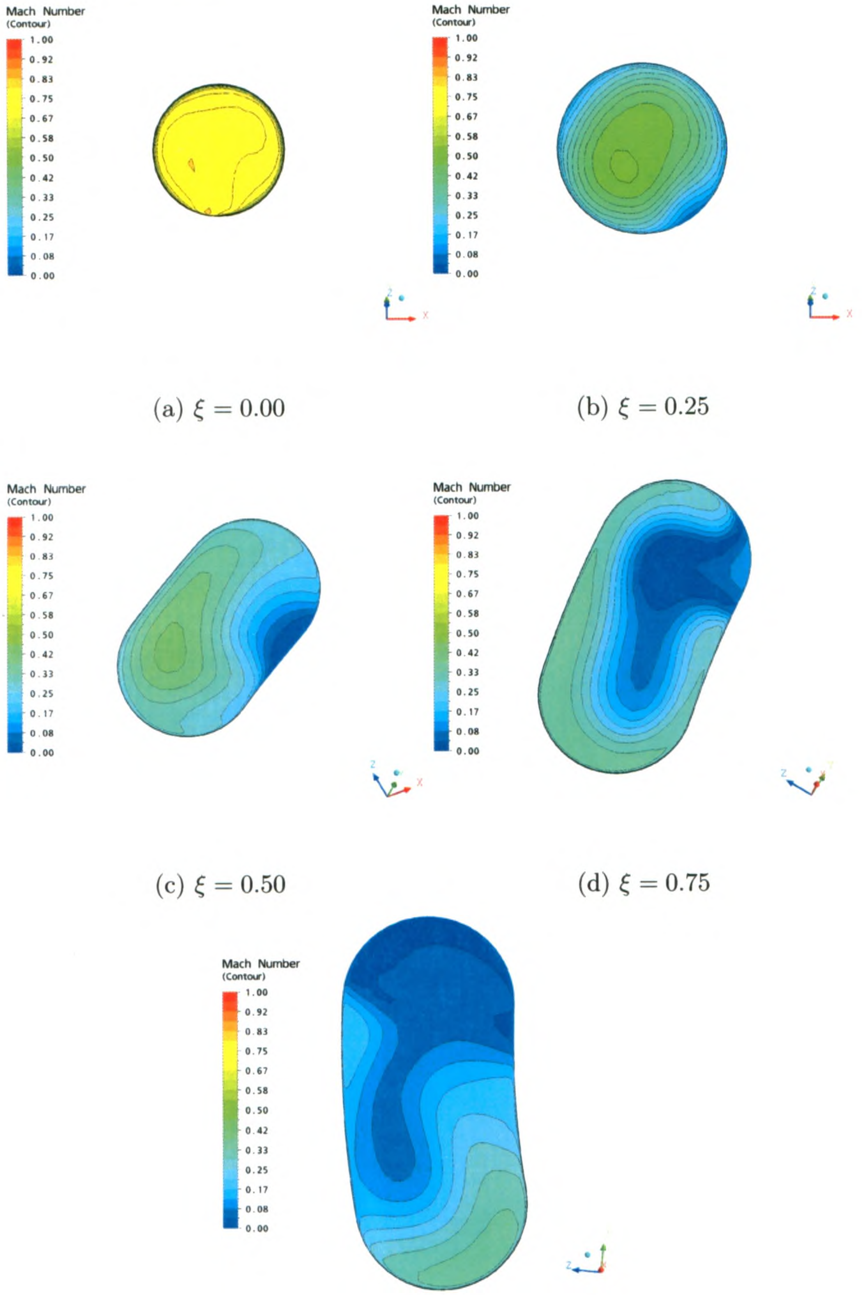

(a) $\xi = 0.00$

(b) $\xi = 0.25$

(c) $\xi = 0.50$

(d) $\xi = 0.75$

(e) $\xi = 1.00$

Figure 6.9: Mach number on streamwise cuts of the diffuser pipe from the throat ($\xi = 0$) to the exit ($\xi = 1$) for the SST turbulence model.

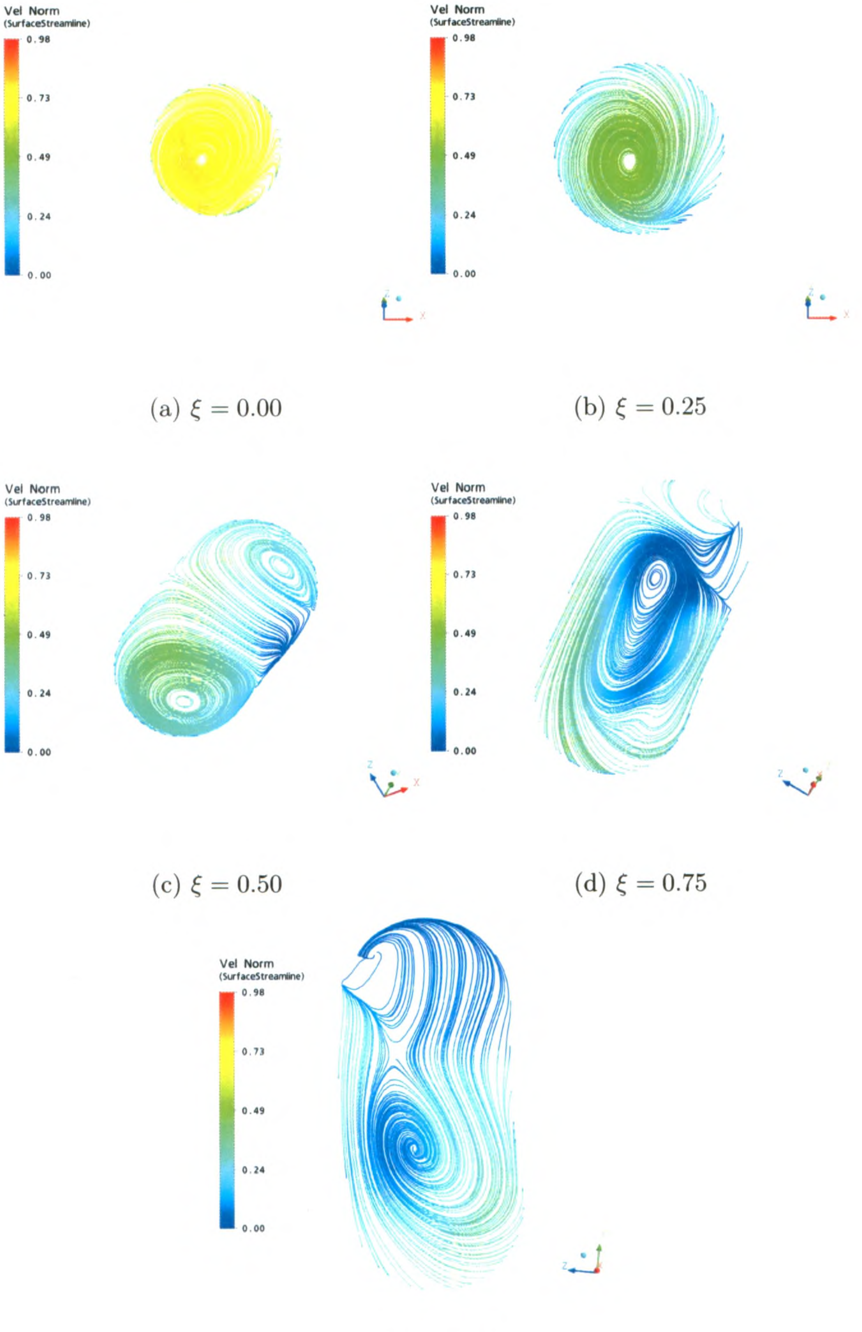

(a) $\xi = 0.00$ (b) $\xi = 0.25$

(c) $\xi = 0.50$ (d) $\xi = 0.75$

(e) $\xi = 1.00$

Figure 6.10: Projected streamlines on streamwise cuts of the diffuser for $\xi = [0, 1]$ for the SST turbulence model coloured by velocity normalized by the tip speed, C/U_2.

6.3 Summary

This chapter presented a description of the baseline case for the numerical simulations. The stage total to static pressure ratio, total to total temperature ratio, and total to static isentropic efficiency were presented along the speedline at 100% shaft and were compared against experimentally determined values. Performance predictions were quite accurate with some deterioration in accuracy towards choke and stall. In the following two chapters, the results of the baseline model will be compared against different representations of the geometry and different turbulence models.

Chapter 7

Assessment of a more accurate representation of the physical geometry

This chapter discusses an assessment of using a more accurate geometry to model the compressor stage. Firstly, the effects of trying to more accurately represent the true filleted geometry compared to the typical geometrical modeling at the root of the impeller blades was investigated. The approximated fillet geometry was incorporated in the baseline case discussed in Chapter 6. Secondly, a plenum downstream of the stage was modeled and analyzed with somewhat similar geometry to the actual plenum of the compressor test rig where experimental measurements are obtained for the stage. This latter investigation, in particular, is to analyze the effect of the location of the exit boundary on the flow by comparing the simulations with and without the plenum. The effect of using the more accurate fillet geometry is found to be more significant on performance parameters predicted. Consequently, all simulations presented, other than those cases shown in this chapter, have used this geometry, while the effect of the exit plenum is not as significant and so the plenum was not used subsequently due to the added computational expense of modeling another component. During the design process, the additional expense of modeling another component would typically win-out over a better representation of the geometry if performance is not shown to be affected. As with the grid independence study, all simulations carried out herein use the SST turbulence model.

7.1 Better fillet representation

Typically, computational studies of a turbomachine rotor do not model fillets at the root of the blade. The upper blade surface is extended to the hub such that the two surfaces are nearly orthogonal. Herein, the modeling of the fillet in this way is compared against an attempt to approximate the true filleted blade where there is a similar geometric blockage associated with the approximated geometry as there is in the true filleted blade. The full fillet is not modeled in order to avoid degenerate mesh angles (angles approaching zero degrees). A comparison of the typically modeled blade surface, the approximated fillet surface used herein, and the true fillet representation is shown in Fig. 7.1. To create the approximated geometry, a desired angle, ϕ, between the hub and blade surface at the root is chosen, and the height for the given angle and fillet radius is calculated such that at the cut-off, the tangent surface is extended downwards and meets the hub at the desired angle. Once the tangent surface is created, meshing of the geometry is possible without problems of degenerate angles. The angle used between the hub and the approximated fillet surfaces chosen for the study was $\phi = 45$ degrees since it models the majority of the geometric blockage while the mesh is not skewed excessively at the fillet-hub interface.

The locations for the rotor analyzed herein where degenerate mesh angles would occur with the true fillet modeling are at the interface between the inducer and exducer sections where the fillets on both blades have been partially ground off, and at the blunt exducer trailing edge. These surfaces are shown along with the inducer leading edge in Fig. 7.2. The figure presents a comparison between the typical modeled blade geometry, the approximated fillet geometry used in the study herein, and the true fillet geometry of the actual component. Where these blunt edges meet

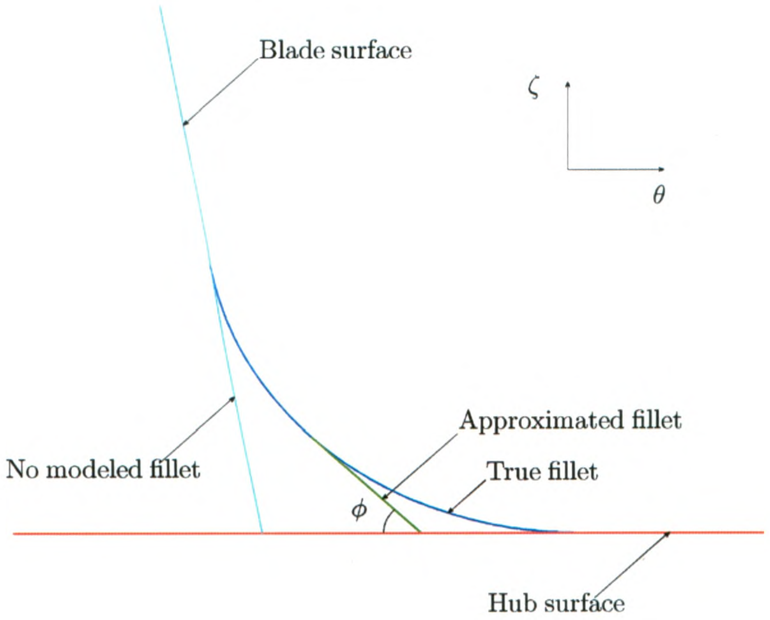

Figure 7.1: Comparison of geometry for the typical blade modeling, the approximated fillet modeling used as the standard case herein, and the true fillet representation.

the hub surface, the sharp edges meet at zero degrees which means that a body-fitted mesh would have angles approaching zero if a truncation technique was not used on the fillet surface.

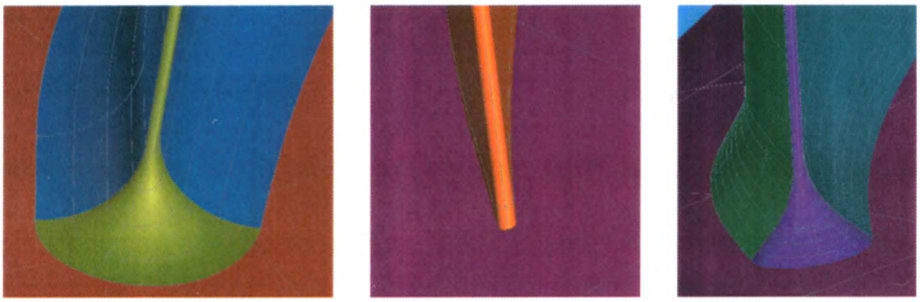

(a) True (b) Typical (c) Approximated

(d) True (e) Typical (f) Approximated

(g) True (h) Typical (i) Approximated

Figure 7.2: Comparison of details of geometry for the typical blade modeling, the approximated fillet modeling, and the true fillet representation at; (a),(b),(c) the inducer leading edge, (d), (e), (f) the inducer-exducer interface, and (g), (h), (i) the exducer trailing edge.

7.1.1 Speedline comparison

The most important performance parameters for the stage, namely, the total to static pressure ratio, the total to total temperature ratio, and the total to static isentropic efficiency, are shown in Figs. 7.3, 7.4, and 7.5, respectively, for the case of the impeller with and without (approximated) fillets. The effects of the fillets most importantly show a higher mass flow rate due to the reduced blockage without the fillets and a higher total temperature rise over the stage.

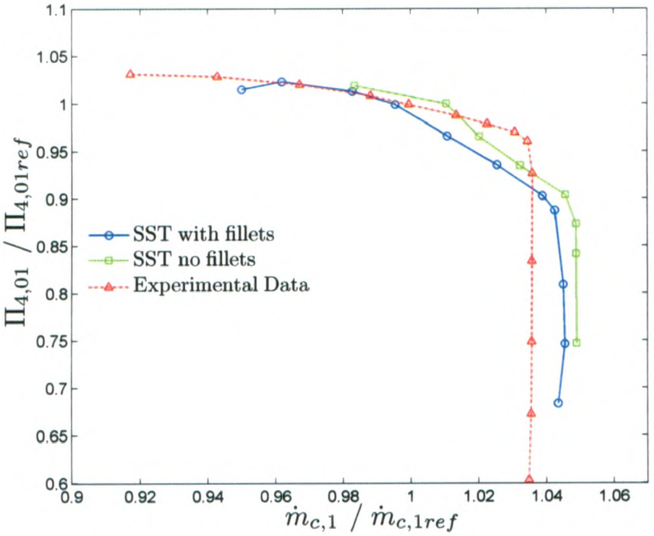

(a)

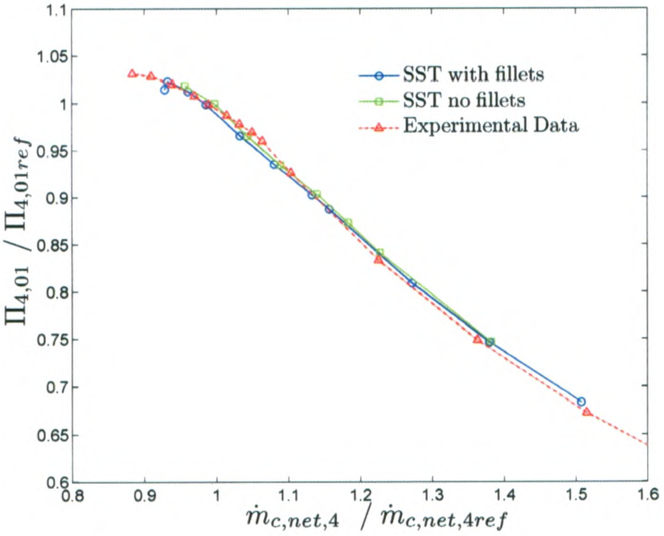

(b)

Figure 7.3: Normalized pressure ratio versus (a) inlet corrected flow rate and (b) net exit corrected flow rate.

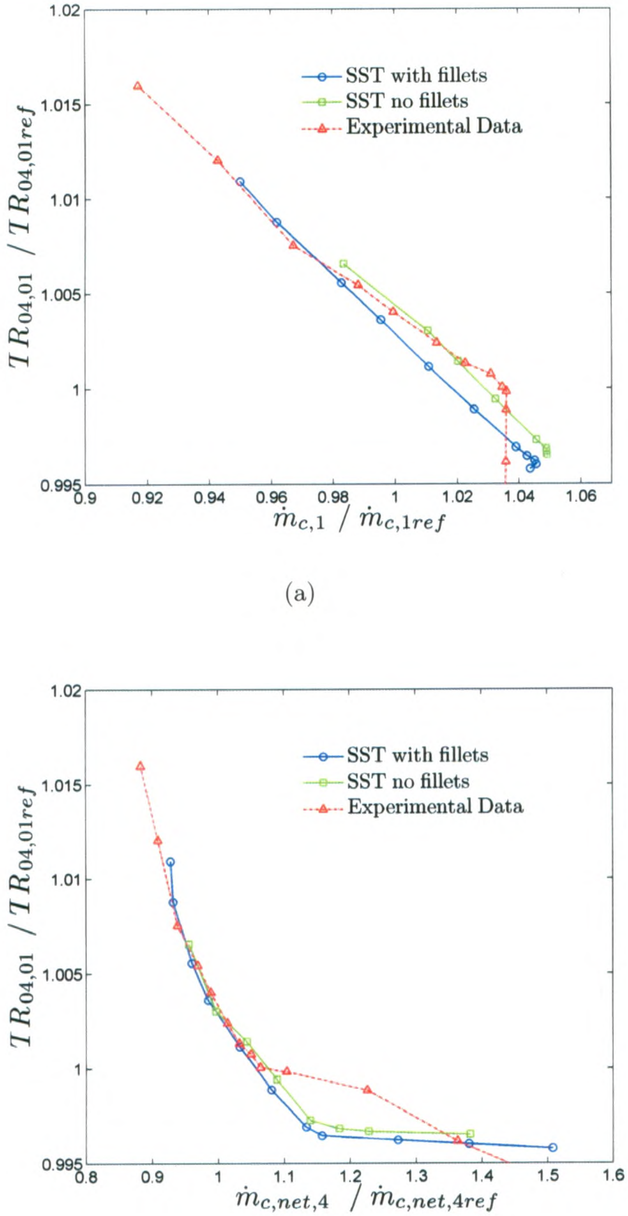

(a)

(b)

Figure 7.4: Normalized total temperature ratio versus (a) inlet corrected flow rate and (b) net exit corrected flow rate.

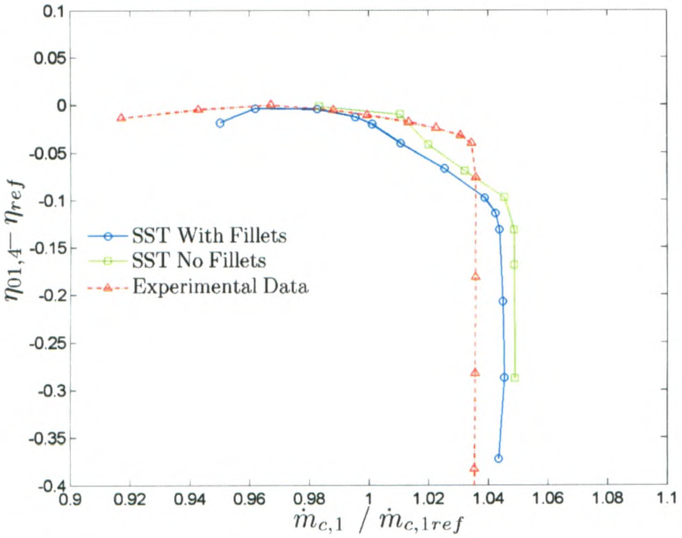

(a)

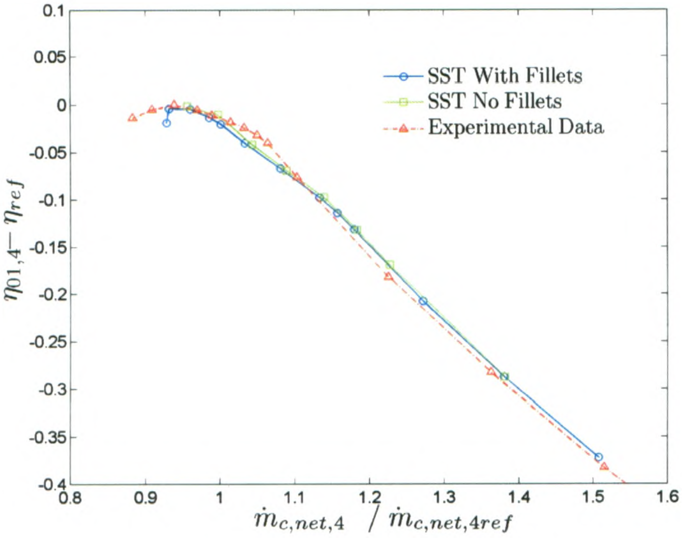

(b)

Figure 7.5: Efficiency change versus (a) inlet corrected flow rate and (b) net exit corrected flow rate.

7.1.2 Impeller streamwise effects of fillets

A plot of the difference in flow area without fillets (denoted with a subscript nf) to the flow area with fillets (denoted with a subscript f), $\Delta A = A_{nf} - A_f$, through the bladed section of the impeller is computed numerically for the geometries with approximated fillets and without fillets and is shown in Fig. 7.6 as a function of streamwise location and normalized by the impeller outlet area. The geometrical blockage of the blade across a constant streamwise cut is a function of the local blade angle, hence it varies across the impeller, and the variation is seen to be quite complicated.

It may be seen in Fig. 7.7 that the flow field itself is not significantly effected by the presence or absence of the fillets. Perhaps unsurprisingly, the main effect of the fillets is very localized in that they simply reduce the cross-sectional area available for the flow. Thus, for the same pressure rise across the stage, the mass flow rate has been increased. It may be seen from Fig. 7.6 that there is an area decrease of approximately 1%, while the mass flow rate has been reduced over the speedline by approximately 0.6% when the stage is not choked.

The choke mass flow rate is found to be reduced by 0.35% when modeling the fillets. The reason the mass flow rate changes is due to the change in the relationship between mass flow rate and pressure in the impeller. For the case of choking of the

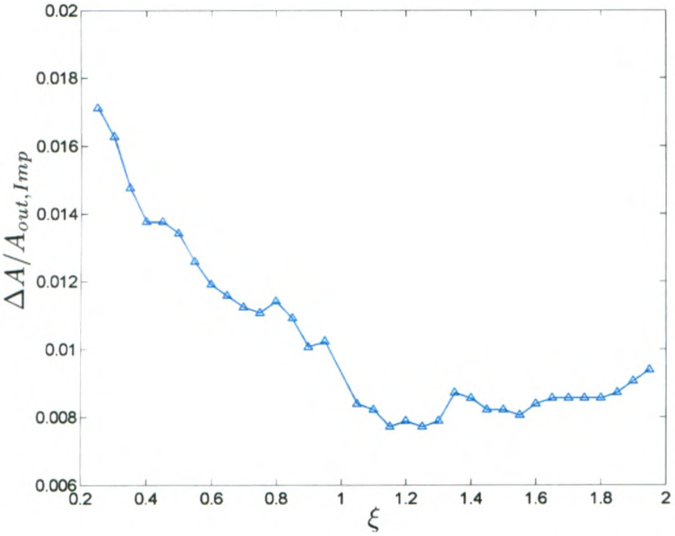

Figure 7.6: Difference in streamwise cross-sectional area for the unfilleted and approximated filleted geometries.

stage, we have choking at the diffuser throat, and since the mass flow rate at choke is given by the condition when the velocity at the throat is sonic, we have (denoting the choked throat quantities with an asterix),

$$\dot{m}^* = \rho^* A^*_{eff} a = \frac{p^*}{RT^*} A^*_{eff} \sqrt{\gamma RT^*} = \frac{p^*}{\sqrt{RT^*}} A^*_{eff} \sqrt{\gamma} \tag{7.1}$$

The choke mass flow, then, is a function of the geometry, the blockage, the pressure, the temperature, and the gas properties. Even though the diffuser geometry is the same, the pressure and temperature rise through the impeller are different because of the difference in impeller geometry. Assuming the effective area at the throat is the same, the ratio of mass flow rates for the filleted and unfilleted cases is then

$$\frac{\dot{m}_f^*}{\dot{m}_{nf}^*} = \frac{p_f^*}{p_{nf}^*}\sqrt{\frac{T_{nf}^*}{T_f^*}} \tag{7.2}$$

A very simple estimate of the amount of the geometric blockage of the fillets being modeled is 90% of the true blockage when approximating the fillets with the 45 degree angle between the hub and blade surface. It is assumed for this estimate that the upper blade surface and hub are orthodonal. Of course, the geometry is much more complicated than this, but the true blockage should be about 10% more than is actually being modeled. Extrapolating, the choke flow is likely predicted about 0.4% higher when fillets are not being modeled, and when out of choke, the mass flow for a given pressure ratio may be about 0.7% of that with the true fillets. Whether these effects are important to the designer to model or whether it would be more appropriate to simply scale the results by an approximate value of the blockage caused by the fillets would depend on the time and ressources available. Analysis of streamline patterns on constant streamwise surfaces throughout the impeller showed no indication of different physics other than the difference in mass flow from the blockage. The geometry of the ground fillets where the inducer and exducer sections are joined adds much more difficulty to the meshing the components. These geometric difficulties would not be encountered with conventional single-blade impellers where modeling of the fillets would be a fairly simple task.

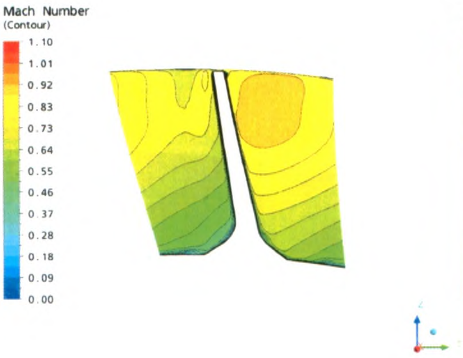

(a) $\xi = 0.30$

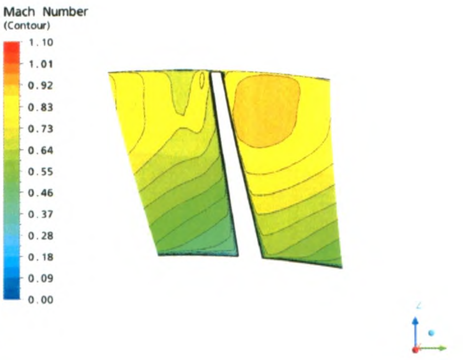

(b) $\xi = 0.30$

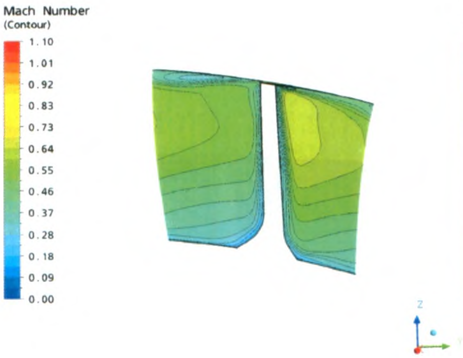

(c) $\xi = 0.70$

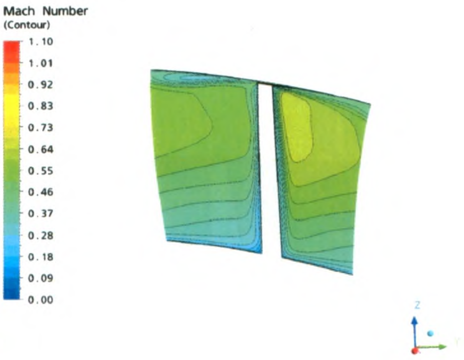

(d) $\xi = 0.70$

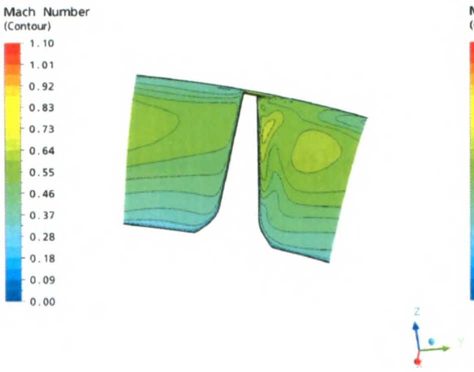

(e) $\xi = 1.20$

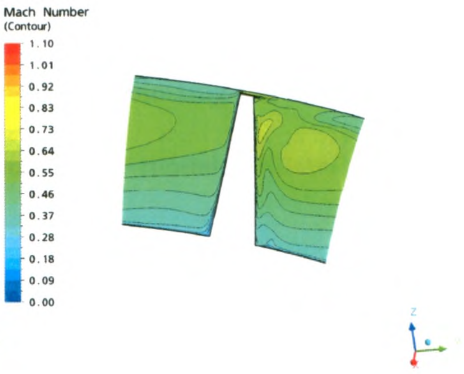

(f) $\xi = 1.20$

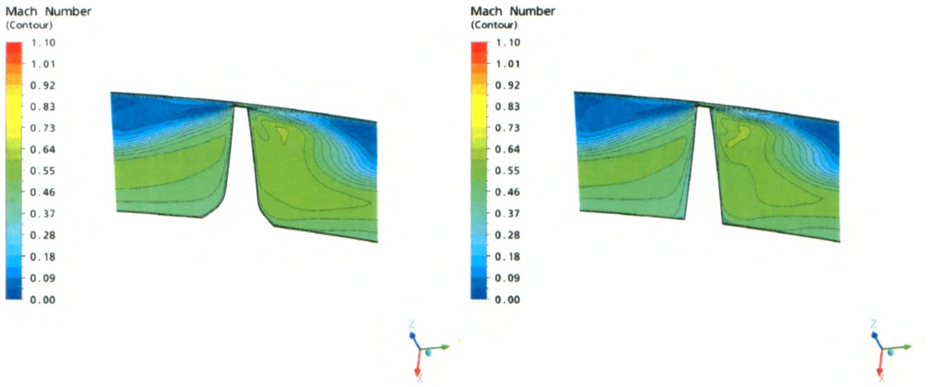

(g) $\xi = 1.60$ (h) $\xi = 1.60$

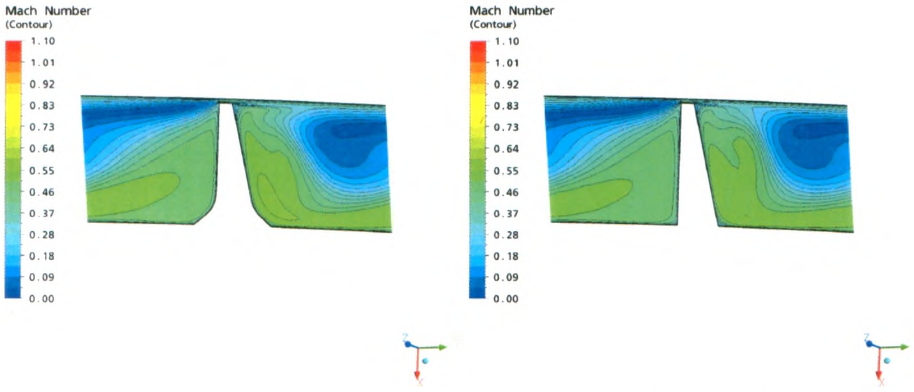

(i) $\xi = 1.90$ (j) $\xi = 1.90$

Figure 7.7: Streamwise cuts of the impeller gaspath plotting the relative frame Mach number for the cases with (left) and without (right) modeled fillets.

7.2 Exit plenum modeling

To assess the effect of the position of the computational boundary at the diffuser exit plane and to assess the constant pressure profile assumption, a plenum model was created. On the upstream side, the modeled plenum has the same dimensions as the test rig plenum, while on the downstream side a step change in the inner wall radius and a contraction are used to inhibit any recirculation at the plenum exit plane. The full geometry and the single passage geometry used for computations are shown in Fig. 7.8.

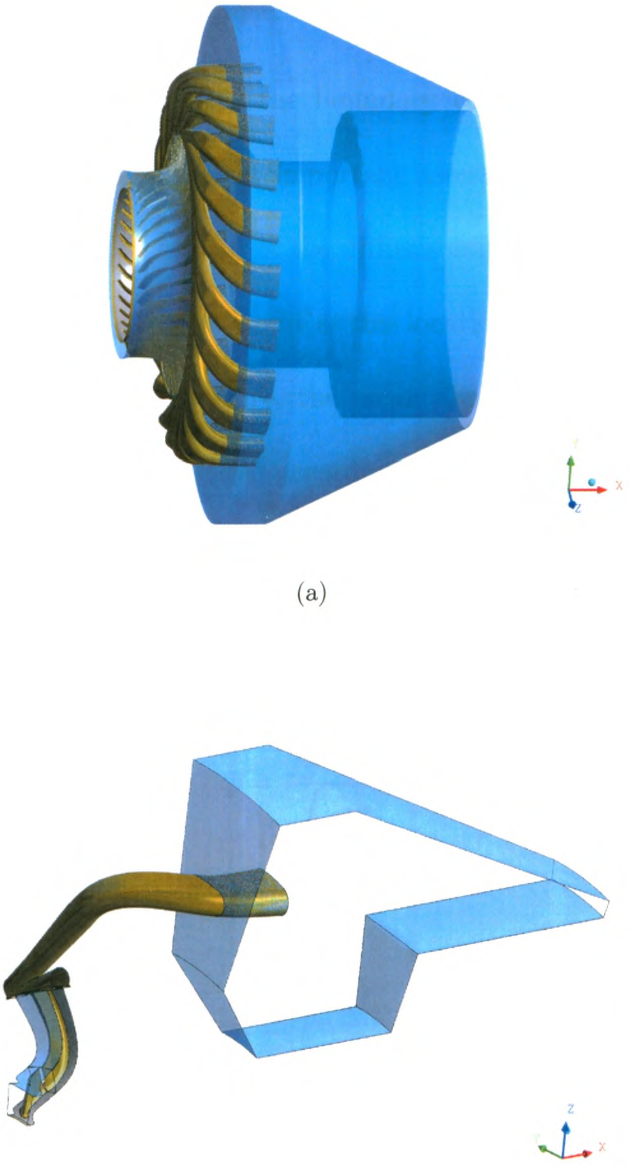

(a)

(b)

Figure 7.8: Modeled plenum downstream of the compressor stage, (a) full geometry, (b) computational domain.

7.2.1 Pressure profile

Since a constant pressure profile is the boundary condition used for simulations without the plenum, one of the most important assessments to be made with the modeling of the plenum downstream of the diffuser exit is the quantification of the deviation from a flat static pressure profile at this location. To quantify the deviation from the area averaged mean pressure, the mean absolute deviation and the root mean square deviation (both weighted according to the boundary area around each vertex on the surface which is associated with it in the solver) are examined. The area averaged pressure is defined as

$$\overline{p} = \frac{\int_S p\,dS}{\int_S dS} \tag{7.3}$$

or in discrete form

$$\overline{p} = \frac{\sum_{i=1}^{N} p_i (\Delta S)_i}{\sum_{i=1}^{N} (\Delta S)_i} \tag{7.4}$$

The area averaged deviation from the mean is calculated as

$$\overline{d_p} = \frac{\int_S |p - \overline{p}|\,dS}{\int_S dS} = \frac{\sum_{i=1}^{N} |p_i - \overline{p}|\,(\Delta S)_i}{\sum_{i=1}^{N} (\Delta S)_i} \tag{7.5}$$

and the root mean square deviation is given by

$$\sigma_p = \sqrt{\frac{\int_S (p-\overline{p})^2\, dS}{\int_S dS}} = \sqrt{\frac{\sum_{i=1}^{N} (p_i-\overline{p})^2 (\Delta S)_i}{\sum_{i=1}^{N} (\Delta S)_i}} \tag{7.6}$$

For the simulation calculated very near design conditions, the averaged deviation and root mean square deviation were 0.08% and 0.11% from the mean, respectively. This negligible deviation from the mean justifies the use of a constant pressure profile at this location in the simulations without a plenum. If the calculations were to simulate the flow through the actual engine, the assumption of a flat profile may not hold since, typically, the combustor sits very close to the diffuser exit and so may have a very significant impact on the homogeneity of the pressure field at this plane. For validation with the experiments undertaken in this study, however, it is the pressure field at the pipe-exit with the plenum which is most important, and such small deviations show that the constant pressure boundary condition is appropriate when undertaking simulations without a downstream plenum.

7.2.2 Speedline comparison

As in the case of the fillet modeling analysis, the stage total to static pressure ratio, total to total temperature ratio, and the total to static efficiency are compared for the simulations with and without the exit plenum in Figs. 7.9, 7.10, and 7.11. It is seen that there is no significant difference in performance parameters for the cases with and without fillets.

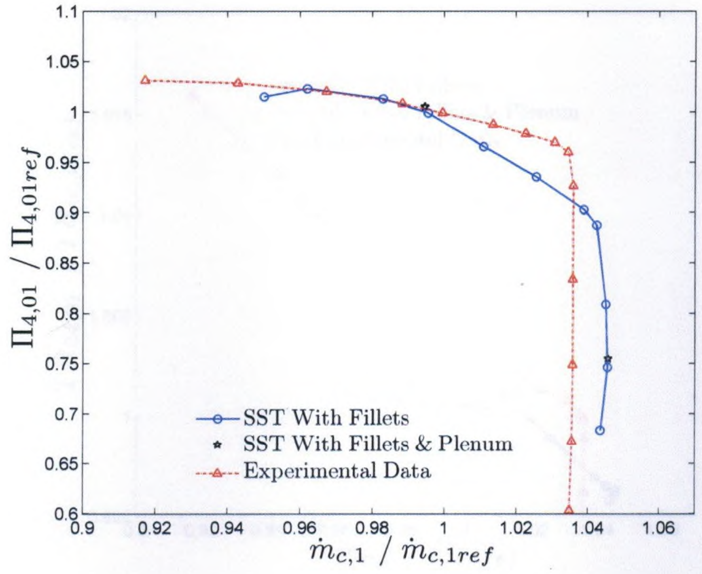

(a)

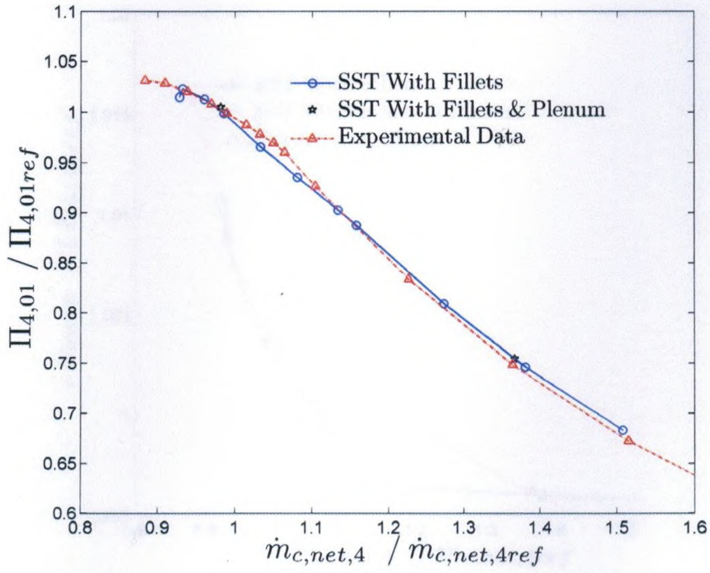

(b)

Figure 7.9: Normalized pressure ratio versus (a) inlet corrected flow rate and (b) net exit corrected flow rate.

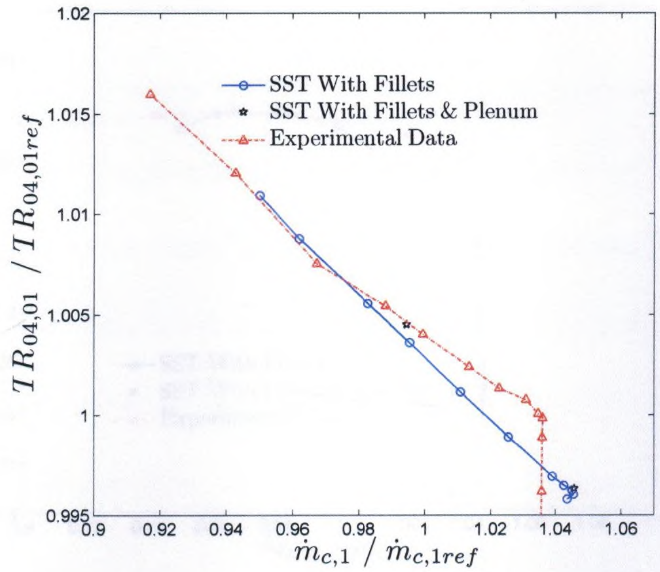

(a)

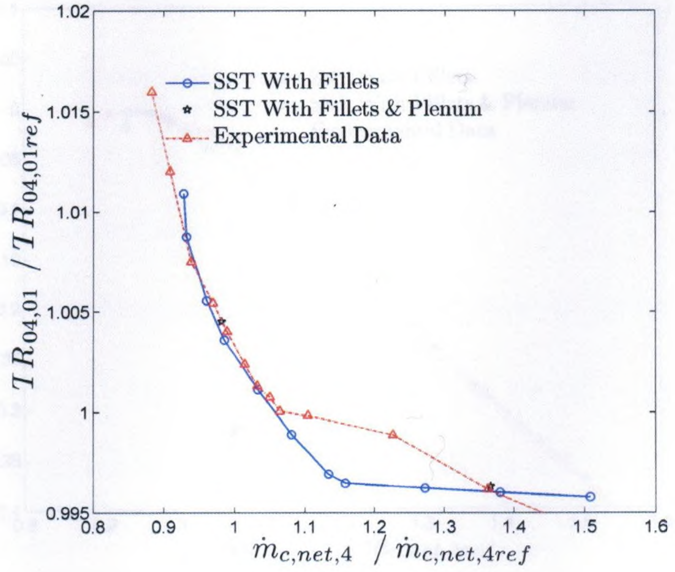

(b)

Figure 7.10: Normalized total temperature ratio versus (a) inlet corrected flow rate and (b) net exit corrected flow rate.

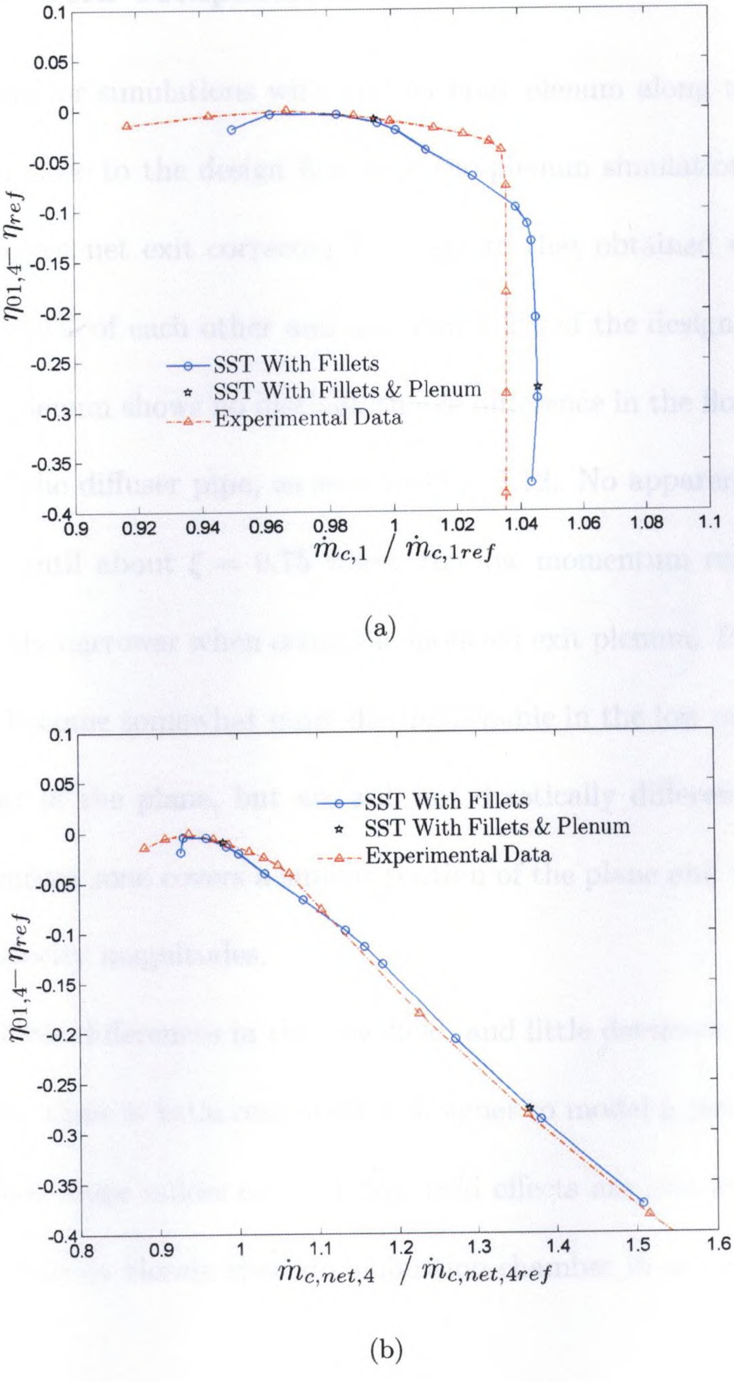

(a)

(b)

Figure 7.11: Efficiency change versus (a) inlet corrected flow rate and (b) net exit corrected flow rate.

7.2.3 Flow field comparison

Flow field results for simulations with and without plenum along the speedline are compared quite close to the design flow rate (no-plenum simulations compared are taken at the closest net exit corrected flow rate to that obtained with the plenum and are within 0.4% of each other and are within 2% of the design flow rate). The addition of the plenum shows no distinguishable difference in the flow field except in the very end of the diffuser pipe, as seen in Fig. 7.12. No apparent differences are distinguishable until about $\xi = 0.75$ where the low momentum region attached to the wall is slightly narrower when using the modeled exit plenum. By the exit plane, the differences become somewhat more distinguishable in the low momentum region that spans most of the plane, but are still not drastically different. In particular, the high momentum zone covers a similar portion of the plane and has, for the most part, similar velocity magnitudes.

With such little differences in the flow field, and little deviation in pressure from a constant value, there is little reason for a designer to model a plenum downstream of the compressor stage unless coupled flow field effects are important between the diffuser and a possibly closely spaced combustion chamber in an actual engine.

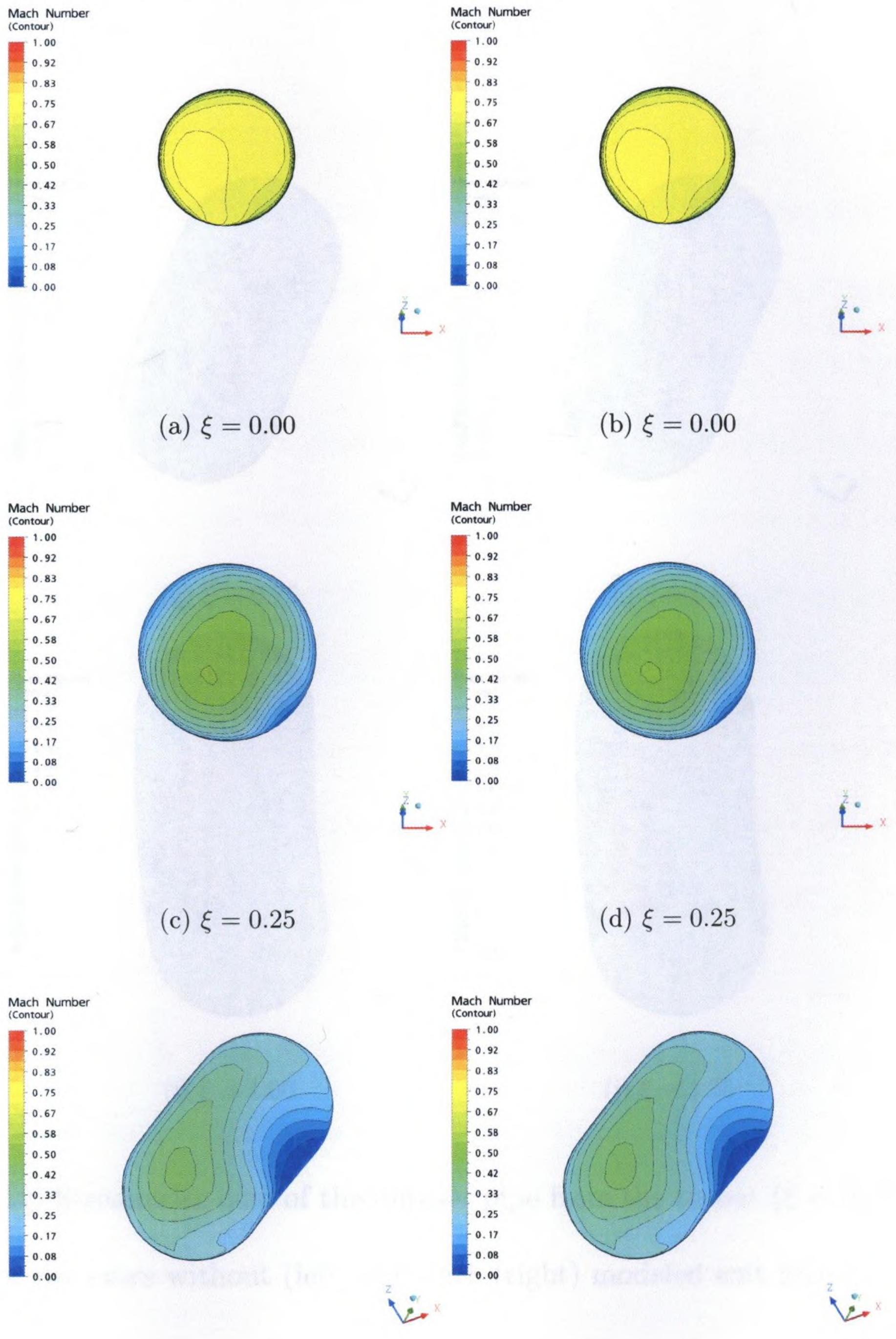

(a) $\xi = 0.00$ (b) $\xi = 0.00$

(c) $\xi = 0.25$ (d) $\xi = 0.25$

(e) $\xi = 0.50$ (f) $\xi = 0.50$

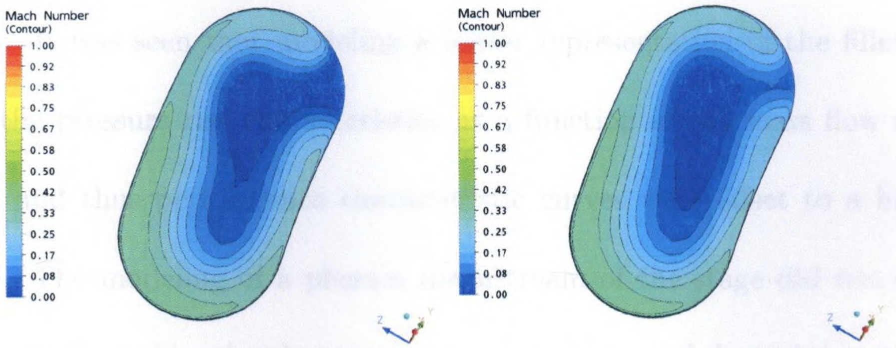

(g) $\xi = 0.75$ (h) $\xi = 0.75$

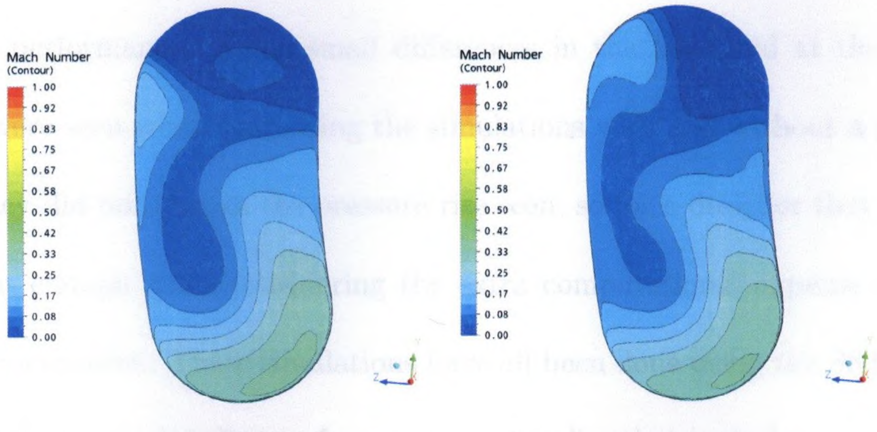

(i) $\xi = 1.00$ (j) $\xi = 1.00$

Figure 7.12: Streamwise cuts of the diffuser pipe from the throat ($\xi = 0$) to the exit ($\xi = 1$) for the cases without (left) and with (right) modeled exit plenum.

7.3 Summary

Two assessments were made of using more accurate representations of the physical geometry. It was seen that modeling a better representation of the fillet geometry changes the pressure rise characteristics as a function of the mass flow rate in the impeller, and thus performance characteristic curves were offset to a higher mass flow rate. The modeling of a plenum downstream of the stage did not change the pressure or temperature rise characteristics in the stage, and showed that the constant pressure boundary condition applied when not modeling the plenum are valid in terms of performance. Some small differences in the flow field at the end of the diffuser were seen when comparing the simulations with and without a plenum, but again, they did not change the pressure rise seen, so for a designer they may not be important enough when considering the extra computational expense of modeling another component. These simulations have all been done using the SST turbulence model, and because it is known from previous studies that turbulence modeling does have effects on the quality of predictions, it is to this issue that we turn in the next chapter.

Chapter 8

Comparison of turbulence model predictions

The aim of the investigation in this chapter is to address the issue that the complex flow field in turbomachinery components is quite a challenging problem in terms of turbulence modeling techniques. Significant differences are found with different models and there is a need for an investigation of best practices for modeling. Herein, the predictions for the flow field of this compressor stage obtained with the turbulence models discussed in Chapter 3 are compared and evaluated.

8.1 Speedline results and discussion

Fig. 8.1 compares the measured and numerically computed total to static pressure ratios against inlet corrected flow and net exit corrected flow, respectively. It is found that the $k-\epsilon$ model seems to over-predict the pressure-rise in the compressor stage when compared to the SST and RSM-SSG models. The SST-RM turbulence model results obtained lie approximately midway between the SST and $k-\epsilon$ results. The choke mass flow is over-predicted in the case of the SST model by about 0.9%, which is deemed acceptable since the estimated uncertainty of the mass flow measurement itself is about 1%. The RSM-SSG and SST-RM predictions are about the same at 2.4% and 2.2% higher than the experimentally determined inlet corrected choke flow rate, respectively. The $k-\epsilon$ model predicts the highest choke flow rate which is 3.3% above the experimental value.

It is clearly seen in Fig. 8.2 that, again, the $k-\epsilon$ model over-predicts the total to total temperature ratio, meaning that the predictions show that a higher amount of work is being done on the fluid through the compressor stage than is actually being done. The SST-RM model lies between the results of the $k-\epsilon$ model and the SST model. The experimental drop-off in the temperature ratio with inlet corrected mass flow is most closely predicted by the RSM-SSG model, with the SST model dropping at a slightly higher rate just before the onset of choke. Other than the choke flow rate, the RSM-SSG results lie closest to the experimental results. The range of the choke total temperature ratio for the different models is about 1.1%. Note for models other than the SST model, the full profile has not been captured in Fig. 8.2(b), but the curves should show a similar shape as that for the SST model.

Fig. 8.3 shows the change in stage total to static efficiency from a reference condition, again plotted against the inlet corrected and net exit corrected flow rates. The SST model shows good agreement with the experimental data near the design flow rate and shows an under-prediction as the choke flow is approached. Despite much poorer prediction in terms of other performance parameters, the $k-\epsilon$ model efficiencies calculated for the simulations carried out do not lie far from the experimental curve. The SST-RM and RSM-SSG data agree well for the points calculated near the design flow rate, and as with other parameters, the most significant differences are seen on the choke side.

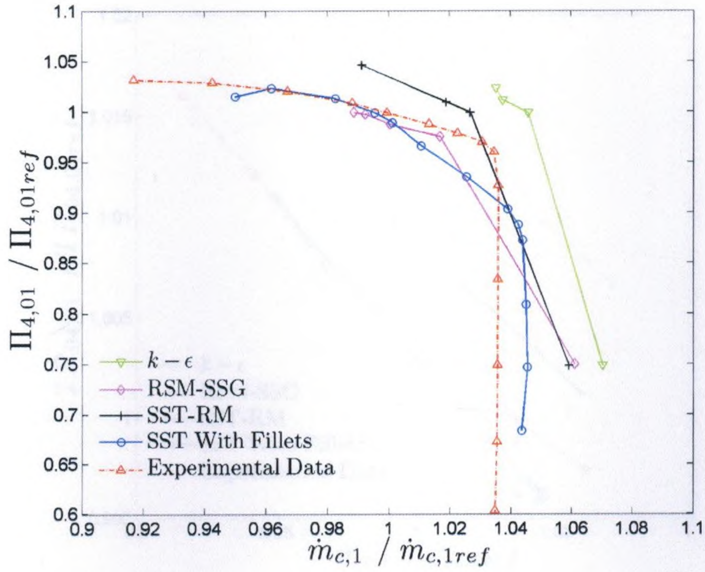

(a)

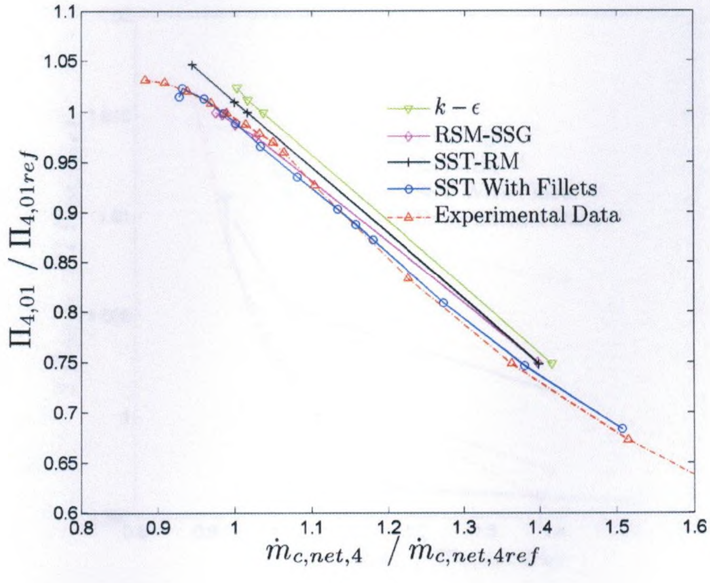

(b)

Figure 8.1: Normalized pressure ratio versus (a) inlet corrected flow rate and (b) net exit corrected flow rate.

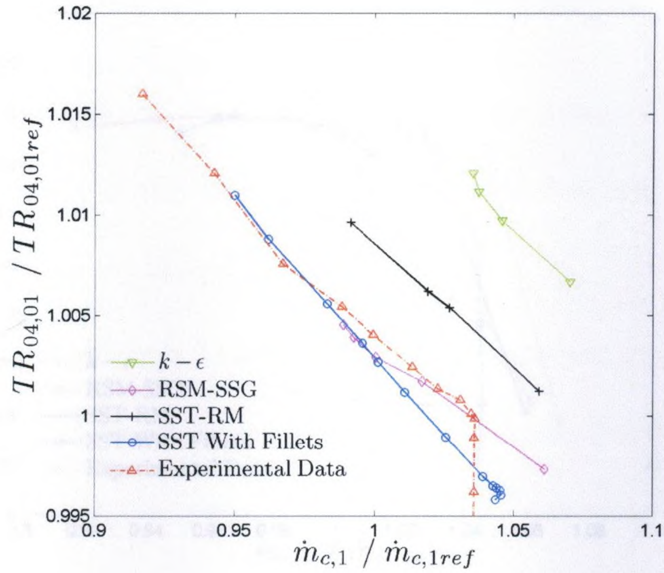

(a)

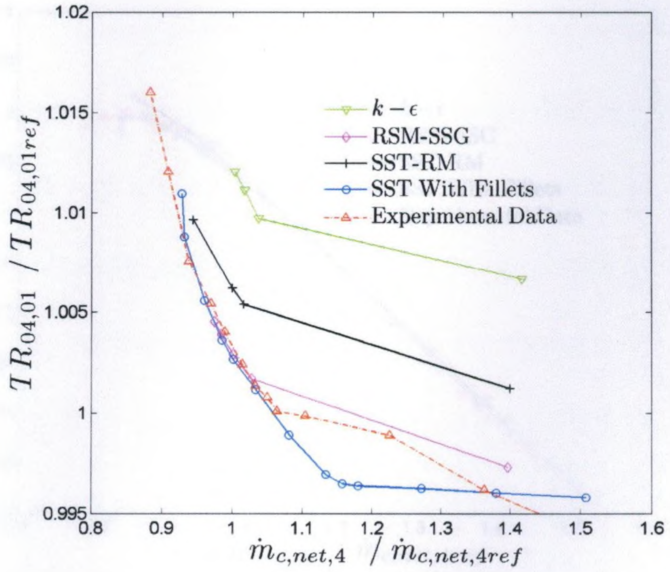

(b)

Figure 8.2: Normalized total temperature ratio versus (a) inlet corrected flow rate and (b) net exit corrected flow rate.

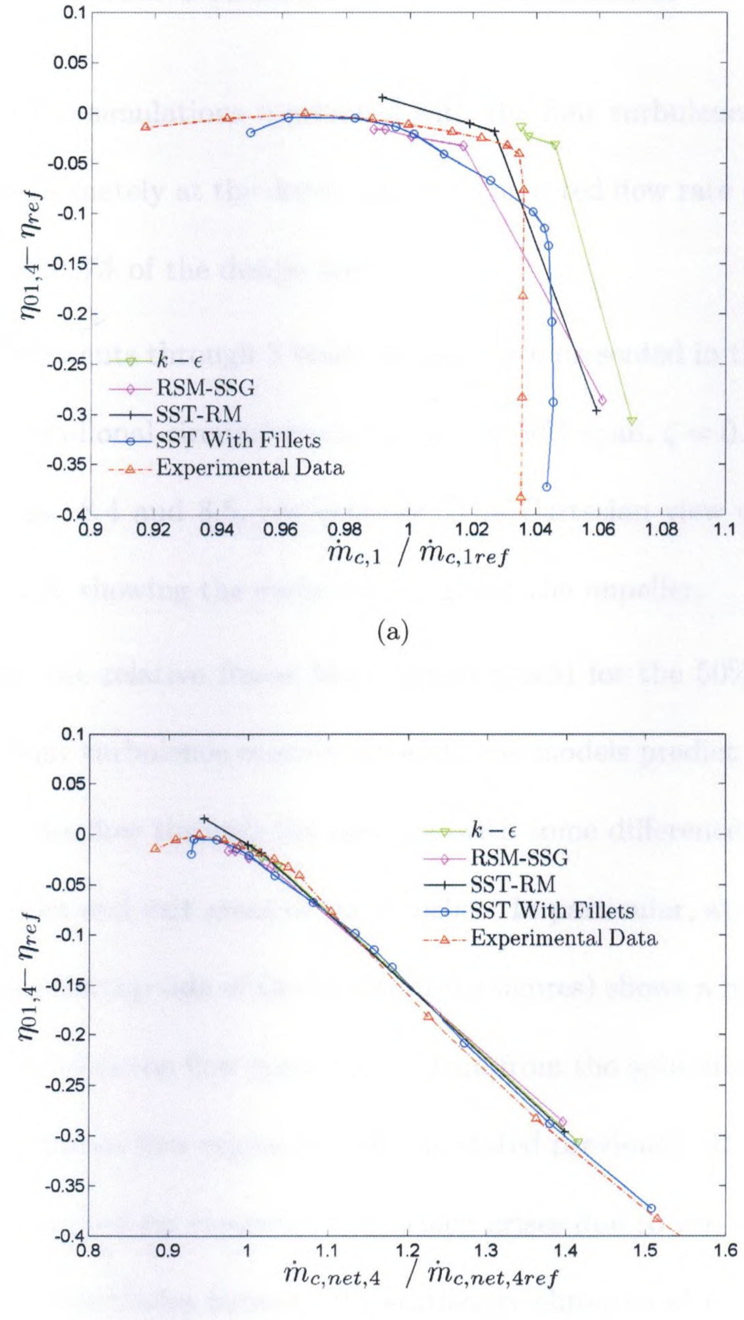

(a)

(b)

Figure 8.3: Efficiency change versus (a) inlet corrected flow rate and (b) net exit corrected flow rate.

8.2 Flow field results and discussion

In this section the simulations conducted with the four turbulence models are discussed, all approximately at the design net exit corrected flow rate (no run deviating by more than ± 0.3% of the design flow).

First, spanwise cuts through 3 blade passages are presented in the blade-to-blade view (i.e. the meridional-circumferential plane) at 50% span, $\zeta = 0.5$, and 95% span, $\zeta = 0.95$ in Figs. 8.4 and 8.5, respectively. The Cartesian view of these cuts was shown in Fig. 6.5, showing the surface throughout the impeller.

In Fig. 8.4, the relative frame Mach number field for the 50% spanwise cut is shown for the four turbulence models. Overall, the models predict a similar relative deceleration of the flow through the passage, with some differences apparent in the figures at the inlet and exit areas of the impeller. In particular, at the inducer inlet, the suction side (the top side of the blades in the figures) shows a higher acceleration for the $k - \epsilon$ model as the flow gains momentum from the spinning impeller. At the exit, a low momentum flow region is seen. As stated previously, this is the footprint of the highly distorted tip clearance flow which arises due to the shear in the small gap at the tip of the blades between the stationary shroud and the rotating blade.

Fig. 8.5 shows the 95% span blade-to-blade view where the low momentum and highly distorted zone at the exit of the impeller is even more pronounced, and differences are seen especially in the latter portion of the blade passage. To highlight the differences in the flow field, the projected streamlines on a constant streamwise surface at $\xi = 1.9$ is shown in Fig. 8.6. We see the projected streamlines indicating the secondary flows only show a full roll-up of the tip clearance flow in the results with the SST and RSM-SSG models. Even between these two models, there is a significant difference in the flow pattern of the swirling flow from the tip clearance gap.

Projected streamlines plotted on a constant streamwise surface at $\xi = 1.95$ near the trailing edge of the exducer blade are shown in Fig. 8.8 along with the surface limiting streamlines. To make it clear what is being presented in this figure, the constant streamwise surface is shown relative to the passage geometry in Fig. 8.7. The projected streamlines on the constant streamwise surface indicate that for both the cases of the SST and RSM-SSG models, the flow through the tip gap from the pressure surface side (lower surface in the figures) to the suction surface side has a recirculating region, where reattachment occurs before exiting onto the other side of the blade, whereas the $k-\epsilon$ model shows an attached flow, indicating different physics being predicted in the tip gap region. The limiting streamlines show the steady-state flow paths near the wall, and the differences in velocities are apparent between the models using the ω-equation that are integrated through the sublayer and the models using the ϵ-equation with wall-functions where the scalable wall-functions limit the minimum distance from the wall such that it is outside the sublayer, and thus has higher velocities. The limiting streamlines show the reattachment line for the SST and SST-RM are more similar compared to the shorter reattachment length seen for the RSM-SSG model. The low momentum region predicted by the RSM-SSG model is also more complicated after reattachment compared to the other two-models showing separation.

To further investigate the impeller exit flow, the mean impeller radial and tangential velocity exit profiles on the diffuser side of the mixing plane for the four models is extracted from these simulations and is shown in Fig. 8.9 and are normalized by the tip speed of the impeller. At the time of submission of this thesis, only a single measurement traverse of this location is available. For direct comparison, the experimental data should be pitch-averaged as this is the effect of using a mixing plane. These profiles will be compared against this data in Chapter 9, but first we mention some of the important differences seen by changing the turbulence modeling used. The relative velocity throughout most of the span is predominantly radial at this location, with the exception of the tip region which is highly influenced by the presence of the shroud. It is seen that there is a fairly good agreement between all models throughout most of the passage, but on the shroud side all models predict some flow reversal such that the flow goes back upstream along the shroud with the exception of the $k-\epsilon$ and RSM-SSG models. The SST model predicts the most significant amount of reversal, followed by the SST-RM. The tangential velocity in this tip region also shows very different physics in this very-near shroud region. The RSM-SSG model predicts an increase in tangential velocity, while the $k-\epsilon$ model shows a nearly constant velocity, and the last two models show a decrease in tangential velocity here. Velocity vectors plotted show that the flow is much more disorganized in the case of the RSM-SSG model, especially in the wake of the blade and the flow following the tip. The speed up in circumferential velocity is seen with this model at the mixing plane just downstream of the tip very near to the shroud.

The spanwise distribution of the swirl on the diffuser side of the mixing plane is shown in Fig. 8.10. Also shown is the diffuser elliptical leading edge metal angle, i.e. an effective camber-line value for the leading edge which is formed by the intersections of cylindrical drillings. The difference of the metal angle and the swirl velocity gives the incidence seen by the leading edge. Maxima are seen near the shroud for the two SST models, while the two other models show no such maxima and tend towards 90 degrees at the shroud.

Finally, the results for an estimate of the blockage at the exit of the impeller are presented. Blockage is given by

$$B = 1 - \frac{A_{eff}}{A_{geom}} \tag{8.1}$$

where A_{eff} is the effective flow area and A_{geom} is the geometric flow area. In a flow like the exit flow from the impeller, there is no core region of constant velocity bounded by hub and shroud boundary layers. Rather, the flow is more nearly a fully-developed turbulent flow (Cumpsty, 1989). The effective area, then, is not exactly clear. The blockage is estimated at the impeller exit by determining the area necessary for a one-dimensional compressible flow with the same massflow averaged relative Mach number, relative total temperature and pressure, and massflow through a given surface. i.e.

$$\begin{aligned} \dot{m} =& \rho V_{rel} A_{eff} = \frac{p}{RT} M_{rel} \sqrt{\gamma R T} A_{eff} \\ =& \frac{p_{0rel}}{\sqrt{RT_{0rel}}} \sqrt{\gamma} M_{rel} A_{eff} \left(1 + \frac{\gamma - 1}{2} M_{rel}^2\right)^{(\gamma+1)/(2-2\gamma)} \end{aligned} \tag{8.2}$$

The effective area is then given by

$$A_{eff} = \dot{m} \frac{\sqrt{RT_{0rel}}}{p_{0rel}\sqrt{\gamma} M_{rel}} \left(1 + \frac{\gamma - 1}{2} M_{rel}^2\right)^{(\gamma+1)/(2\gamma-2)} \tag{8.3}$$

These blockage estimates are presented in Table 8.1. It is seen that the exit blockage is about 5% lower in the case of the $k - \epsilon$ model than in the SST and RSM-SSG models which differ by less than a percentage point. The SST-RM blockage estimate is closer to that predicted by the $k - \epsilon$ model.

Table 8.1: Impeller exit blockage estimates for the three turbulence models.

Turbulence model	Impeller exit blockage, B_2
$k - \epsilon$	0.144
SST	0.200
SST-RM	0.162
RSM-SSG	0.192

The aerodynamic slip factor, σ, will also affect the performance of the stage. It is given by the ratio of the blade exit tangential velocity and the ideal tangential velocity at which the fluid would exit if it followed the blade metal angle.

$$\sigma = \frac{c_{\theta 2}}{c_{\theta 2i}} = \frac{c_{\theta 2}}{U_2 - c_{m2} \tan\left(\beta_{2metal}\right)} \tag{8.4}$$

Fig. 8.11 shows the predicted slip over the speedline points calculated. It is seen that there is about a 4% variation in aerodynamic slip factor between the turbulence models. The higher slip predicted by the $k - \epsilon$ model is related to a higher work done on the flow in the compressor. As stated by Cumpsty (1989), the slip factor is typically a very weak function of the flow rate, but the SST model predictions show an increase of slip as the flow rate through the impeller is decreased. Over the range predicted with the other models, little variation was seen. It would be interesting in a future study to capture make predictions for the models at lower flow rates to see if this effect is also seen.

Fig. 8.12 shows a global view of Mach number contours for streamwise cuts along the diffuser pipe. For each turbulence model, the deceleration of the flow from the diffuser throat (the upper section of the first plane) to the diffuser exit (in the bottom left of the figures) can be seen. In all cases, the side of the pipe with a larger turning radius shows a higher momentum zone. This zone is the largest in the case of the $k - \epsilon$ model which also notably has the highest throat Mach number. The flow obtained using the RSM-SSG model shows the most pronounced secondary flow patterns, seen especially in the furthest upstream portions of the pipe.

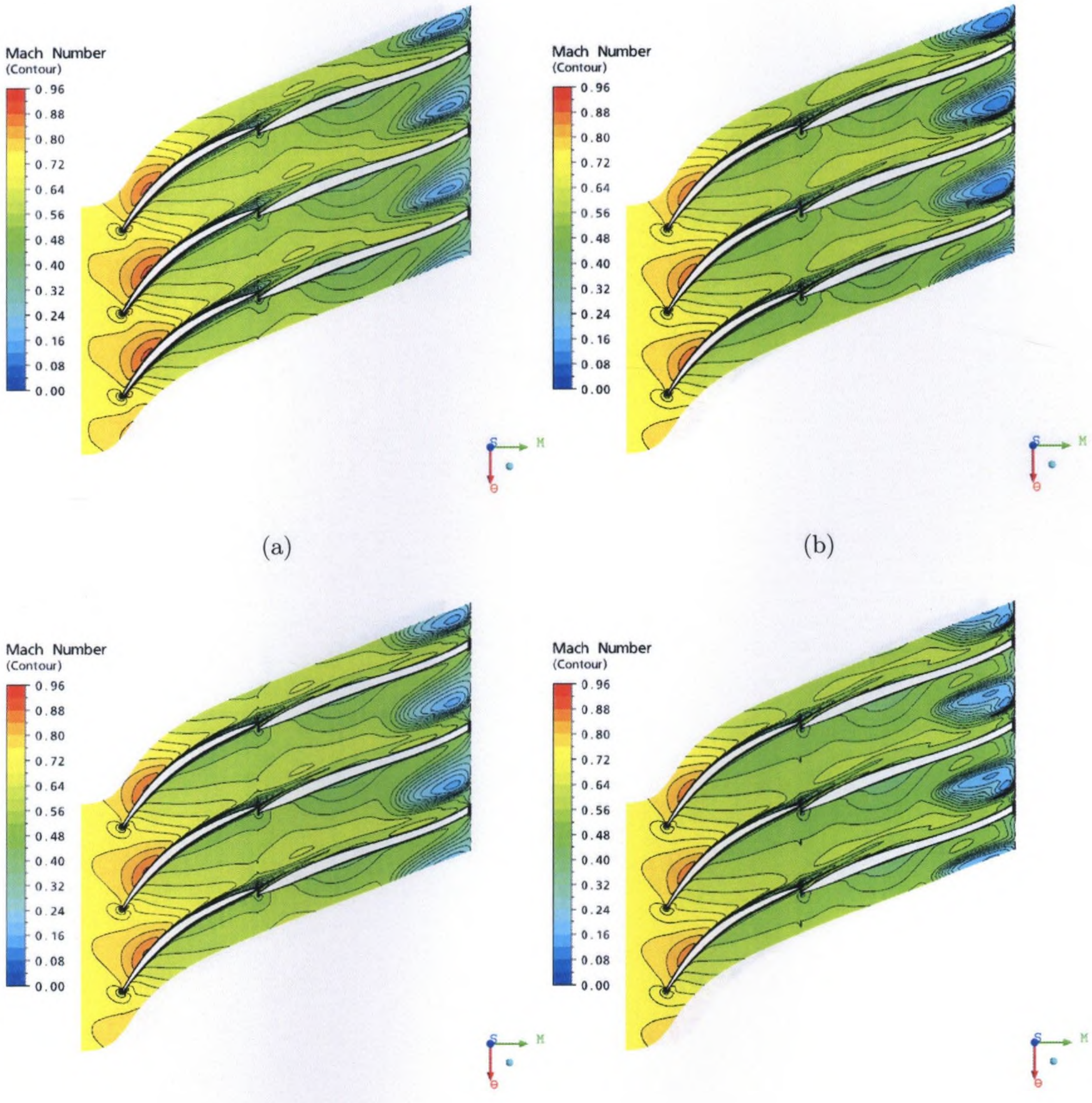

(a) (b)

(c) (d)

Figure 8.4: Blade-to-blade relative Mach number contours at 50% span for the (a) $k - \epsilon$, (b) SST, (c) SST-RM, and (d) RSM-SSG models.

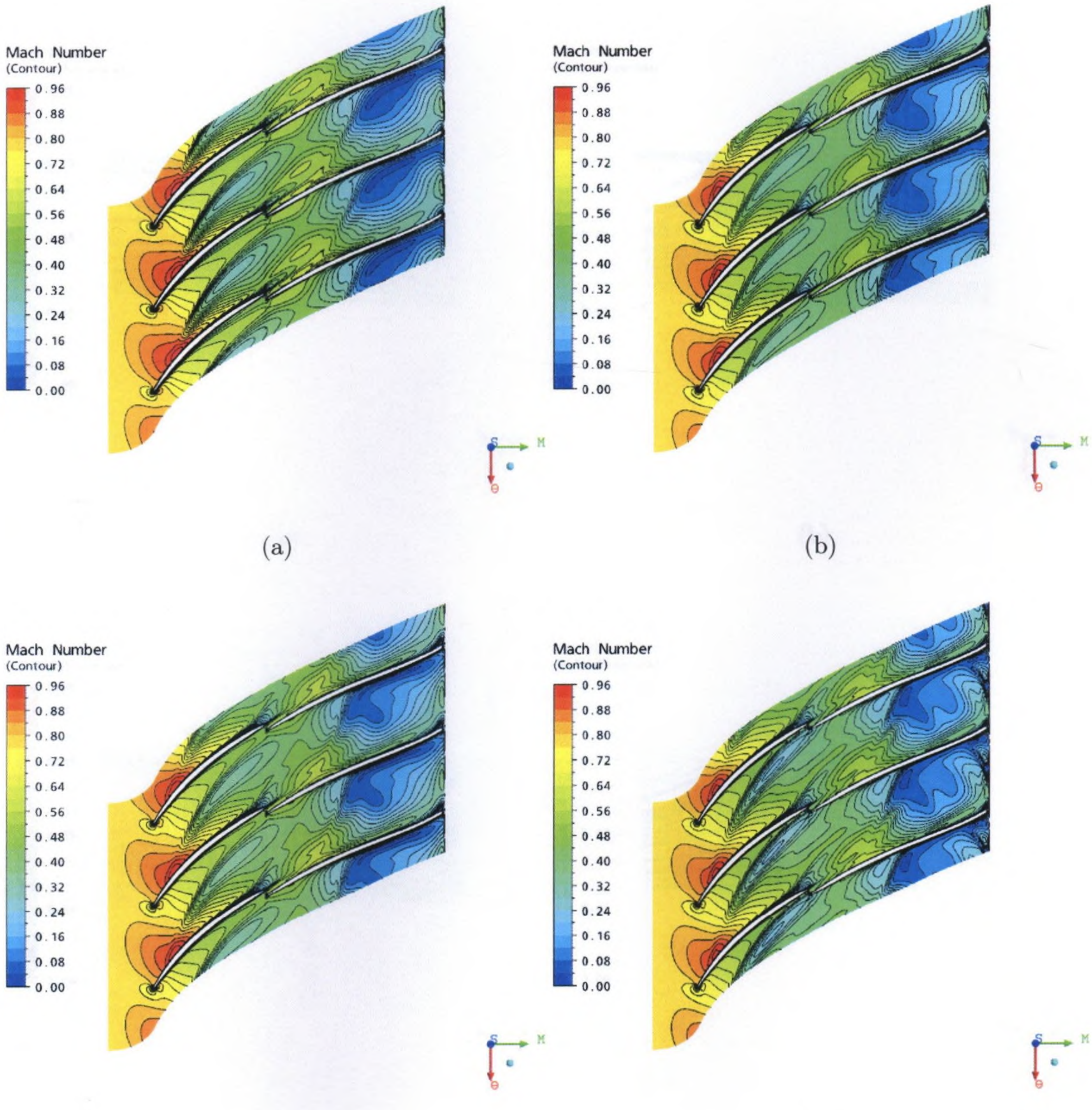

(a) (b)

(c) (d)

Figure 8.5: Blade-to-blade relative Mach number contours at 95% span for the (a) $k-\epsilon$, (b) SST, (c) SST-RM, and (d) RSM-SSG models.

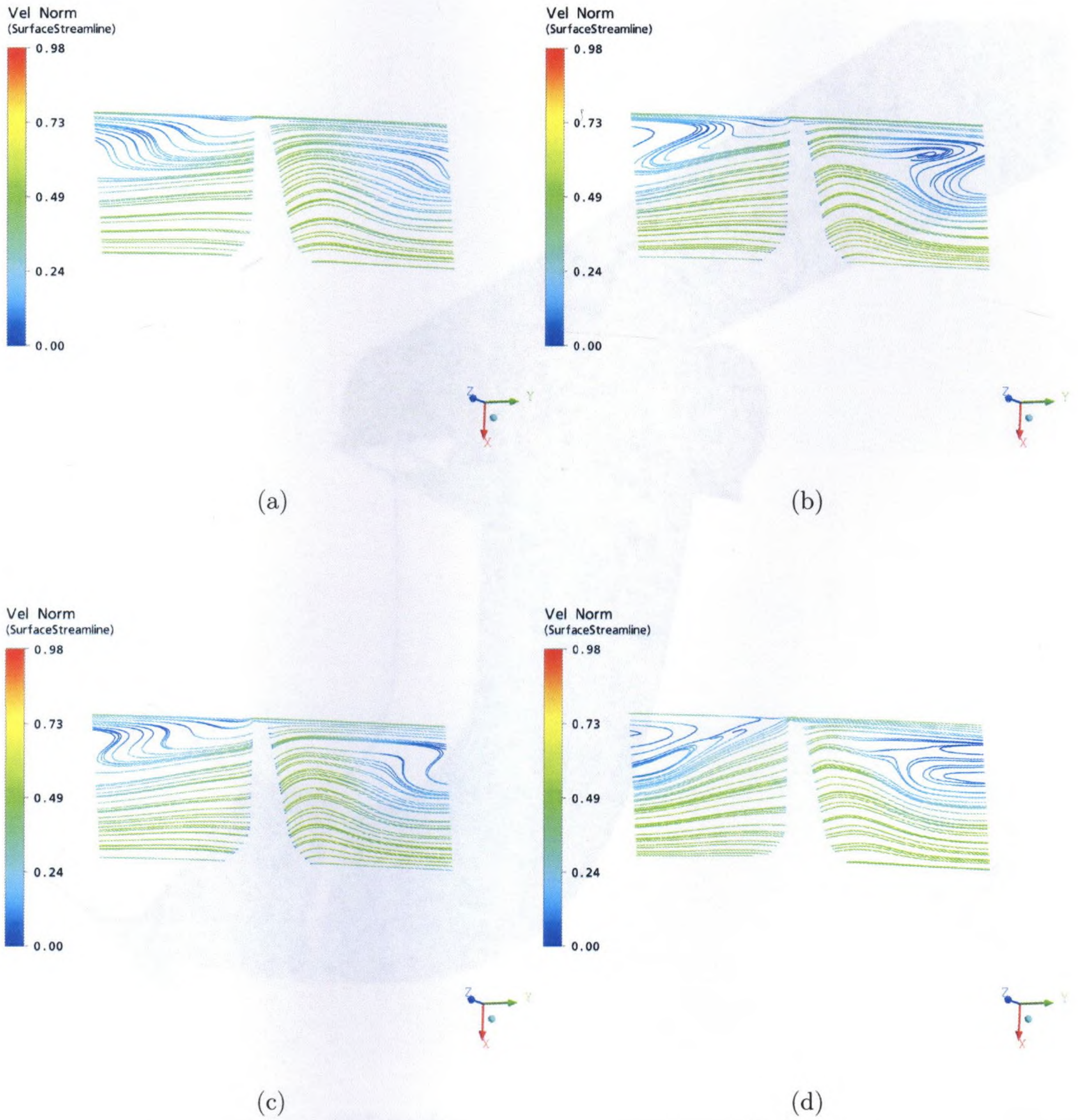

(a) (b) (c) (d)

Figure 8.6: Projected streamlines at $\xi = 1.9$ coloured by the relative velocity normalized by the tip speed, W/U_2, for the (a) $k-\epsilon$, (b) SST, (c) SST-RM, and (d) RSM-SSG models.

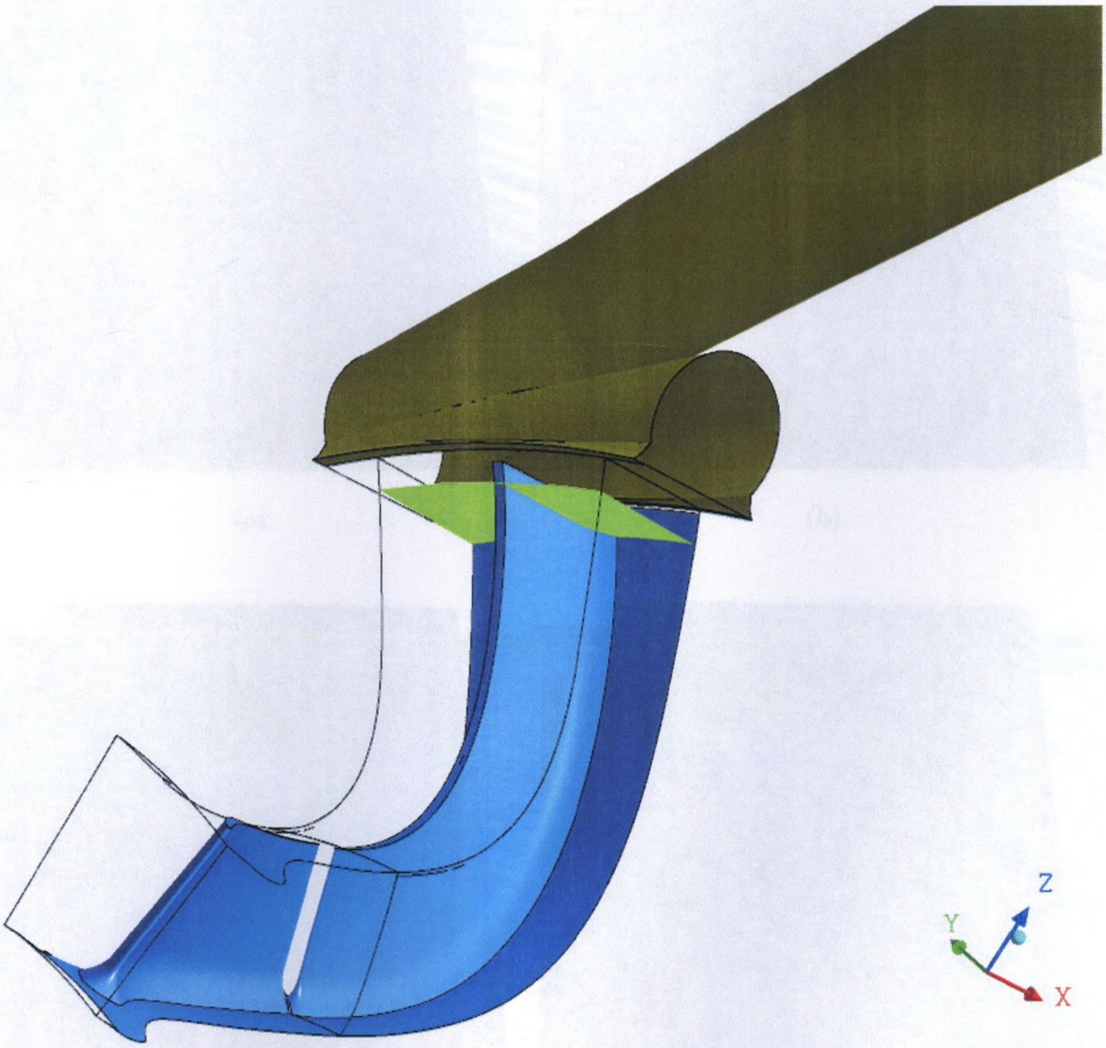

Figure 8.7: Constant $\xi = 1.95$ surface shown in green on which projected streamlines are plotted in Fig. 8.8.

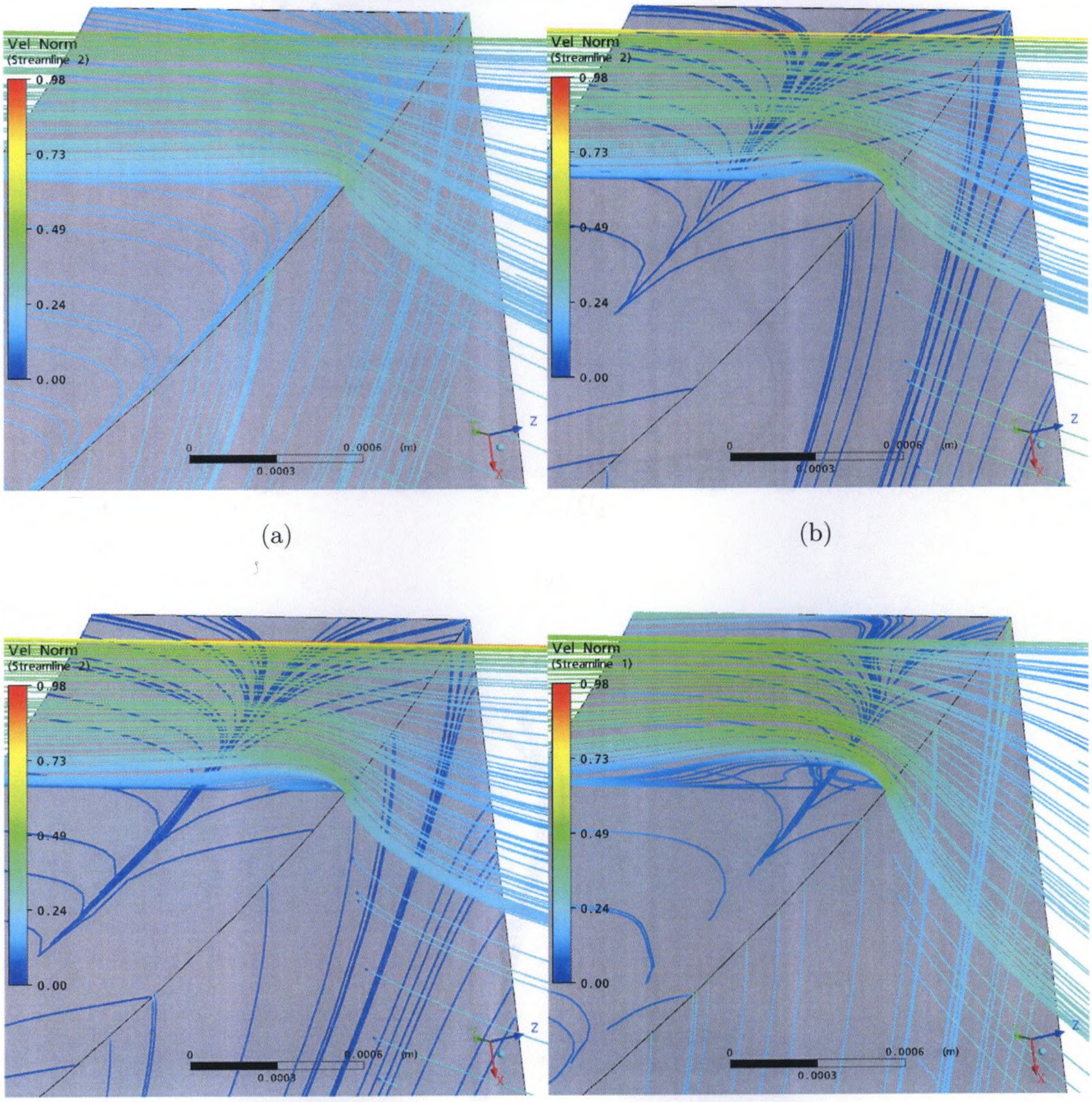

(a) (b)

(c) (d)

Figure 8.8: Tip clearance flow viewed by projected streamlines on a constant $\xi = 1.95$ cut coloured by the relative velocity normalized by the tip speed, W/U_2, for the (a) $k - \epsilon$, (b) SST, (c) SST-RM, and (d) RSM-SSG models.

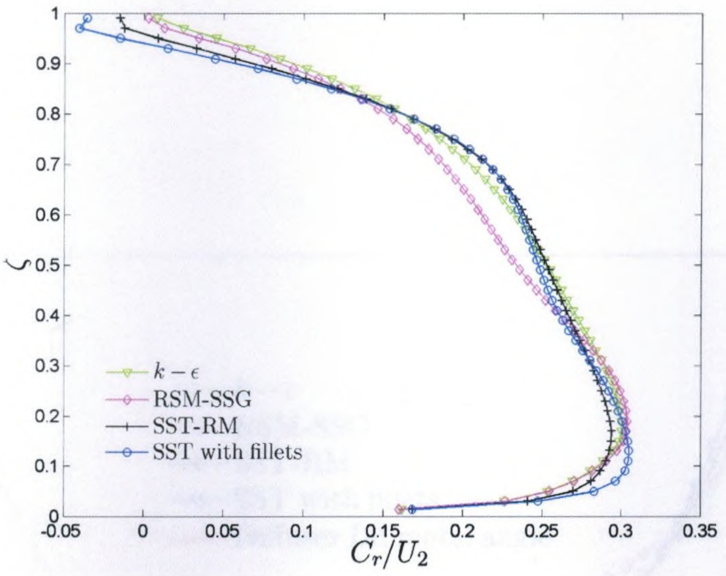

(a)

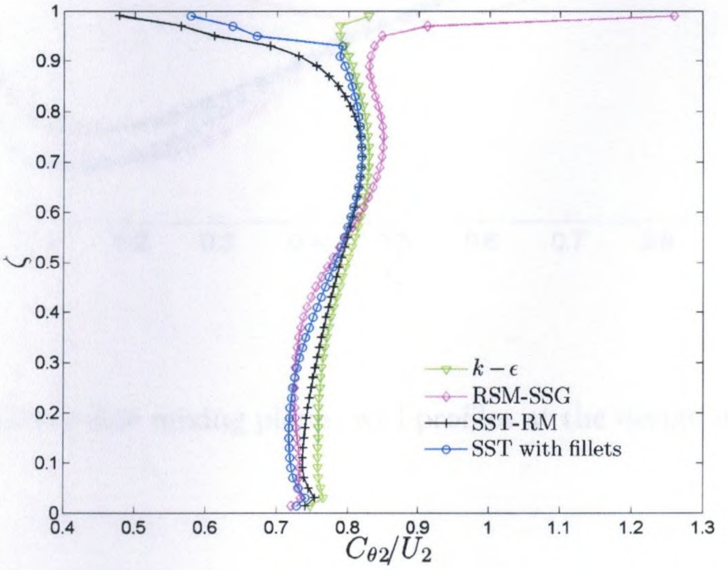

(b)

Figure 8.9: Diffuser side mixing plane velocity profiles at the design net exit corrected flow rate (a) radial (b) tangential.

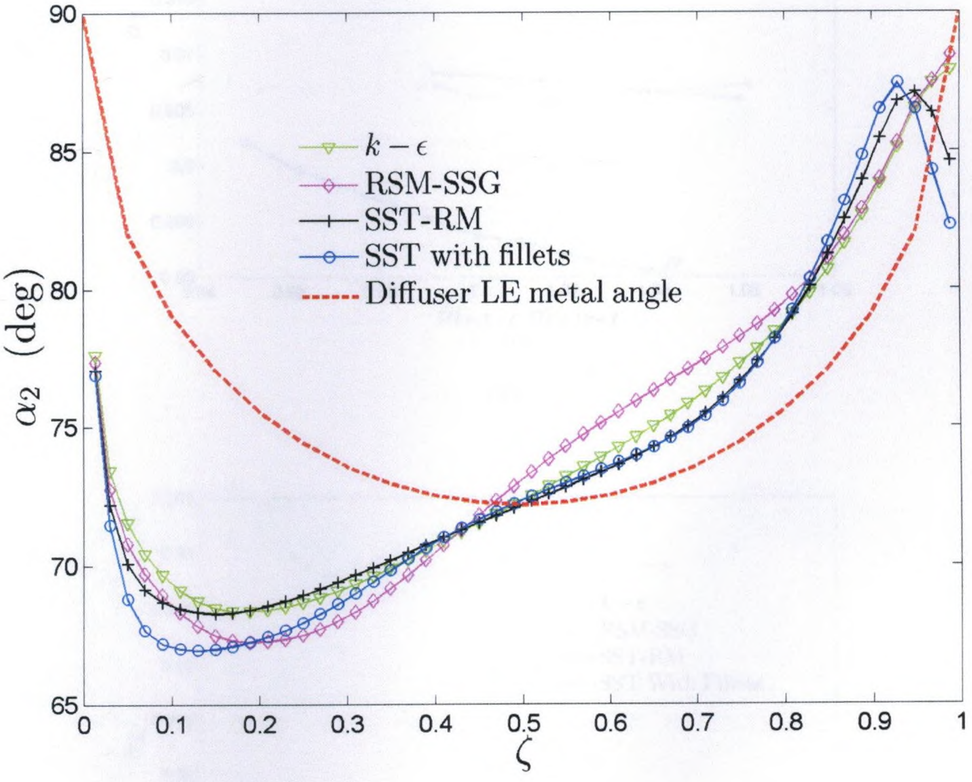

Figure 8.10: Diffuser side mixing plane swirl profiles at the design net exit corrected flow rate.

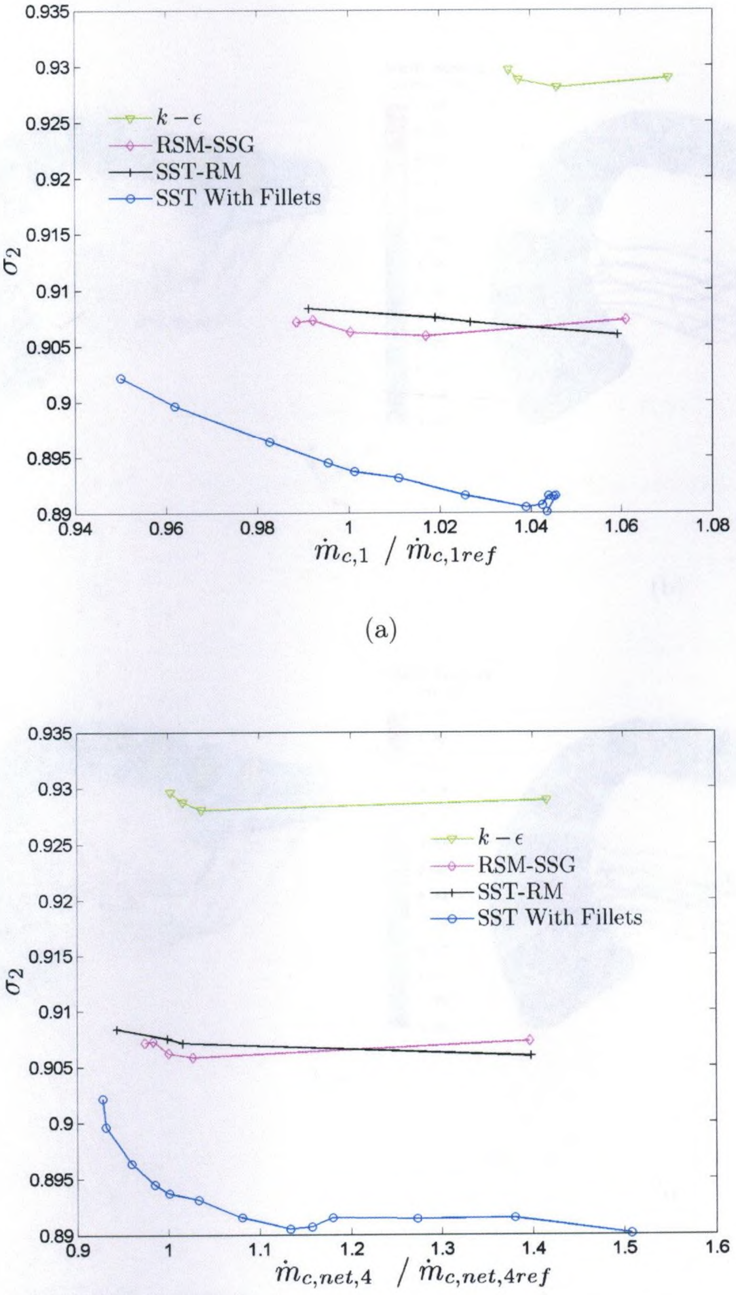

(a)

(b)

Figure 8.11: Aerodynamic slip factor versus (a) inlet corrected flow rate and (b) net exit corrected flow rate.

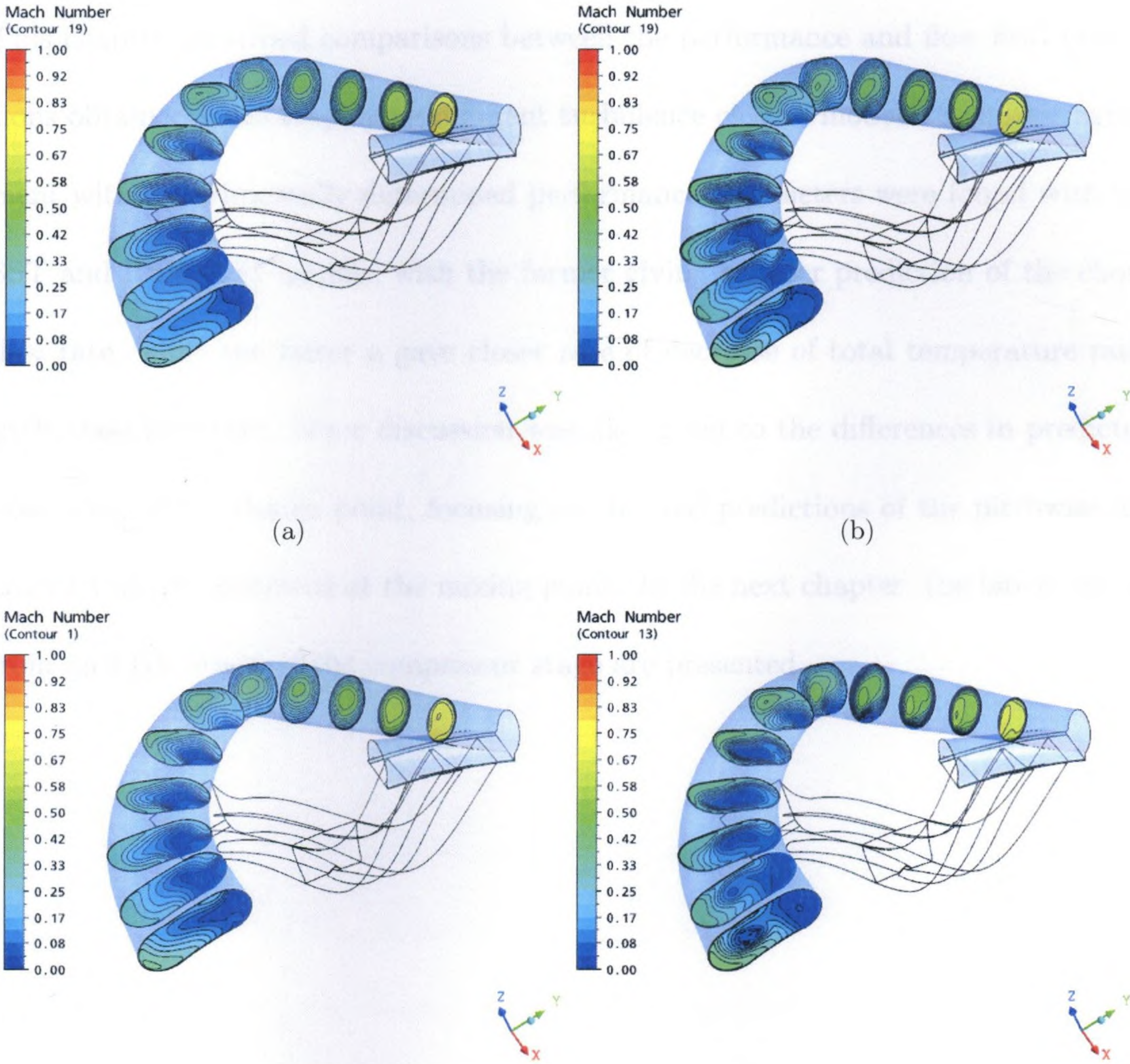

(a) (b)

(c) (d)

Figure 8.12: Diffuser pipe Mach number contours of cuts normal to the centreline for the (a) $k-\epsilon$, (b) SST, (c) SST-RM, and (d) RSM-SSG models.

8.3 Summary

This chapter described comparisons between the performance and flow field predictions obtained when employing different turbulence closure models. The best agreement with experimentally determined performance parameters were found with the SST and RSM-SSG models, with the former giving a closer prediction of the choke flow rate, while the latter a gave closer rate of decrease of total temperature ratio with mass flow rate. Some discussion was also given to the differences in predicted flow fields at the design point, focusing on slip and predictions of the pitchwise averaged velocity and swirl at the mixing plane. In the next chapter, the latest results from an LDV study of the compressor stage are presented.

Chapter 9

Comparison of numerical and experimental results

In the later stages of the numerical studies presented herein, experimental investigations were undertaken which can be used to assess the models employed in the numerical analysis and can deepen the understanding of the compressor flow. Testing was carried out in a compressor test rig at Pratt & Whitney Canada in Longueuil, Quebec. The author was involved in troubleshooting and data collection for approximately a month of the test campaign. Results from this testing stage as well as subsequent measurements have come thanks to the diligent work of Dr. Rofiqul Islam of the University of Calgary and the testing team at P&WC in Longueuil. Two-component laser Doppler velocimetry (LDV) is used to measure velocities within the full-scale centrifugal compressor stage. An overview of the test rig, the LDV optical probe, the three-axis linear traverse, and seeding apparatus is shown in Fig. 9.1.

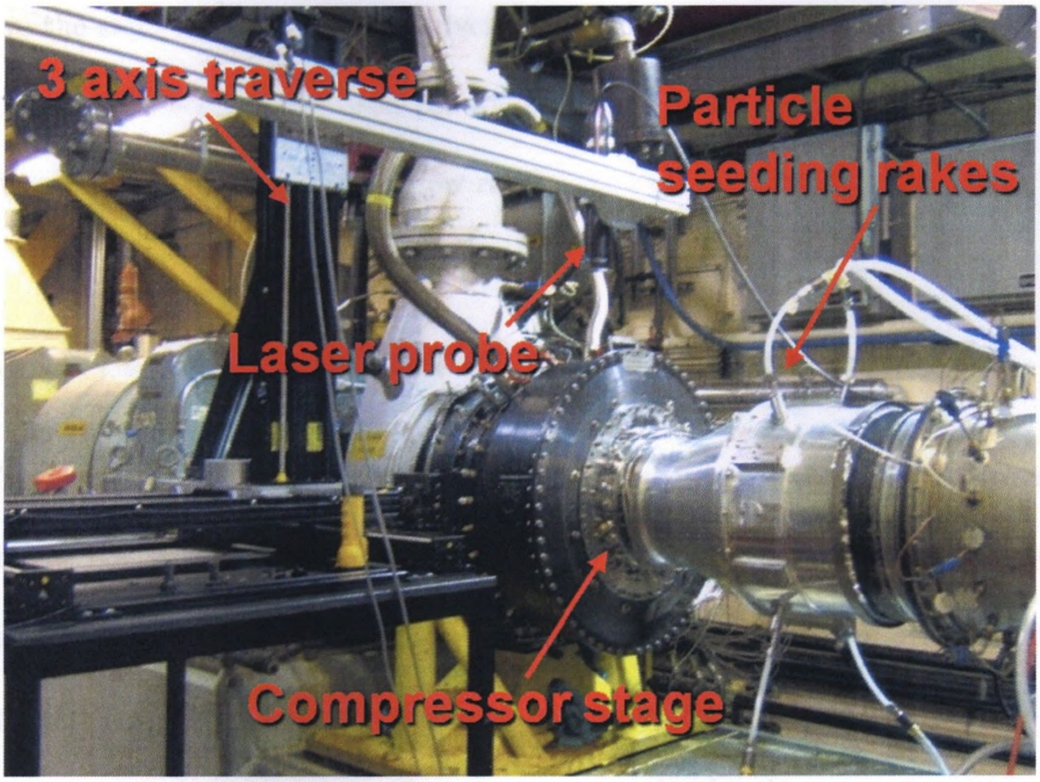

Figure 9.1: Centrifugal compressor test rig.

The rig is driven electrically and a downstream exhaust valve was used to adjust the flow rate through the compressor stage so that at a given shaft speed, the compressor could be run for conditions between choke and stall. The swirl and total pressure profiles that would be encountered at the impeller inlet when running in a full gas turbine engine downstream of a multi-row axial compressor are simulated by using a set of bluff "fingers" which give higher total pressure values on the shroud side of the annulus which are followed by a set of pre-swirl vanes which are designed to give the same swirl as would be given by an upstream multi-stage axial compressor. The LDV studies have been conducted at the design point (100% shaft speed and the design net exit corrected flow rate).

9.1 Brief description of the principle of LDV

LDV is a non-intrusive optical technique used to capture point velocity measurements. It was the technique employed for this study to take measurements at the stage inlet and exit as well as the interface between the rotor and stator in the compressor rig. Other flow measurement techniques that tend to be intrusive have been employed in compressors. Hot-wire anemometry has been employed by Dean and Senoo (1960) at the impeller exit of a vaneless diffuser compressor stage, but the technique was not only intrusive, it was also found that the hot-wire was easily damaged by the high-speed flow. The small passage dimensions in a centrifugal compressor mean that probe dimensions for intrusive measurement techniques must be kept very small to have the least effect on the flow field. Ziegler *et al.* (2003a,b) discuss the special effort to keep the size as small as possible of the instrumentation which included thermocouples, pitot tubes, and cobra probes. In certain cases, compromises needed to be made between keeping the probes as small as possible while keeping the strength of the probes high enough for mechanical safety. They also mention that the compressor would become unstable when using cobra probes to measure velocities in the vaneless space region when the rig was run at design speed, so the speed had to be reduced to 80% to avoid instability.

A significant number of non-intrusive laser based measurements of centrifugal compressors have been undertaken using laser-2-focus (L2F) velocimetry where velocities are based on a time-of-flight of seeding particles passing two laser beams. Examples of studies using L2F include those of Eckardt (1976), Krain (1981), and Ziegler *et al.* (2003a,b). Within the last decade, LDV and particle image velocimetry (PIV) have gained much popularity. Ubaldi *et al.* (1998) and Gizzi *et al.* (1999) used LDV in centrifugal stages with a vaneless diffuser in the former study and a vaned diffuser in the latter. Gizzi *et al.* (1999) noted difficulties in obtaining optical access, seeding of the flow, and reflections off of the walls. Similar problems were encountered with the measurements conducted herein, and some locations required the walls to be painted black to reduce reflections. Wernet (2000) discusses the development of PIV for use in turbomachinery and highlights the benefits of being able to obtain multiple point planar measurements of comparable accuracy to LDV all at once, which can decrease measurement times. For the present study, both PIV and LDV were compared in terms of the difficulty of application and because PIV requires much more optical access, LDV was chosen because only limited optical access was available between the tightly-space compressor components without very significant modifications to the existing rig.

In the present study, the LDV system used is a two-component, dual-beam system operating in back-scatter mode. A dual-beam system operates by splitting a laser beam into a beam pair for each velocity component and passing the split beam pair through a system of optics to a focusing lens. The focusing lens steers the beams such that the beam waists cross at the focal point, creating a small volume called the measurement volume. If the flow is seeded with particles that pass through the measurement volume and reflect light back through the receiving optics, the light seen by a photodector will have a Doppler shift which is directly proportional to the component of velocity of the particle in the direction orthogonal to the bisector of the beams.

9.2 Measurement locations

Measurements were undertaken at three locations along the gas path. They were the impeller inlet, the impeller-diffuser interface, and the diffuser exit. They are denoted as has been done consistently throughout this thesis as locations 1, 2, and 4, respectively (recall from Chapter 2 that location 3 is the diffuser throat where no flow field measurements were undertaken). A cross-sectional view of the compressor rig denoting the locations is shown in Fig. 9.2. The cones enveloping the two pairs of laser beams at each measurement location are depicted with the beam crossing shown at the deepest measurement point at each location. It is this deepest point that determined the height of the optical windows that were manufactured. The width was determined by the size of the traverse plane that was desired at each location, and the thickness was based on the differential pressures between the atmosphere and that inside the rig. At location 2, the beams had to be steered through a 90 degree bend with a mirror because there was not enough clearance to direct the probe directly into the gas path.

Two-component LDV measurements are undertaken in the three locations over a grid of traverse points. The physical locations of the full set of desired grid points are shown in Fig. 9.3. For location 1, not all measurement points have been taken, and those that have are shown to the right of the full set of grid points in Fig. 9.3(a) and are shown according to the fraction of impeller blade pitch, λ_p. For location 2, only a single spanwise traverse at top dead centre of the annulus has been measured. Location 4 measurements have been completed for the full set of grid points. LDV

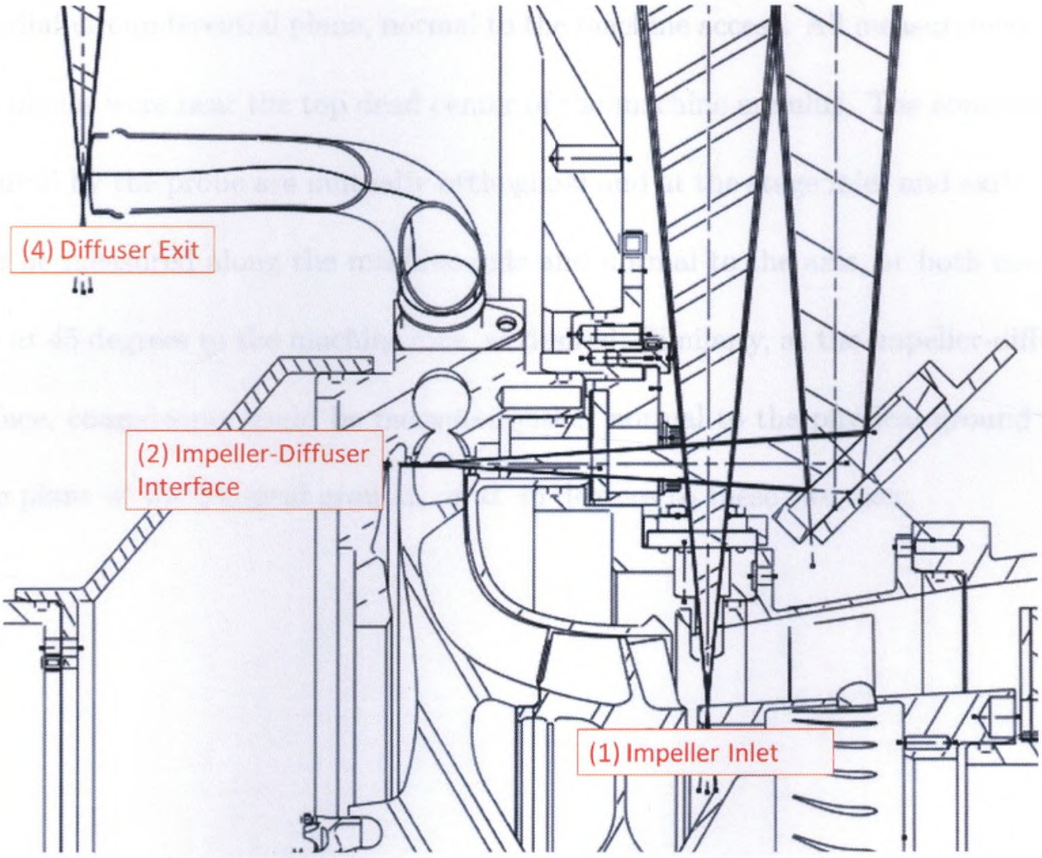

Figure 9.2: Test rig cross-section.

measurements continue at the time of submission of this work, and the full set of data should be available for future analysis when complete.

The measurement plane that contained the two velocity components at the stage inlet and exit was the plane of the physical ground since a Cartesian traverse was used, and velocity components were subsequently transformed into the cylindrical frame of reference. At the impeller-diffuser interface, the plane of measurement was the radial-circumferential plane, normal to the machine access. All measurement traverse planes were near the top dead center of the machine annulus. The components measured by the probe are mutually orthogonal and at the stage inlet and exit could either be measured along the machine axis and normal to the axis, or both components at 45 degrees to the machine axis, as desired. Similarly, at the impeller-diffuser interface, components could be measured either normal to the physical ground and in the plane of the physical ground, or at 45 degrees to these two axes.

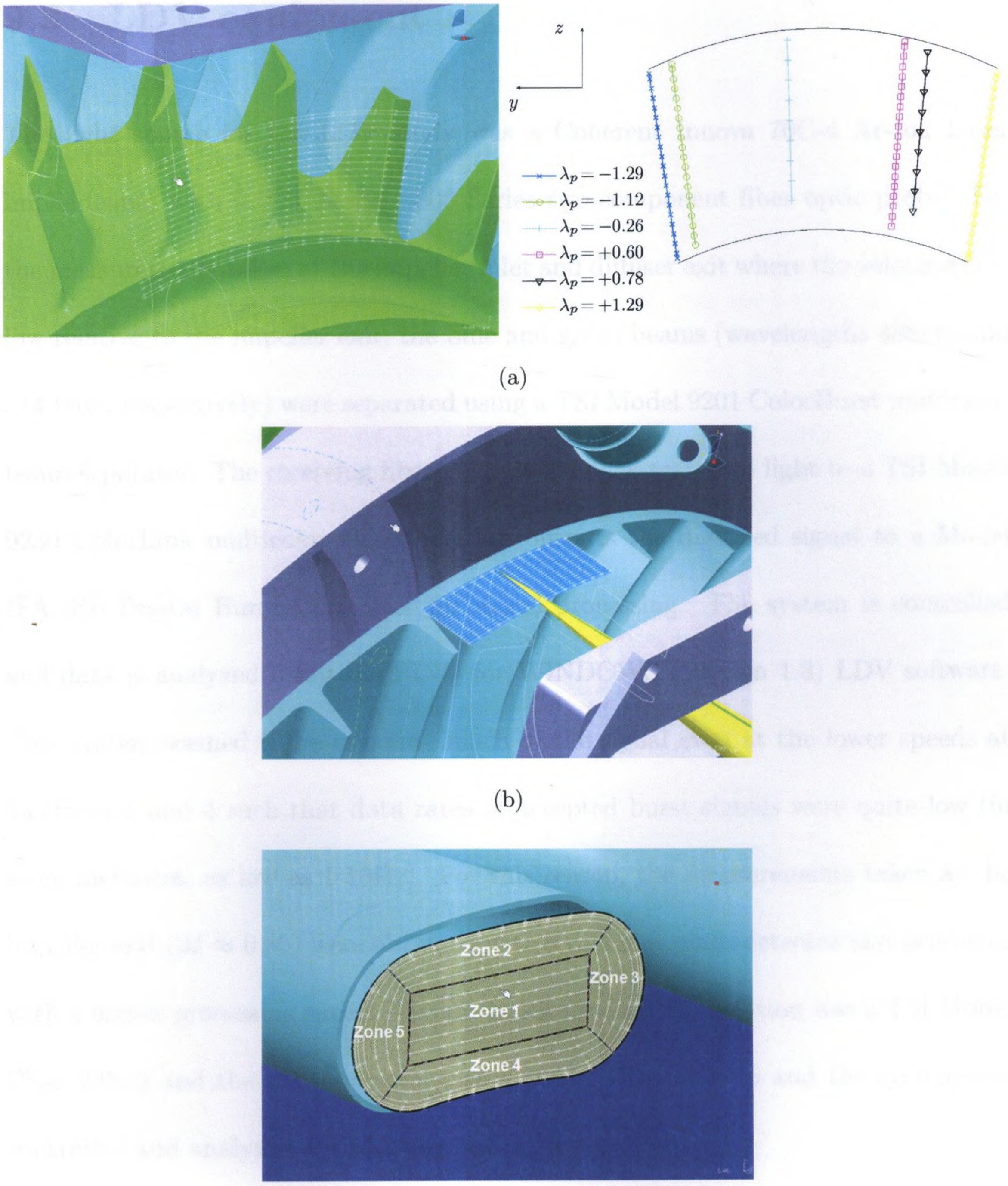

(a)

(b)

(c)

Figure 9.3: Measurement grids at (a) impeller inlet, (b) impeller exit/diffuser inlet, and (c) diffuser exit.

9.3 LDV equipment

The light source for the LDV study was a Coherent Innova 70C-4 Ar-Ion Laser implemented with a TSI Model 9800 Series two-component fiber optic probe. For the measurements taken at the impeller inlet and diffuser exit where the velocities are low relative to the impeller exit, the blue and green beams (wavelengths 488nm and 514.5nm, respectively) were separated using a TSI Model 9201 ColorBurst multicolor beam separator. The receiving fiber couples the back-scattered light to a TSI Model 9230 ColorLink multicolor receiver which outputs the digitized signal to a Model IFA 650 Digital Burst Correlator for signal processing. The system is controlled and data is analyzed using the FIND for WINDOWS (Version 1.3) LDV software. This system seemed to be rejecting much of the signal even at the lower speeds at locations 1 and 4 such that data rates of accepted burst signals were quite low (in some instances, as low as 1-10Hz). For this reason, the measurements taken at the impeller exit ($M \approx 0.85$) were obtained with a different photodetector and processor with a higher processing speed. The processor used at this location was a TSI Model FSA 3500-3 and the photodetector was a Model PDM 1000-5 and the system was controlled and analyzed with its own software.

The optical probe focusing lenses used at the impeller inlet and exit planes was a 350mm Model 9253-350 lens and at the diffuser exit plane, a 250mm Model 9253-

250 lens was used. An LDV system requires optical access to the flow, and for this purpose, the beams are passed through a piece of B270 super white glass at each measurement plane which are sealed with gaskets or o-rings at each location to prevent leakage and allow for the full grid of traverse points to be measured.

Seeding particles used in the study were olive oil, and were injected upstream of the test section from a maximum of 4 seeding rakes at any combination of 6 circumferential locations as shown in Fig. 9.4. The injection rakes had 4 seeding ports at 20% span increments, and could be adjusted in the radial direction and could be turned about their axes to allow better seeding. Speedline curves were obtained with and without the seeding rakes and for conditions with the seeding on and off, and no differences were seen in compressor performance.

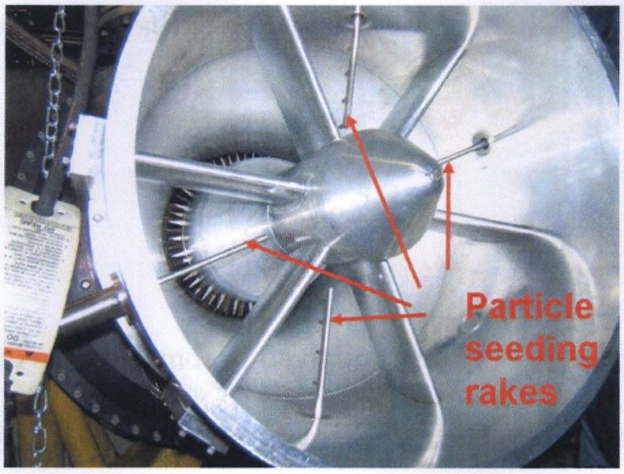

Figure 9.4: Rig intake section with particle seeding rakes.

The fiber optic probe was mounted on a Velmex BiSlide three-axis linear traverse oriented with the machine axis, and the top dead centre radial and circumferential coordinate directions. The traverse is quoted by the manufacturer to have a repeatability of 4 microns, a straight line accuracy of 0.076 mm over the entire travel distance, and a screw lead accuracy of 0.076mm per 25 cm.

9.4 Uncertainty estimate

Uncertainties in calculating mean velocities from LDV measurements are given by two significant sources: the uncertainty in the oscillation of the Bragg cell (uncertainties given by 0.2% of the shift frequency used) and the precision uncertainty, ϵ_P, due to random fluctuations estimated as

$$\epsilon_P = \pm 2 \frac{SD}{\sqrt{N}} \tag{9.1}$$

where SD is the sample standard deviation and N is the number of statistically independent samples. Nearly all measurements had estimated uncertainties of below 1% of the mean, but some measurement points, especially near the walls, yielded uncertainties as high as 5%.

9.5 Impeller inlet

Measurements of the flow field are compared to those at the inlet boundary in the numerical simulations. The flow angles are set as boundary conditions, along with the total pressure and total temperature profiles. They are given as being a function of span only, with no circumferential dependence. In the actual rig, there may be some circumferential dependence according to the location measured compared to the upstream swirl stator vanes.

To correct for temperature differences during the measurement campaign and for proper comparison against CFD, plotted velocity values are corrected to standard temperature, and are denoted with a subscript c as has been done with the corrected flow rates,

$$\vec{C}_c = \vec{C}\sqrt{\frac{T_{ref}}{T_{01}}} \tag{9.2}$$

Points were measured along profiles at a number of different angles, θ, off of top dead centre. They are given in Fig. 9.5 as the fraction of θ on the impeller pitch

$$\lambda_p = \frac{\theta}{2\pi/N_{blades}} \tag{9.3}$$

At both locations 1 and 4, the circumferential velocity component was found from the ground plane measurement velocity and assuming that the component of velocity that is not measured normal to the ground plane is not significant due either to the component being small and to the fact that measurements are never significantly far from top dead centre so as to have much effect on the circumferential velocity component. Fig. 9.6 shows the circumferentially averaged velocity profiles.

The agreement between the simulation profiles and those obtained by LDV is quite good, especially in the mid-span axial velocity component. The spread of velocity measurements with circumferential location is about 5% of the tip velocity and the measured pitchwise averaged profile shows a lower axial velocity on the shroud side than has been found from the numerical simulations with a maximum deviation of 7.5%. On the hub side, the pitchwise averaged axial velocity profile shows a higher velocity compared to that from the numerical simulations with a maximum deviation of 10%. The measured circumferential profile was seen to be flatter than that from the numerical simulations. Fig. 9.7 shows a comparison of the swirl profiles which are a boundary condition on the numerical simulations. It is seen that there is more than a four degree difference in swirl angle at the hub side, and approximately a two degree difference in the mid-span to shroud side angle. It would be interesting for future study to carry out simulations with the swirl angle profiles obtained from LDV to see the effects of this magnitude difference in angle on flow predictions. Because the LDV measurements have been obtained very late in the course of the present work, there was not sufficient time to carry out such an investigation.

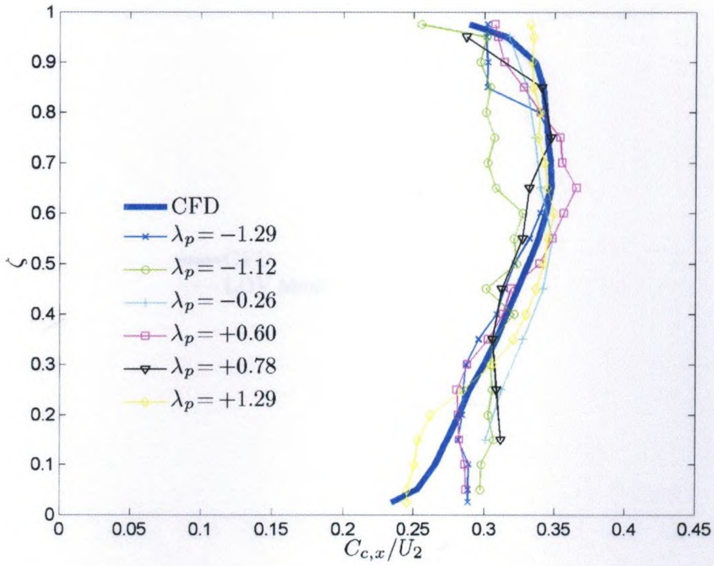

(a)

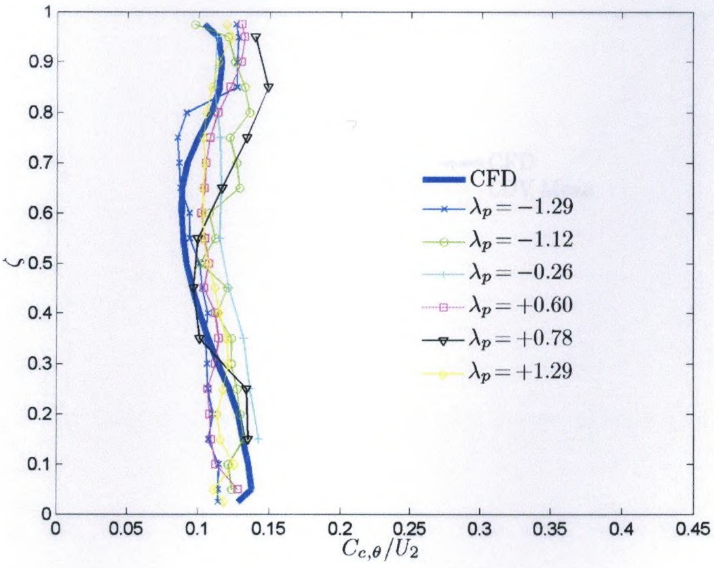

(b)

Figure 9.5: Impeller inlet corrected velocities obtained from LDV (a) axial and (b) circumferential components.

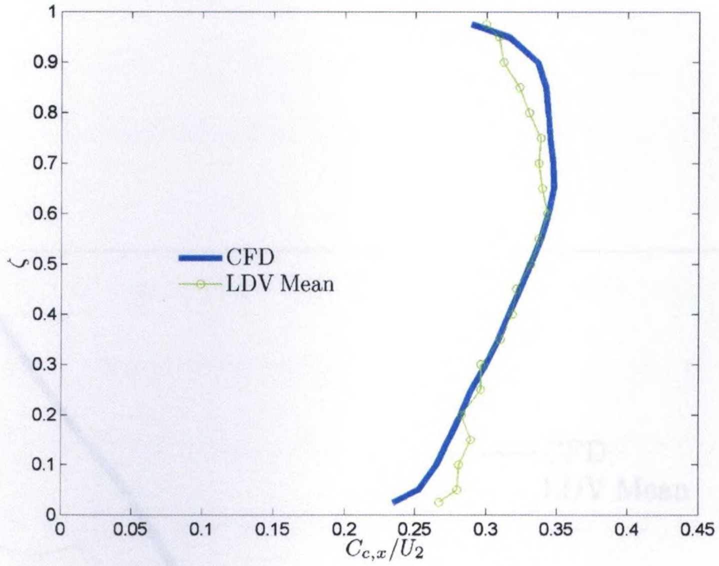

(a)

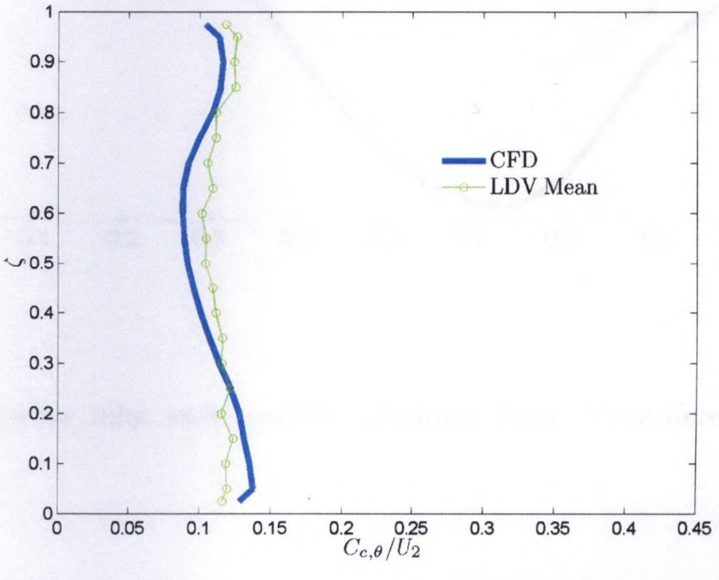

(b)

Figure 9.6: Impeller inlet corrected velocities obtained from circumferential averaging of LDV (a) axial and (b) circumferential components.

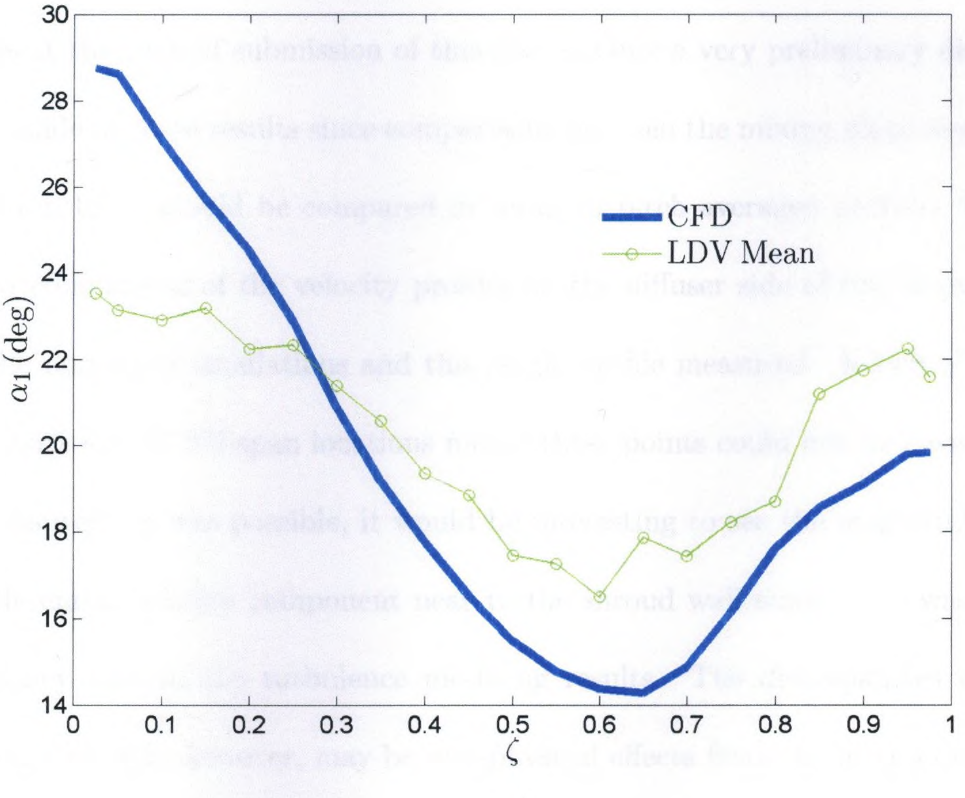

Figure 9.7: Impeller inlet swirl profiles obtained from circumferentially averaged LDV profiles.

9.6 Impeller-diffuser interface

Measurements in the vaneless space in between the impeller trailing edge and the diffuser leading edge have only been made for a traverse of top dead centre of the rig annulus at the time of submission of this thesis. Only a very preliminary discussion can be made of these results since comparisons between the mixing plane results and those from LDV should be compared in terms of pitch averaged profiles. Fig. 9.8 shows a comparison of the velocity profiles on the diffuser side of the mixing plane from the numerical simulations and this single profile measured. A lack of seeding at the 2.5% and 97.5% span locations meant these points could not be measured. If this measurement was possible, it would be interesting to see the magnitude of the circumferential velocity component near to the shroud wall since there was a large discrepancy seen in the turbulence modeling results. The discrepancies with the turbulence models, however, may be non-physical effects from the interaction of the numerical mixing plane and the tip clearance flow. It is seen that there is a significant difference in the radial velocity component by almost 50% in the region from mid-span to the hub. It would seem, then, that since the rig was running at the same corrected mass flow rate as in the simulations, there must likely be large pitchwise differences in the velocity field at this plane, or the difference in magnitude of the two measured velocity components have yielded a high error upon transformation to cylindrical coordinates. At this stage, this is only speculatory, and such issues will have to be investigated once further data is available. Fig. 9.9 shows the swirl angle at the exit of the impeller with a plot of the effective leading edge angle of the elliptical diffuser pipe leading edge to show the flow incidence. Angles would show more similarity to those from the numerical studies if it were not for the differences in the radial velocity. Towards the hub, the maximum difference in predicted and measured swirl angle is up to almost 9 degrees.

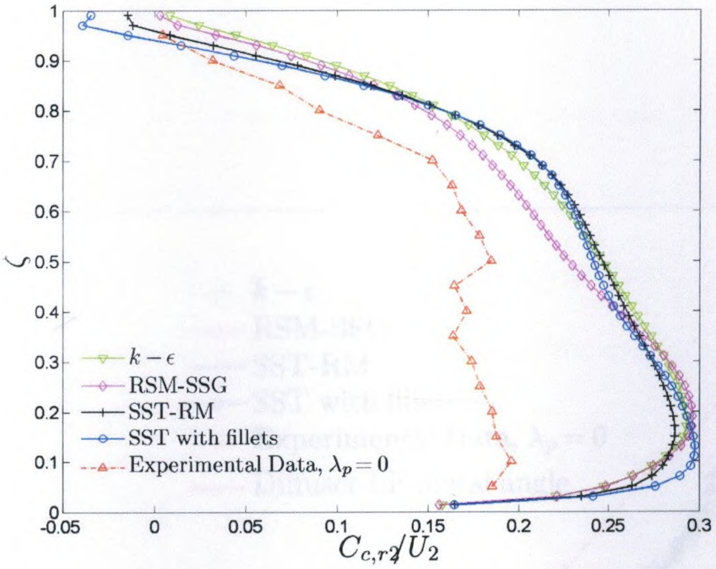

(a)

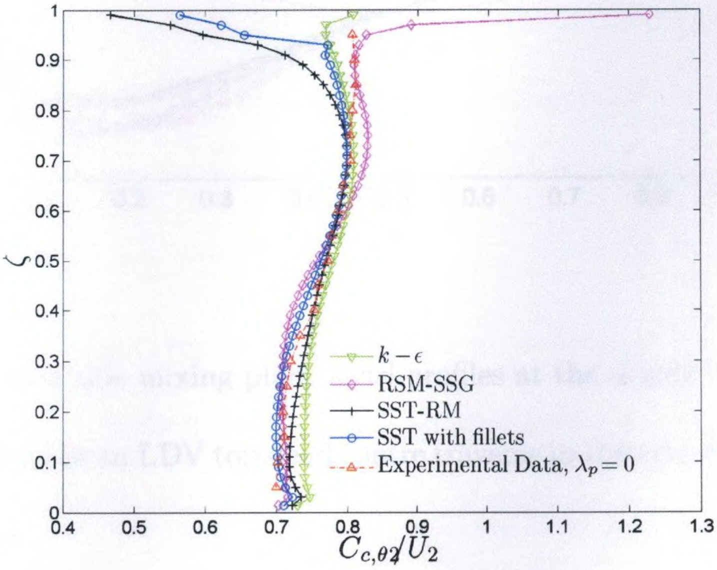

(b)

Figure 9.8: Diffuser side velocity profiles at the design net exit corrected flow rate compared to an LDV top dead centre traverse in the test rig at the impeller-diffuser interface (a) radial and (b) circumferential components.

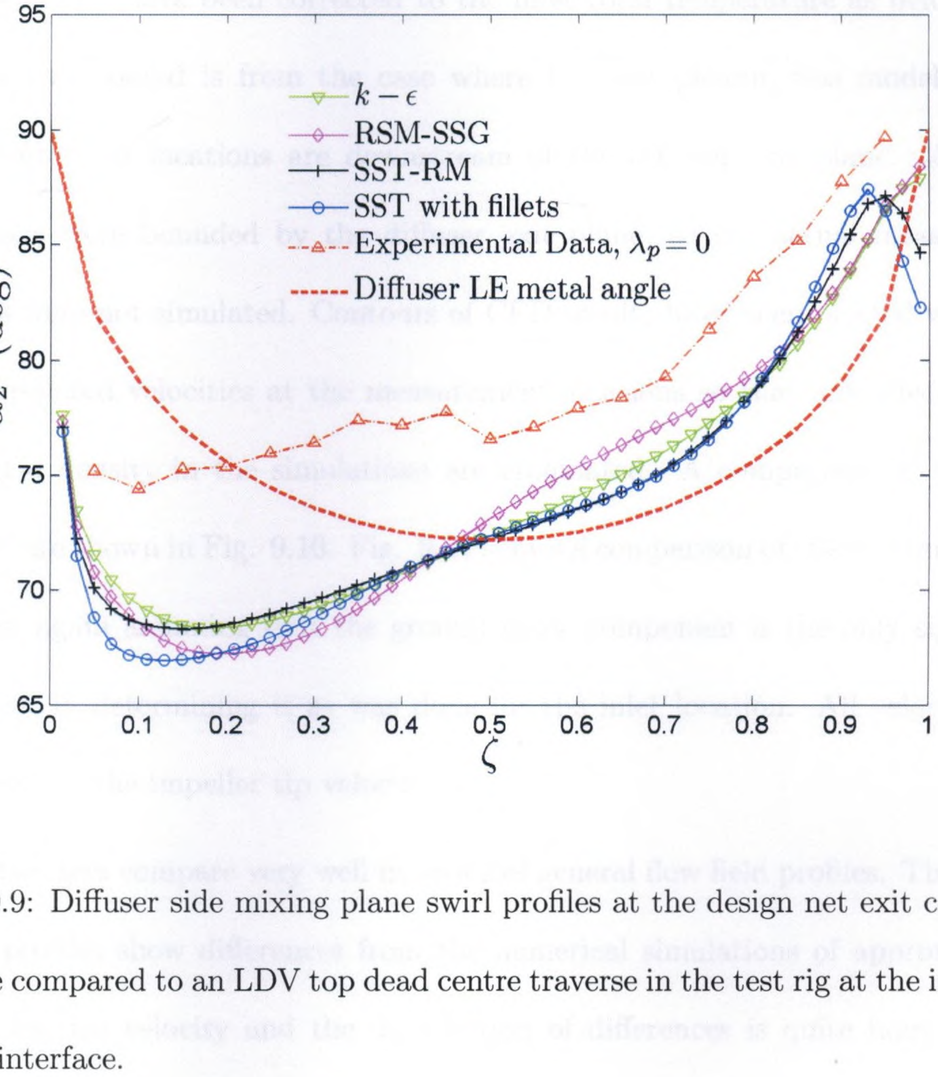

Figure 9.9: Diffuser side mixing plane swirl profiles at the design net exit corrected flow rate compared to an LDV top dead centre traverse in the test rig at the impeller-diffuser interface.

9.7 Diffuser exit

Results for the diffuser exit plane are plotted as has been done for the compressor inlet. Velocities have been corrected to the inlet total temperature as before. The CFD data compared is from the case where the exit plenum was modeled since the measurement locations are downstream of the diffuser exit plane. All other simulations were bounded by the diffuser exit plane, so the actual measurement locations were not simulated. Contours of CFD results have been plotted with only the interpolated velocities at the measurement locations so that any effects of the higher grid density in the simulations are eliminated. A comparison of the axial velocities are shown in Fig. 9.10. Fig. 9.11 shows a comparison of the circumferential velocities, again assuming that the ground plane component is the only significant component in determining it as was done for the inlet location. All velocities are normalized by the impeller tip velocity.

The two sets compare very well in terms of general flow field profiles. The experimental profiles show differences from the numerical simulations of approximately 1-2% of the tip velocity and the distribution of differences is quite homogeneous across the plane without any single section showing much greater differences. The magnitudes of the differences are approximately 6% of the mean which is somewhat higher than the uncertainties estimated in terms of the elemental precision and shift frequency uncertainties. One unquantified, yet likely significant source of uncertainty comes when measuring the high speed flow with the LDV system used. There was a very drastic drop in accepted particle measurements (data rate) when the rig speed was increased up to the design condition, such that only 1-10Hz data rates were typical despite a good particle concentration seen by eye at the measurement location. Despite data scatter from point-to-point over the plane, both quantitative and qualitative agreement between numerical and measured data is found.

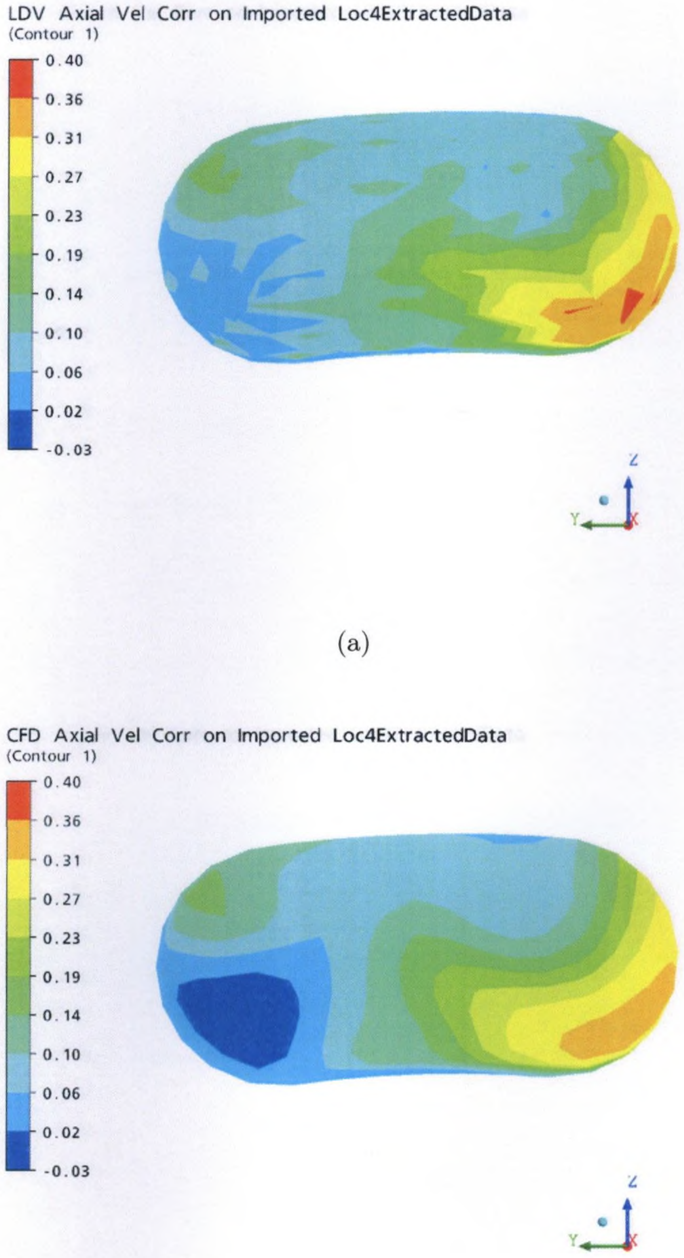

(a)

(b)

Figure 9.10: Diffuser exit corrected axial velocities, $C_{c,x}/U_2$, obtained from (a) LDV and (b) CFD.

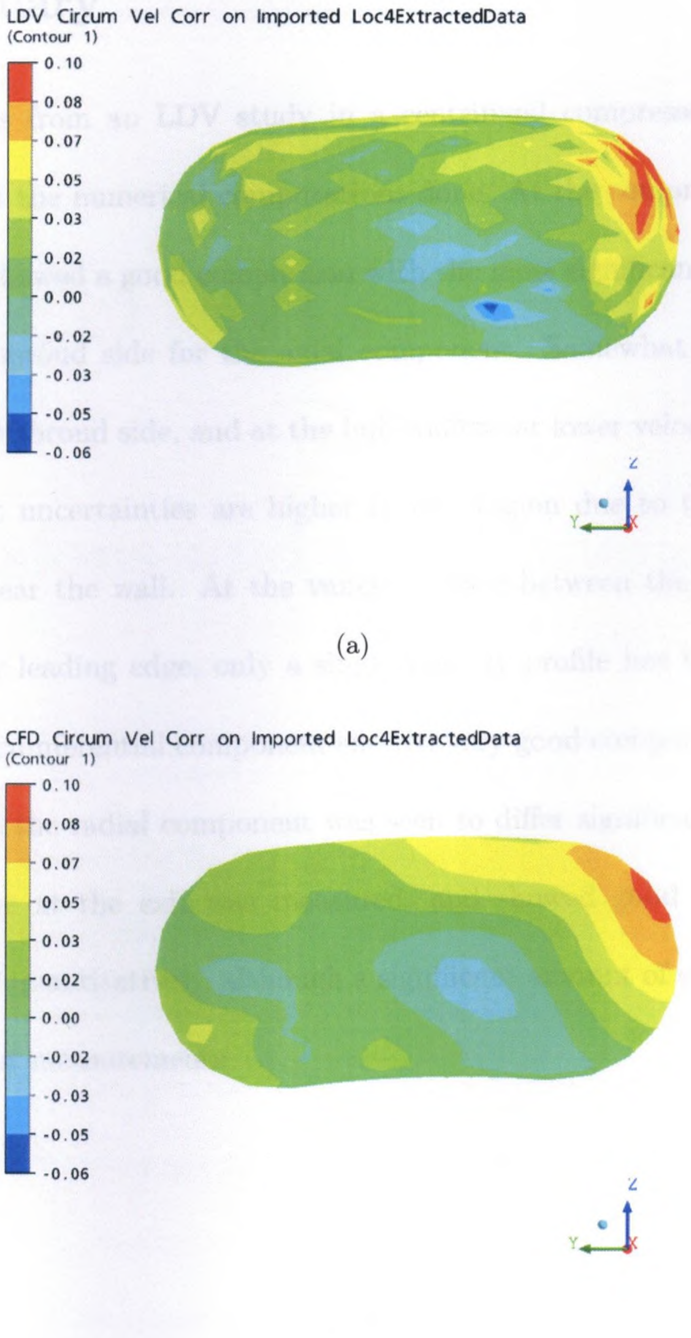

(a)

(b)

Figure 9.11: Diffuser exit corrected circumferential velocities, $C_{c,\theta}/U_2$, obtained from (a) LDV and (b) CFD.

9.8 Summary

The latest results from an LDV study in a centrifugal compressor rig have been compared against the numerical computations done. At the compressor stage inlet, velocity profiles showed a good comparison with the most significant differences seen at the hub and shroud side for the axial component. Somewhat higher velocities were found at the shroud side, and at the hub somewhat lower velocities were found. It is typical that uncertainties are higher in this region due to the higher degree of fluctuations near the wall. At the vaneless space between the impeller trailing edge and diffuser leading edge, only a single velocity profile has been measured to date, and the circumferential component showed very good comparison to numerical predictions while the radial component was seen to differ significantly. A full plane of a diffuser pipe at the exit was measured, and showed good comparison both qualitatively and quantitatively, although a significant amount of scatter was seen in the point to point measurements.

Chapter 10

Conclusions and recommendations

Herein, a number of numerical and experimental studies have been documented for an aero-engine centrifugal compressor stage consisting of a tandem-bladed impeller and fish-tail pipe diffuser. Numerical work presented used the mixing plane technique to obtain steady-state solutions of the governing equations for the coupled rotor-stator flow field by use of a mixing model which applies circumferential averaging of fluxes on the flow leaving the rotating domain to be applied on the downstream stationary diffuser. The mixing plane technique has not been used for long during the design process, and further investigations into experimental validation and an assessment of alternatives to the numerical modeling were deemed highly desirable. Numerical investigations presented herein focus on previously uninvestigated geometrical configurations and the differences in solution by using different turbulence modeling approaches. Experimental data is used for the validation and assessment of the numerical results and include performance and LDV measurements. All studies were for 100% shaft speed, and data presented focused particularly on the design point (defined by the peak efficiency net exit corrected flow rate) as this is the only point investigated using LDV.

In terms of grid geometry, an assessment of using more accurate fillet representation showed how the pressure rise as a function of mass flow rate can shift the performance profiles with respect to simple extension of the upper blade surfaces to the hub as is typically used. The effect of changing the boundary condition from the diffuser exit to the exit of a downstream plenum was also undertaken, and it was seen that performance predictions were unaffected and the pressure profile at the diffuser exit was nearly constant, justifying the use of this type of boundary condition for simulations without a downstream plenum.

In terms of turbulence modeling, the best agreement of numerical and experimental results in terms of measured performance parameters along the speedline was obtained by the SST and RSM-SSG turbulence models. Outside of choke, the RSM-SSG model seemed to follow most accurately the trends of the experimental speedline, yet the SST model seemed to more accurately predict the choke inlet corrected mass flow rate. The SST model showed satisfactory results over the whole speedline. The $k-\epsilon$ model, however, showed an over-prediction of the temperature and pressure ratios, yet a satisfactory prediction of stage efficiency. As the work herein is not only of academic interest, it should also be noted that from a design perspective, there is the issue of time required to carry out simulations that should be mentioned. Although no rigorous attempt has been made here to optimize and quantify the solution times for each model, it was found that with respect to the $k-\epsilon$ model, the time per iteration for the SST model is on the order of about 5% higher, and the RSM-SSG model is approximate 40% higher. Robustness and stiffness issues also led to the need to reduce the iteration time step on the order of 2 to 4 times for the RSM-SSG model, also increasing the time for convergence of this model.

Results from the recent laser Doppler velocimetry (LDV) investigation that is still underway at the submission of this work were presented and compared to numerical simulations. Modifications to a compressor rig fitted with the stage studied herein have been made so that LDV measurements can be carried out to capture the velocity profiles at the impeller inlet, the diffuser exit, and the impeller-diffuser interface. Important physical processes, such as the shroud wall separation seen with only the SST model, could be verified or disproven, thereby showing which direction should be taken for subsequent turbulence modeling of these flows, however with the limited data available at the vaneless space regions, no conclusions about shroud separation can be made. The LDV measurements at the inlet showed a good comparison in the core of the annulus with some differences at the hub and shroud to those at the inlet boundary of the simulations. The swirl angle was determined and was found to have differences between two to 4 degrees at the inlet. Results obtained at the exit of one of the diffuser pipes showed good quantitative and qualitative agreement with those found from the numerical simulations.

10.1 Recommendations for future work

After the LDV measurement campaign is finished, an interesting study would be to run simulations with the best assessment of the pitch-averaged swirl angle profiles obtained from LDV to see the effects of this magnitude difference on flow predictions. Of particular importance, is the pitchwise averaged profiles at the vaneless space in between the impeller trailing edge and diffuser leading edge. The desired data to be captured would include both time averaged unsynchronized and shaft synchronized data sets. The unsychronized data would show the circumferential variations seen in the actual diffuser and an assessment could be made of the validity of the mixing plane, and pitch-averaged profiles could be compared against those from the numerical simulations. Shaft synchronized data sets could show the unsteady flow field, revealing part of the unmodeled impeller-diffuser interaction.

If computational ressources were available, a full unsteady speedline from choke to stall could be carried out to analyze especially each end of the speedline where the flow may have features that cannot be captured with the mixing plane approach, i.e. off design conditions in choke and at stall. Moreover, newer methods have arisen that may be able to capture other physics while still keeping computational costs down like nonlinear harmonic methods (NLH), as described in for example Chen *et al.* (2001). Results obtained with this methodology could be used and compared against the experimental and mixing plane numerical results presented herein.

Appendix A

Governing equations of fluid flow

The conservation equations governing a compressible fluid flow problem are made up of the continuity equation, the momentum equations, and the total energy equation. Herein, their derivations are briefly outlined.

A.1 Conservation of mass

For an arbitrary control volume, V, taken in the continuum, the statement of conservation of mass for a fluid particle in a Lagrangian reference frame is given as

$$0 = \frac{D}{Dt}\int_V \rho dV \tag{A.1}$$

Using the Reynolds Transport Theorem, the Langrangian derivative can be converted to Eulerian derivatives as

$$0 = \int_V \left[\frac{\partial \rho}{\partial t} + \frac{\partial}{\partial x_i}(\rho u_i) \right] dV \tag{A.2}$$

Since this statement is valid for an arbitrary volume, the integrand itself must be equal to zero to satisfy the equality, thus the statement of the conservation of mass (the continuity equation) in differential form may be found,

$$0 = \frac{\partial \rho}{\partial t} + \frac{\partial}{\partial x_i}(\rho u_i) \tag{A.3}$$

A.2 Conservation of momentum

The conservation of momentum principle is stated by Newton's Second Law of motion for a fluid particle. The change in momentum of a fluid particle is equal to the sum of forces acting on the particle, where the surface forces are given by the product of the stress tensor with the outward normal of the surface, $F_i = \sigma_{ji} n_j$, and S_i^m is a source of momentum that acts on a volume element.

$$\frac{D}{Dt} \int_V \rho u_i dV = \oint_S \sigma_{ji} n_j dS + \int_V S_i^m dV \tag{A.4}$$

In the momentum equation, the momentum source term, S_i^m, for the i-th component of momentum could be a typical body force such as gravity or an electromagnetic field, but it could also include the momentum sources which arise as in the present case for rotational frames of reference where there are Coriolis and centrifugal forces as source terms,

$$S_i^{m,Rot} = S_i^{m,Cor} + S_i^{m,Cfg} = -2\epsilon_{ijk}\rho\omega_j u_k - \epsilon_{ijk}\epsilon_{klm}\rho\omega_j\omega_l r_m \tag{A.5}$$

Using the Reynolds Transport Theorem for the term on the left and Gauss' Divergence Theorem for the first term on the right,

$$\int_V \left[\frac{\partial}{\partial t}(\rho u_i) + \frac{\partial}{\partial x_j}(\rho u_i u_j)\right] dV = \int_V \left[\frac{\partial \sigma_{ji}}{\partial x_j} + S_i^m\right] dV \tag{A.6}$$

Again, the fact that the volume selected is arbitrary may be used, so the integrand itself must satisfy the equality. The stress tensor can be decomposed into pressure and viscous parts, where $\sigma_{ji} = -p\delta_{ji} + t_{ji}$.

$$\frac{\partial}{\partial t}(\rho u_i) + \frac{\partial}{\partial x_j}(\rho u_i u_j) = -\frac{\partial p}{\partial x_i} + \frac{\partial t_{ji}}{\partial x_j} + S_i^m \tag{A.7}$$

where the viscous stress tensor is given by

$$t_{ji} = \delta_{ij}\lambda\frac{\partial u_k}{\partial x_k} + \mu\left(\frac{\partial u_i}{\partial x_j} + \frac{\partial u_j}{\partial x_i}\right) = \delta_{ij}\lambda\frac{\partial u_k}{\partial x_k} + 2\mu s_{ij} \tag{A.8}$$

Invoking Stokes' relation that the bulk viscosity is zero, $\kappa = \lambda + 2/3\mu = 0$, giving

$$t_{ji} = \mu \left(\frac{\partial u_i}{\partial x_j} + \frac{\partial u_j}{\partial x_i} - \frac{2}{3} \delta_{ij} \frac{\partial u_k}{\partial x_k} \right) \tag{A.9}$$

Substituting in Eq. (A.7),

$$\frac{\partial}{\partial t}(\rho u_i) + \frac{\partial}{\partial x_j}(\rho u_i u_j) = -\frac{\partial p}{\partial x_i} + \frac{\partial}{\partial x_j}\left[\mu \left(\frac{\partial u_i}{\partial x_j} + \frac{\partial u_j}{\partial x_i}\right)\right] - \frac{2}{3}\frac{\partial}{\partial x_i}\left(\mu \frac{\partial u_k}{\partial x_k}\right) + S_i^m \tag{A.10}$$

A.3 Conservation of energy

For a compressible flow, an equation for the total energy within the flow is also needed. The net rate of change of energy for a given fluid particle is

$$\frac{D}{Dt} \int_V \rho E dV$$

where $E = e + 1/2 u_i u_i$ with e the internal energy and $1/2 u_i u_i$ the kinetic energy. This is balanced by the rate of heat conduction into the particle, $-\oint_S q_j n_j dS$, and the rate of work done by the surface forces. The force on an elemental surface is given by $\sigma_{ji} n_i dS$ and the rate of work done by the surface forces is the scalar product of the force and the velocity vector, $\oint_S \sigma_{ji} u_j n_i dS$. The statement of the conservation of energy is thus

$$\frac{D}{Dt}\int_V \rho E dV = -\oint_S q_j n_j dS + \oint_S \sigma_{ji} u_j n_i dS$$

Employing Gauss' divergence theorem and the Reynolds transport theorem, gives

$$\int_V \left[\frac{\partial}{\partial t}(\rho E) + \frac{\partial}{\partial x_j}(\rho E u_j)\right] dV = -\int_V \left[\frac{\partial q_j}{\partial x_j} + \frac{\partial}{\partial x_i}(\sigma_{ji} u_j)\right] dV$$

Since this has been derived for an arbitrary volume, the relation is valid at a point, and using the chain rule on the terms on the left and cancelling terms using the continuity equation, we find

$$\rho\frac{DE}{Dt} = -\frac{\partial q_j}{\partial x_j} + \frac{\partial}{\partial x_i}(\sigma_{ji} u_j)$$

Substituting for the total stress tensor the sum of the pressure term and the viscous stress tensor, and inserting Fourrier's law for heat conduction,

$$\rho\frac{DE}{Dt} = \frac{\partial}{\partial x_j}\left(\kappa\frac{\partial T}{\partial x_j}\right) - \frac{\partial}{\partial x_i}(p u_i) + \frac{\partial}{\partial x_i}(t_{ji} u_j) \tag{A.11}$$

Now, the momentum equation can be used to rearrange this equation. Taking the scalar product of the momentum equation, Eq. (A.7), with the velocity vector, u_i, gives

$$\rho u_i\frac{Du_i}{Dt} = \rho\frac{D}{Dt}\left(\frac{u_i u_i}{2}\right) = -u_i\frac{\partial p}{\partial x_i} + u_i\frac{\partial t_{ji}}{\partial x_j}$$

Subtracting this from Eq. (A.11),

$$\rho\frac{DE}{Dt}-\rho\frac{D}{Dt}\left(\frac{u_iu_i}{2}\right)=\rho\frac{De}{Dt}=\frac{\partial}{\partial x_j}\left(\kappa\frac{\partial T}{\partial x_j}\right)-\frac{\partial}{\partial x_i}(pu_i)+u_i\frac{\partial p}{\partial x_i}+\frac{\partial}{\partial x_i}(t_{ji}u_j)-u_i\frac{\partial t_{ji}}{\partial x_j}$$

or

$$\rho\frac{De}{Dt}=\frac{\partial}{\partial x_j}\left(\kappa\frac{\partial T}{\partial x_j}\right)-p\frac{\partial u_i}{\partial x_i}+t_{ji}\frac{\partial u_j}{\partial x_i} \tag{A.12}$$

The energy equation can also be cast in terms of the total enthalpy, $h_o = h + 1/2u_iu_i = e + p/\rho + u_iu_i = E + p/\rho$. With some algebra and application of the continuity equation, one obtains

$$\rho\frac{DE}{Dt}+\frac{\partial}{\partial x_i}(pu_i)=\rho\frac{Dh_o}{Dt}-\frac{\partial p}{\partial t}$$

Substituting this into Eq. (A.11),

$$\rho\frac{Dh_o}{Dt}=\frac{\partial p}{\partial t}+\frac{\partial}{\partial x_j}\left(\kappa\frac{\partial T}{\partial x_j}\right)+\frac{\partial}{\partial x_i}(t_{ji}u_j) \tag{A.13}$$

Or using the continuity equation to put the energy equation in conservative form gives

$$\frac{\partial}{\partial t}(\rho h_o)+\frac{\partial}{\partial x_j}(\rho h_o u_j)=\frac{\partial p}{\partial t}+\frac{\partial}{\partial x_j}\left(\kappa\frac{\partial T}{\partial x_j}\right)+\frac{\partial}{\partial x_i}(t_{ji}u_j) \tag{A.14}$$

References

ANSYS (2006). *ANSYS CFX-Solver Theory Guide. ANSYS CFX Release 11.0.* ANSYS, Inc., Canonsberg, PA.

Barth, T. J. and Jesperson, D. C. (1989). The design and application of upwind schemes on unstructured meshes. *AIAA Paper*, (89-0366).

Boussinesq, J. (1877). Théorie de lécoulement tourbillant. *Mém. Présentés par Divers Savants Acad. Sci. Inst. Fr.*, **23**:46–50.

Bradshaw, P., Ferriss, D. H., and Atwell, N. P. (1967). Calculation of boundary layer development using the turbulent energy equation. *Journal of Fluid Mechanics*, **28**(3):593–616.

Chen, T., Vasanthakumar, P., and He, L. (2001). Analysis of unsteady blade row interaction using nonlinear harmonic approach. *Journal of Propulsion and Power*, **17**(3):651–658.

Cumpsty, N. A. (1989). *Compressor Aerodynamics.* Longman Scientific & Technical, Essex.

Dawes, W. N. (1995). Simulation of unsteady interaction of a centrifugal impeller with its vaned diffuser: flow analysis. *Journal of Turbomachinery*, **117**(2):213–222.

Dean, R. C. and Senoo, Y. (1960). Rotating wakes in vaneless diffusers. *Journal of Basic Engineering Series D*, **82**(3):563–574.

Dixon, S. L. (2005). *Fluid mechanics and thermodynamics of tubomachinery, 5e.* Elsevier-Butterworth-Heinemann, Amsterdam, Boston.

Eckardt, D. (1976). Detailed flow investigations within a high-speed centrifugal compressor impeller. *Journal of Fluids Engineering*, **98**(3):390–402.

Favre, A. (1965a). Equations des gaz turbulent compressibles I. Formes générales. *Journal de Mécanique*, **4**(3):361–390.

Favre, A. (1965b). Equations des gaz turbulent compressibles II. Méthode des vitesses moyennes; méthode des vitesses macroscopiques pondérées par la masse volumique. *Journal de Mécanique*, **4**(4):391–421.

Gizzi, W. P., Roduner, C., Stahlecker, D., and K oppel, G., P. Gyarmathy (1999). Time-resolved measurements with fast-response probes and laser Doppler velocimetry at the impeller exit of a centrifugal compressor: a comparison of two measurement techniques. *Proceedings of the Institution of Mechanical Engineers, Part A: Journal of Power and Energy*, **213**(4):291–308.

Jones, W. P. and Launder, B. (1973). The calculation of low-Reynolds-number-phenomena with a two-equation model of turbulence. *International Journal of Heat and Mass Transfer*, **16**:1119–1130.

Kenny, D. P. (1968). A novel low cost diffuser for high performance centrifugal compressors. *ASME Paper*, (68-GT-38).

Krain, H. (1981). A study on centrifugal impeller and diffuser flow. *Journal of Engineering for Power*, **103**:688–697.

Krain, H. (1988). Swirling Impeller Flow. *Journal of Turbomachinery*, **110**:122–128.

Launder, B. E. and Sharma, B. I. (1974). Application of the energy dissipation model of turbulence to the calculation of flow near a spinning disc. *Letters in Heat and Mass Transfer*, **1**(2):131–138.

Menter, F. R. (1994). Two-equation eddy-viscosity turbulence models for engineering applications. *AIAA Journal*, **32**(8):1598–1605.

Merz, L. F., Dailey, L. D., and Orkwis, P. D. (2004). A CFD Study of the Flow

Through a Transonic Compressor Rotor with Large Tip Clearance. *AIAA Paper*, (2004-3934).

Patel, R. (2007). *Experimental and numerical investigation of a stationary cascade rig*. Master's thesis, University of Western Ontario.

Raw, M. J. (1996). Robustness of coupled algebraic multigrid for the Navier-Stokes equations. *AIAA Paper*, (96-0297).

Reynolds, O. (1895). On the dynamical theory of incompressible viscous fluids and the determination of the criterion. *Philosophical Transactions of the Royal Society of London, Series A*, **186**:123–164.

Rhie, C. M. and Chow, W. L. (1983). A numerical study of the turbulent flow past an airfoil with trailing edge separation. *AIAA Journal*, **21**:1525–1532.

Roberts, D. and Kacker, S. C. (2002). Numerical investigation of tandem-impeller designs for a gas turbine compressor. *Journal of Turbomachinery*, **124**:36–44.

Roberts, D. and Steed, R. (2004). A Comparison of Steady-State Centrifugal Stage CFD Analysis to Experimental Rig Data. *ANSYS Users Conference, Pittsburgh.*

Schlichting, H. and Gersten, K. (2000). *Boundary layer theory: 8th revised and enlarged edition*. Springer Verlag, Berlin Heidelberg.

Shabbir, A., Zhu, J., and Celestina, M. (1996). Assessment of Three Turbulence Models in a Compressor Rotor. *ASME 96-GT-198, International Gas Turbine and Aeroengine Congress & Exhibition, Birmingham.*

Shum, Y. K. P., Tan, C. S., and Cumpsty, N. A. (2000). Impeller-Diffuser Interaction in a Centrifugal Compressor. *Journal of Turbomachinery*, **122**:777–786.

Smirnov, P. E., Hansen, T., and Menter, F. R. (2007). Numerical Simulation of Turbulent Flows in Centrifugal Compressor Stages with Different Radial Gaps. *ASME GT2007-27376, Proceedings of ASME Turbo Expo, Montreal.*

Speziale, C. G., Sarkar, S., and Gatski, T. B. (1991). Modelling the pressure-strain correlation of turbulence: an invariant dynamical systems approach. *Journal of Fluid Mechanics*, **227**:245–272.

Ubaldi, M., Zunino, P., and Ghiglione, A. (1998). Detailed flow measurements within the impeller and the vaneless diffuser of a centrifugal turbomachine. *Experimental Thermal and Fluid Science*, **17**(1):147–155.

Wernet, M. (2000). Development of digital particle imaging velocimetry for use in turbomachinery. *Experiments in Fluids*, **28**(2):97–115.

Wilcox, D. C. (1998). Reassessment of the scale-determining equation for advanced turbulence models. *AIAA Journal*, **26**(11):1299–1310.

Wilcox, D. C. (2006). *Turbulence Modeling for CFD, 3e.* DCW Industries, La Cañada.

Ziegler, K. U., Gallus, H. E., and Niehuis, R. (2003a). A study on impeller-diffuser interaction Part I: Influence on the performance. *Journal of Turbomachinery*, **125**:173–182.

Ziegler, K. U., Gallus, H. E., and Niehuis, R. (2003b). A study on impeller-diffuser interaction Part II: Detailed flow analysis. *Journal of Turbomachinery*, **125**:183–192.